# CMB Observations and the Metal Enrichment History of the Universe
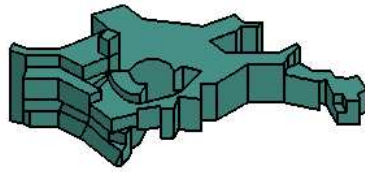
Kaustuv moni Basu

Max-Planck-Institut für Astrophysik

Garching

"We are all in the gutter, but some of us are looking at the stars."

– Oscar Wilde

# Acknowledgements

# Abstract

The main purpose of the work presented in this thesis is to investigate the phenomenon of resonant scattering of the Cosmic Microwave Background (CMB) photons by atoms and molecules. The fine-structure transitions of the various atoms and ions of Carbon, Nitrogen, Oxygen and other common metals have wavelengths in the far-infrared regions, which are particularly suitable for scattering the CMB photons at high redshifts ($2 \lesssim z \lesssim 30$). Since the CMB photons are released at redshifts $z \simeq 1100$, they must interact with all the intervening matter before reaching us at $z = 0$. Therefore scattering of these photons in the far-IR fine-structure lines of various atoms and ions provide a plausible way to couple the radiation with the matter at those redshifts and to study the enrichment and ionization history of the universe. Moreover, rotational transitions of diatomic molecules like the CO have wavelengths extending into the sub-millimeter wavebands, and hence they can scatter the CMB photons at very low redshifts. Studying the very low density gas of nearby galaxies in CO lines can yield a definitive signature of resonant scattering of the CMB photons through a decrement in the background intensity of the microwave sky. Observation of this scattering signal from any object in the sky will tell us about its radial velocity in the CMB rest frame.

In this work we first derive the detailed formalism for the scattering effect in presence of the peculiar motion of the scatterer. Then we investigate the possibility to detect individual objects at different redshifts through scattering and try to find applications for this effect. Our main example is the possibility to find the peculiar motions of nearby galaxies in the CMB rest frame through observation of the scattering signal, which we explore in detail. Next we discuss the density limits in which scattering effect can dominate over the line emission in individual objects. We describe three types of critical densities, and show that detection of single objects through scattering requires very low density, whereas observation of the integrated scattering signal coming from many unresolved objects in the sky will permit us to probe higher densities. We discuss this effect subsequently, as we compute the change in the angular fluctuations of the CMB sky temperature through resonant scattering. We found that the scattering signal gets strong enhancement due to a non-zero correlation existing between the density perturbations at the last scattering surface, where CMB anisotropies are generated,

and at the epoch of scattering. This opens up a new way to study the ionization and enrichment history of the universe, and we investigate various enrichment scenarios and the temperature fluctuations that might be caused by them. The resulting signal is already within the sensitivity limits of some upcoming space- and ground-based CMB experiments, and we show upto what extent they shall be able to put constraints on different enrichment histories. Finally we analyze the effect of line and dust emission in the same frequency range that we used for the detection of scattering signal. These emissions are coming from very high density objects where active star formation is taking place, and due to the compactness of their size as well as absence of any velocity dependence the emission signal is significantly suppressed at large angular scales, where scattering will be dominant. We present some detailed analytic expressions for the scattering signal and also a method to solve for the detailed statistical balance equations in a multi-level system in the appendix.

# Contents

# List of Figures

# List of Tables

# Chapter 1

# Introduction

The analysis of the Cosmic Microwave Background (CMB) provides a crucial test bed for cosmological models and theories of interaction of matter and radiation during the course of evolution of the universe. The CMB photons received today were released at the redshift $z \simeq 1100$, when the universe was only $300,000$ years old, therefore studying the changes in the thermal spectrum as well as angular intensity distribution of the CMB can yield information about many subsequent events in the cosmic history, like growth of structure formation, reionization of the universe by the first stars, or evolution of the chemical abundances leading to present day values. High precision CMB observations are already giving us unique information about the angular distribution of the temperature fluctuations, as well as their spectral dependence in a wide frequency range. After an year of operation, the WMAP satellite has obtained the first peaks of the CMB power spectrum with an accuracy of a few percent (Hinshaw et al. 2003), and is on its way to provide measurements of the temperature anisotropies in the whole sky with an average sensitivity of 35 $\mu$K per $0.3° \times 0.3°$ at the end of the mission (Bennett et al. 2002, Page et al. 2002). HFI and LFI detectors of PLANCK spacecraft will provide unprecedented sensitivity in 9 broad band ($\Delta\nu/\nu \sim 20 - 30\%$) channels, uniformly distributed in the spectral region of the CMB where contribution of different foregrounds are expected to be at a minimum. The ground-based and balloon-borne experiments like Boomerang, APEX, SPT & ACT, will provide complimentary information about the temperature fluctuations at small scales ($\theta \lesssim 1°$), and will also provide very high precision measurements of the changes in the background intensity of the CMB inside particular objects in the sky.

In this work we have tried to find some additional use for the sensitivities of these forthcoming CMB experiments, by means of the process of resonant scattering of the CMB photons in atomic, ionic or molecular lines. In presence of the peculiar velocity of the scatterer, the change in the brightness temperature of the background CMB photons takes a particularly simple form

$$\frac{\Delta \mathrm{T}(\nu)}{\mathrm{T_{CMB}}} \ = \ - \ \tau_\nu \ \left(\frac{v_\parallel}{c}\right) \tag{1.1}$$

where $\Delta T(\nu)$ is the change in brightness temperature observed at the line frequency $\nu$, $T_{\mathrm{CMB}}$ is the mean temperature of background CMB photons, $\tau_\nu$ is the optical depth for scattering at resonance, and $v_\parallel$ is the radial component of peculiar motion of the object in the CMB rest frame. The negative sign arises from the convention of taking velocities positive for motion away from the observer, which results in a decrement of temperature. We found that such decrement is the unique feature of the scattering signal, which might help to distinguish it from the emission in the same line. In fact, the same effect of scattering had been discussed by several authors in the past, but a formal derivation of the effect had been absent. It was first analyzed by Dubrovich (1977, 1993), who followed Sunyaev & Zel'dovich papers (1970, 1980) on influence of electron scattering on CMB angular fluctuations, and coined the term "spatial-spectral fluctuations" to describe the effect of resonant scattering. This effect was analyzed later in detail by Maoli et al. (1994, 1996). These authors were interested in the detection of primordial molecules, like HD, LiH, $H_2D$, $HD^+$ etc., and there were also attempts to observe them experimentally (de Bernardis et al. 1993). We have extended their analysis to the fine-structure transitions of the various atoms and ions of metals like carbon, oxygen, nitrogen etc., which were produced at the end of the dark ages by the first stars. These fine-structure transitions arise from the spin-orbit coupling of the energy levels, and have wavelengths in the far-infrared region which make them suitable for scattering the CMB photons at high redshifts ($2 \lesssim z \lesssim 30$). These lines had been used by Varshalovich, Khersonskii & Sunyaev (1978) as a means to couple matter and radiation at redshifts around $150 - 300$, where the their different adiabatic indices can lead to absorption of CMB in these lines. There are also the hyper-fine transitions arising from spin-spin interaction, but their extremely low cross-sections make these transitions unsuitable for any application with scattering of CMB photons. The other important application we have made is to consider the effect of scattering in the CO rotational lines, which are similar to the molecular lines mentioned above, but have wavelength extending into the sub-millimeter region owing to the larger mass of CO molecule. This feature, together with the fact that CO is the second most abundant molecule in the local universe, makes analysis of scattering in the CO lines very attractive in the low redshift universe ($z \lesssim 2$). We shall see that for galaxies in the local universe, the first three rotational lines of CO which are located near the CMB spectrum and therefore have a large number of photons available for scattering, can give us unique information about the motion of these galaxies in the CMB rest frame.

We found that the scattering effect analyzed in this work is identical to the kinematic-SZ effect described by Sunyaev & Zel'dovich (1970, 1980), but now the signal is obviously a function of frequency due to the nature of resonant scattering. There are several advantages of this effect, as it might allow us to probe definite redshift intervals by choosing suitable transitions. This idea is illustrated in Fig.(1.1) for the integrated signal of scattering as might become observable for satellites like PLANCK. The broad-band channels of this experiment will see the effect of scattering from a particular redshift slice $\Delta z/z = \Delta\nu/\nu$, $\nu$ being the frequency of the resonant transition.

Therefore the higher frequency channels will be sampling the lower redshifts, and provided the future CMB experiments like ACT measure the CMB sky in many closely packed frequency channels, one would have the possibility to follow the enrichment and ionization history of the universe from such observations. The transverse dimension of the slice will be determined by the beam-width of the experiment, or in case of the integrated signal the angular size of the observing multipole $l$, corresponding roughly as $\theta \approx \pi/l$. When we shall be speaking of the integrated signal of scattering, our interest will be in all unresolved objects inside this volume, which contribute to the coherent distortion in the angular fluctuation of the CMB. On the other hand, future sub-millimeter interferometers like ALMA shall be able to resolve individual parts of galaxies upto very large distances, and the high sensitivities of these instruments might allow us to detect the signal of scattering from individual gas clouds. The precise frequency dependent nature of the signal will allow us to distinguish it from other emissions which might be coming from the same sources.

We now try to give a rough idea of the effect of scattering on the angular distribution of the temperature fluctuations in the CMB sky. As depicted in Fig.(1.2), the CMB photons arrive to us from the inside of a sphere termed as the last scattering surface (LSS), traveling almost freely except from very occasional effect of scattering (we neglect the scattering by electrons here). The angular distribution of temperature fluctuations inside this sphere is very accurately predicted by cosmological models, which gives us the value of temperature fluctuations in average between two points separated by an angle $\theta$, which we call $\Delta T(\theta)$, for any value of $\theta$. Introducing the effect of scattering in this angular distribution, we get

$$\frac{\Delta \mathrm{T}}{\mathrm{T}_0}(\theta, \nu) \; = \; e^{-\tau_\nu} \; \frac{\Delta \mathrm{T}}{\mathrm{T}_0}(\theta)\bigg|_{orig.} \; + \; \frac{\Delta \mathrm{T}}{\mathrm{T}_0}(\theta, \nu)\bigg|_{new} \tag{1.2}$$

Here the temperature anisotropies are scaled in terms of the present day CMB temperature, $\mathrm{T}_0$. The first term on the right hand side represents the smoothening or "blurring" of the original temperature anisotropies due to scattering, which were originally free from any frequency dependence. The CMB photons loose their original direction after scattering, and this causes the blurring of the primordial temperature anisotropy in the sky. But this is not the only effect, as the scatterers are in motion with respect to the CMB rest frame as a result of infall of matter into the large-scale potential wells and growth of structures (Sachs & Wolfe 1967), and this peculiar motion gives rise to its own temperature anisotropies as we have seen from eqn.(1.1). This new anisotropies are represented by the second term in the right hand side. Obviously the new anisotropies are function of frequency, hence redshift, due to the nature of resonant scattering, which give rise to particular features in the power spectrum distortion at large angles, where the Sachs-Wolfe effect is also playing a role.

# 1. INTRODUCTION
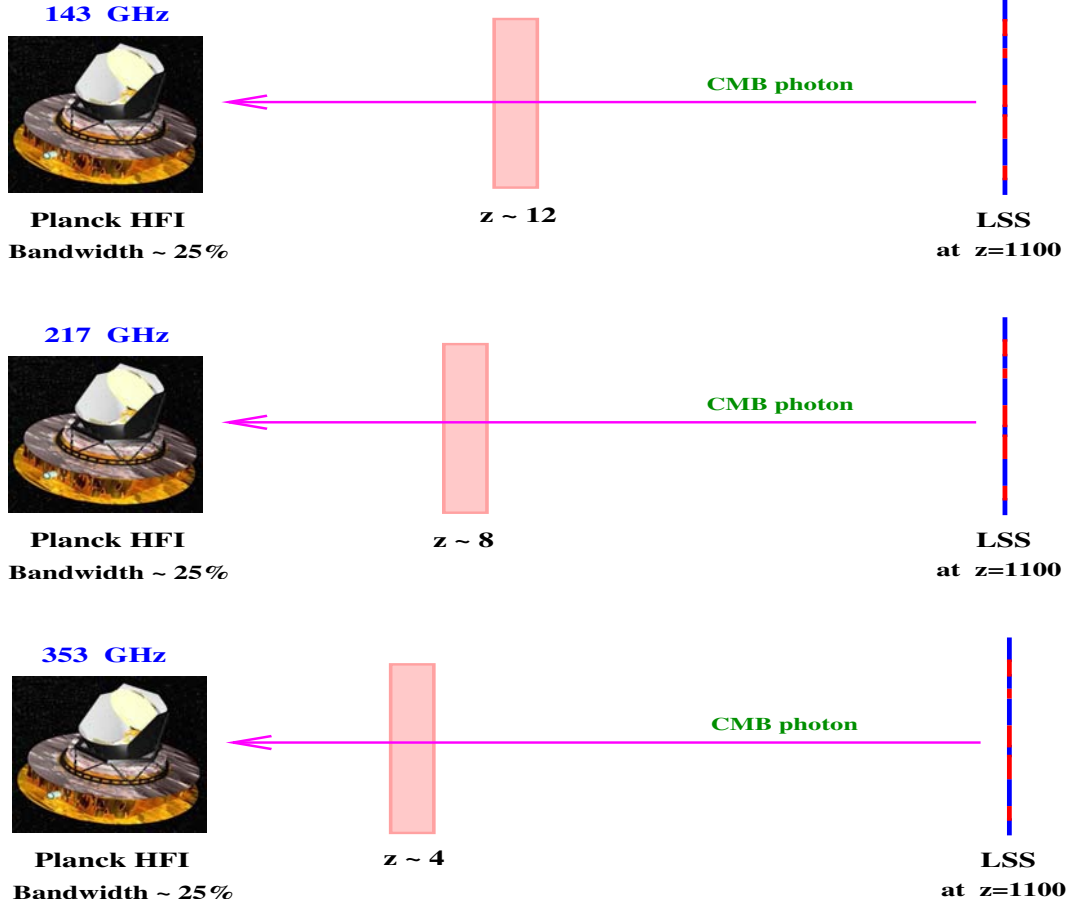


Figure 1.1: Schematic diagram illustrating the advantage of frequency dependent scattering to probe definite redshift intervals. The CMB photons are produced at the epoch of recombination at $z \simeq 1100$, which we term as the Last Scattering Surface, and are received by an observing probe like the PLANCK satellite. The signal of resonant scattering is embedded into the observed temperature fluctuations of the CMB, but unlike scattering by electrons, which is equally effective at all redshifts due to the frequency independent Thomson scattering cross-section, resonant scattering by atomic, ionic or molecular lines work only at definite redshift intervals. This redshift interval is defined by the frequency resolution of the experiment, $\Delta z/z = \Delta \nu/\nu$. In fact, for the integrated scattering signal from many unresolved point sources, the effect correspond to a definite volume along the line-of-sight, whose transverse extent depends on the angular scale of observation. For a particular resonant transition, the higher observing frequencies probe the lower redshifts, in accordance with $\nu_{obs} = \nu/(1 + z)$. The illustration above shows the case for scattering by $C^+$ fine-structure line with PLANCK HFI, which has scattering frequency 1.9 THz.
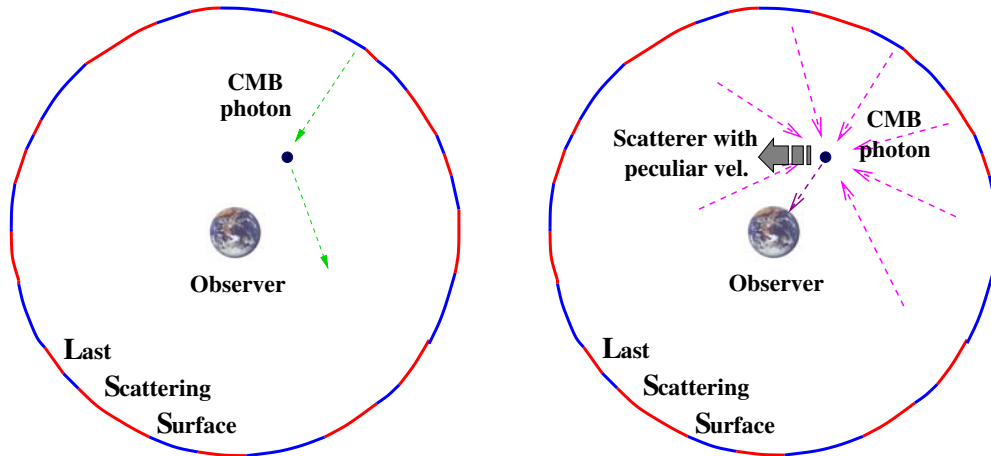
Figure 1.2: Schematic diagram illustrating the process of resonant scattering of the CMB photons. One can imagine the primordial temperature fluctuations in the CMB as patterns inside a sphere at redshift $z \simeq 1100$, which is the Last Scattering Surface. We are at the center of this sphere, and the CMB photons travel almost freely towards us from this surface. However if a photons is scattered by atomic, ionic or molecular lines, it will cause no change in its energy, but will redistribute its direction, as shown in the diagram at *left*. This will result in a smoothing or blurring of the primordial temperature anisotropies. Moreover, these scatterers will induce their own temperature anisotropy, because of their motion in the CMB rest frame, as shown in *right*. This motion chiefly corresponds to the large-scale infall velocities of matter into dark matter potential wells, and depends on the redshift of scattering. The observed angular fluctuations are therefore a combination of the smoothed primordial anisotropies and a newly generated motion-induced term.

Having obtained the expression of temperature anisotropies due to scattering, we try to formulate the corresponding distortion in the power spectrum, $C_l$-s, which are defined as

$$\frac{\Delta T}{T_0}(\theta, \phi) = \sum_{l=0}^{\infty} \sum_{m=-l}^{l} a_{lm} Y_{lm}(\theta, \phi)$$

$$C_l = \frac{1}{2l+1} \sum_{m=-l}^{l} |a_{lm}|^2$$

This is the conventional expansion of the temperature fluctuations in spherical harmonics, the second relation defining the sky correlation function $C_l$-s in terms of the multipole moments $a_{lm}$. As a result of resonant scattering, these observed $C_l$-s now are now function of frequency, and we can write the modification in the CMB power spectrum as

$$\delta C_l(\nu) \equiv C_l^{\text{obs.}}(\nu) - C_l^{\text{prim.}} = \tau_\nu \cdot \mathcal{C}_1(\nu) + \tau_\nu^2 \cdot \mathcal{C}_2(\nu) + \mathcal{O}(\tau_\nu^3) \tag{1.3}$$

$\delta C_l(\nu)$ is the expected distortion in the CMB power spectrum at frequency $\nu$, which one obtains after subtracting the original primordial $C_l$-s from the observed $C_l$-s with the scattering signal inside it. In practice, this can be achieved by subtracting the $C_l$-s from two different frequencies

with large enough separation, where one observation can be taken to be free of the scattering effect. This is one direct advantage of the frequency dependent nature of resonant scattering, which allows us to pick up extremely small signals by means of comparison at two different frequencies. We see that the resulting $\delta C_l$-s can be expressed as a power series in the line optical depth, with the coefficients $\mathcal{C}_1(\nu)$, $\mathcal{C}_2(\nu)$ etc. as function of frequencies (hence redshifts). Since the optical depths in scattering are very small, we are only interested in the first order term, and in fact for small angular scales ($l \gtrsim 100$) we obtain a particularly simple form for power spectrum distortion

$$\delta C_l \; \simeq \; -2 \; \tau_\nu \; C_l^{\mathrm{prim.}} \tag{1.4}$$

We see that such linear dependence on optical depths provide a massive boost in the amplitude of our effect, since the multipole $C_l$-s are squares of the temperature fluctuations, so a priory we should expect the $\delta C_l$-s to be proportional to $\tau_\nu^2$. This huge enhancement is the main difference of our approach from that of Dubrovich and Maoli et al. Such linear dependence arises from a non-zero correlation between the density fluctuations existing between the epoch of recombination and the epoch of scattering (Hernández-Monteagudo & Sunyaev 2004), and we see that it can enhance the scattering signal in the CMB power spectrum by a factor upto a million, if we remember that $\tau_\nu \sim 10^{-6}$ for typical cosmic abundances. This forms the basis for our effort to constrain the enrichment and ionization history of the universe.

The organization of this thesis is as follows. In Ch.2 we present the formulation for the scattering effect, and discuss the nature of the spectrum along random line of sight in comparison with pure absorption spectrum. We also estimate the contribution arising from blurring of primordial anisotropies inside a single scattering cloud. We derive the necessary expressions for brightness temperature and intensities of the scattering signal, and as an application apply them in determining the column densities of CO and molecular gas mass from scattering. Our main example for scattering by individual objects is the detection of peculiar motions of galaxies, which is discussed in Ch.3. In that chapter we try to make use of simultaneous observation of scattering and emission to estimate the optical depths, and also consider the density limits for the effectiveness of scattering. These formalisms are then applied to the Local Group and the Virgo cluster galaxies, where the high velocities of the later make them promising candidates for observing the scattering signal. We demonstrate the method of obtaining the peculiar motions of the galaxies taking into account our own motion in the CMB rest frame. We also tabulate the expected change in the brightness temperatures in the CO lines in these galaxies for some representative column densities.

The issue of different density limits for the effectiveness of scattering is discussed in detail in Ch.4. Here we have defined two new critical densities in addition to the classical definition, and showed that the effect of scattering can dominate upto large densities, but for an individual object the number of photons generated by scattering gets dwarfed by photons from line emission

at much lower densities. This density limit corresponds to the point upto which we can see an individual object in scattering, and is very low for diffuse electron plasma, and also low for neutral gas containing CO. But when one considers the integrated scattering effect coming from many unresolved point sources in the sky, the coherent distortion in the CMB power spectrum can be caused by objects with densities several times higher, because the contribution of emission from small dense objects is smaller at large angles. This makes it necessary to compute the distortion in the CMB power spectrum as a result of scattering, which we have done in Ch.5.

We have computed the changes in the CMB power spectrum under the limit of very low optical depths, using the CMBFAST code of Seljak & Zaldarriaga (1996) with appropriate modifications. This approach had been used previously by Zaldarriaga & Loeb (2002) to compute the change in the power spectrum arising from scattering in the neutral Li $6708\mathring{A}$ line. Although this fine-structure transition of Li can give $\tau_\nu$ greater than unity, it has too short wavelength to be observable by planned CMB experiments, and is outside the high intensity CMB spectrum even for redshifts $800 < z < 1100$. The method to overcome the very small optical depth of far-IR fine-structure lines is one of the main focus of this work, which can be achieved by comparing the power spectrum of the same part of the sky from two different frequency channels, which gets rid of the limitation due to the cosmic variance. In Ch.5 we have discussed in detail this approach and the method to set minimum detectable abundances from any given sensitivity of CMB experiments. We also estimated the limits when removal of foreground signals in the sky is not complete, thereby worsening the minimum detectable abundances by a factor of $50 - 200$.

After obtaining the relation between CMB power spectrum distortion and the abundances of the scattering species, we tried to set constrains on the enrichment and ionization history of the universe in Ch.6. We are interested in redshifts $\sim 10 - 20$ because of the recent WMAP finding of early reionization (Kogut et al. 2003). We have considered several enrichment histories, both with early ($z \sim 20$) and late ($z \sim 6$) reionization, and computed the distortion in the power spectrum in large and small angular scales. The importance of the small angular scale observations lies in the fact that they might become accessible with ground-based CMB experiments well before PLANCK, and the simple formulation of eqn.(1.4) allows one to compute the expected signal immediately. Finally, in Ch.7 we tried to give some preliminary estimate of the signal coming from free-free, line and dust emission from overdense regions. We have made simple models for the emissivity of star-forming halos based on their rate of massive star formation, and estimated the distortion in the CMB power spectrum under the assumption that these point-like sources are Poissonian distributed in the sky. The main conclusion from this part is that the signal of emission is significantly lower than that of scattering at large angles. In the two appendices, we have added the analytical expression for power spectrum distortion and the validity of the linear approximation, as well as the method to compute level populations in a multilevel system under the condition of statistical equilibrium.

# Chapter 2

# Resonant Scattering of the CMB Photons

## 2.1 Characteristics of the scattering signal

First we discuss the basic underlying effect of resonant scattering and the corresponding change in the background intensity of CMB photons in the direction of the enriched gas. The effect we discuss here had been used by various authors to estimate primarily the distortion in the CMB thermal spectrum due to presence of primordial molecules, but a formal derivation of the effect had been absent. It was first analyzed by Dubrovich (1977, 1993) and later followed-up by various Italian and French groups (Maoli et al. 1994, de Bernardis et al. 1993), who sought to find signals from primordial molecules like HD, LiH etc. in the CMB spectrum. Here we have analyzed the basic underlying principle of this effect and tried to find some other applications. The effect under consideration is equivalent to the well-known kinematic-SZ type distortion (Sunyaev & Zeldovich 1970,1980), as was stated by Dubrovich (1977), but now it is a function of frequency due to the nature of resonant scattering. Scattering of CMB photons in an atomic or molecular line has the combined effect of both loss of CMB photons from the line of sight, and also a gain due to the photons that are scattered into the line of sight. If the scatterer is at rest with respect to the isotropic radiation background, these two effect exactly cancel each other and no change in flux is observed. However, due to the peculiar motion of the enriched gas it will have some non-zero velocity with respect to the CMB rest frame, and as a result will cause a net increase or decrease in the intensity of the background radiation as observed through the gas.

### 2.1.1 Basic formulation for kSZE type distortion

We present below a simple description of the effect demonstrating its equivalence with the kinematic-SZ type distortion. Let us assume the gas cloud has peculiar velocity $\vec{\beta}$ with respect to the CMB

background (fig.2.1). The incident radiation on the cloud is $I_\nu$, which in our case is simply the Planckian spectrum at frequency $\nu$, and $T_\gamma$ as the mean temperature of background CMB photons

$$I_\nu = \frac{2h\nu^3}{c^2} \exp\left[\frac{h\nu}{kT_\gamma} - 1\right]^{-1} \tag{2.1}$$

The observed intensity in the direction of the cloud, as mentioned above, consists of two parts: *i)* the scattered intensity in the direction of the observer (denoted by $I_\nu^{Scatter}$ in fig.2.1), and *ii)* the attenuated intensity of the background CMB radiation: $e^{-\tau}I_\nu$. Assuming non-relativistic velocity ($\beta \ll 1$), the frequency transformation relating the cloud frame (denoted by *prime*) and the CMB frame is simply

$$\nu' = \nu(1 + \vec{\beta} \cdot \vec{n}) \tag{2.2}$$
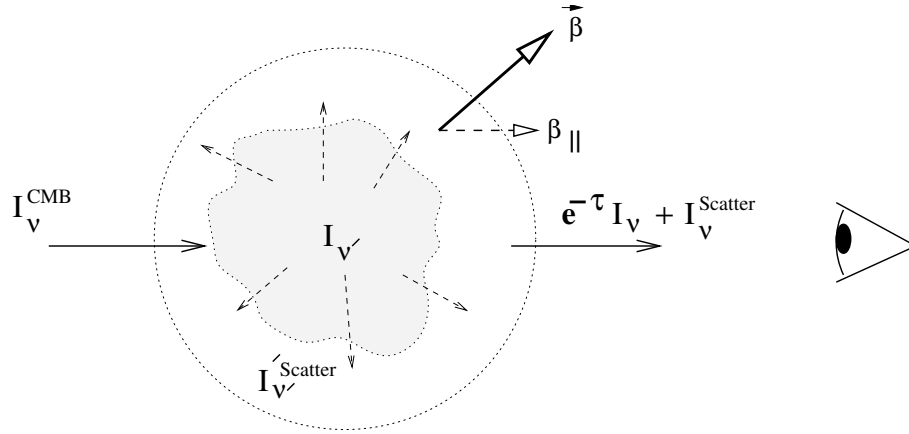


Figure 2.1: Schematic diagram illustrating the change in background intensity through resonant scattering in a moving medium

We can write the intensity in the cloud frame, $I'_{\nu'}$, by using the phase-space density conservation relation $I'_{\nu'} = (\nu'^3/\nu^3)I_\nu$, which gives

$$I'_{\nu'} = (1 - \beta\mu)^3 \ A \ \frac{x^3}{e^x - 1} \tag{2.3}$$

Here $x \equiv h\nu/kT_\gamma$ is the dimensionless frequency in the observer frame, and $A = 2(kT_\gamma)^3/(hc)^2$ is a constant. $\mu$ is the direction cosine for the angle between direction of motion and the observer, and it shows the intensity in the cloud frame is not isotropic but has a dipole component due to the motion of the cloud. The effect of resonant scattering would be to redistribute this intensity, and the scattered intensity can be written, in the optically thin limit, after integrating over all angles as

$$I'^{Scatt}_{\nu'} = \tau(\nu') \ A \frac{x'^3}{e^{x'} - 1} \tag{2.4}$$

## 2. RESONANT SCATTERING OF THE CMB PHOTONS

where $x' \equiv h\nu'/kT_0$, and $\tau(\nu')$ is the line optical depth. The right hand side of eqn(2.4) is solely a function of cloud-frame frequency $\nu'$, and hence can be transformed back to observer frame by using the same conservation law $I_\nu = (\nu^3/\nu'^3)I'_{\nu'}$.

For simplicity, let us consider the case of scattering by one single atom or molecule, without any line broadening effect by an ensemble of scatterers. In this idealized case the line profile will simply be a $\delta$-function, and the optical depth will be the product of the line profile with the oscillator strength of the resonant transition ($\tau \ll 1$ for the subsequent analysis)

$$\tau(\nu') = \frac{\pi e^2}{m_e c} \, f_i \, \delta(\nu' - \nu_0) \tag{2.5}$$

This allows us to write the scattered intensity back in observer frame by simply using the properties of $\delta$-function

$$\begin{aligned} I_\nu^{Scatt} &= \frac{1}{(1 - \beta\mu)^3} \, \frac{\pi e^2}{m_e c} \, f_i \, \delta(\nu' - \nu_0) \, A\frac{x'^3}{e^{x'} - 1} \\ &= \tau^*(\nu) I_\nu \left(1 + \frac{xe^x}{e^x - 1} \, \beta\mu\right) \, + \, \mathcal{O}(\beta^2) \end{aligned} \tag{2.6}$$

$\tau^*(\nu)$ is defined as $\tau^*(\nu) \equiv (\pi e^2/m_e c)\delta(\nu - \tilde{\nu}_0)$, with $\tilde{\nu}_0 = \nu_0(1 + \beta\mu)$. This shows the *shift* in the emission profile away from the rest-frame resonant frequency due to the motion of the scatterer. The absorption profile is also shifted by an equal amount, because only photons with frequency $\nu' = \nu_0(1 - \beta\mu)$ are in resonance with the moving atom/molecule, and hence lost from the line of sight. The total intensity in the direction of the cloud is then simply the sum of the absorption and scattering terms

$$I_\nu^{total} = (1 - \tau_\nu^*) \, I_\nu \, + \, I_\nu^{Scatt} \tag{2.7}$$

which gives the relative change in intensity in the first order as

$$\frac{\Delta I_\nu}{I_\nu} = \frac{\pi e^2}{m_e c} f_i \, \delta\left(\nu - \nu_0(1 + \beta_\parallel)\right) \beta_\parallel \, \frac{xe^x}{e^x - 1} \tag{2.8}$$

We have used $\beta_\parallel$ to denote the velocity component in the direction of the observer. This form is similar to the kinematic-SZ effect, as becomes evident if we rewrite the above equation in terms of temperature distortion upto first order

$$\frac{\Delta T(\nu)}{T_\gamma} \, = \, \tau^*(\nu) \, \beta_\parallel \tag{2.9}$$

In the realistic situation, any molecular cloud or gas will consist of many atoms or molecules in random thermal motion, and will present a different line-of-sight velocity component towards the observer. The net result will be, of course, a thermally broadened line profile with a gaussian shape. As in the case of $\delta$-functions, the thermally broadened absorption and emission (scattering) parts will match perfectly and result in a net increment or decrement of flux depending on the direction

of motion of the scattering cloud. This can be formally established by writing the emission from the cloud in terms of partial frequency redistribution function

$$\epsilon_\nu = n_i \; f_i \; \int_0^\infty d\nu_1 \; \int_{-1}^{+1} d\mu_1 \; \varphi(\nu_0) \; R(\nu, 1; \nu_1, \mu_1) \; I'(\nu_1, \mu_1) \tag{2.10}$$

where $R(\nu, \mu; \nu_1, \mu_1)$ is the photon redistribution function, giving the probability that a photon incident on the atom or molecule from direction $\mu_1$ and having frequency $\nu_1$ will be scattered with frequency $\nu$ in the direction of the observer ($\mu = 1$). $I'(\nu_1, \mu_1)$ is the incident radiation, and $\varphi(\nu_0)$ is the line profile for single scattering, which we can again represent with a delta function, $\varphi(\nu_0) = \delta(\nu_1 - \nu_0)$, assuming zero natural line width. $n_i$ is the total number of atoms or molecules in the lower tradition state available for scattering, and $f_i$ is the oscillator strength for the transition. For pure doppler broadening, the frequency redistribution function takes the form of a truncated gaussian (see, e.g. Mihalas 1970), and the resulting emission profile, shown in Fig.(2.2), is a complete gaussian centered at frequency $\nu_0(1 + \beta_\parallel)$.
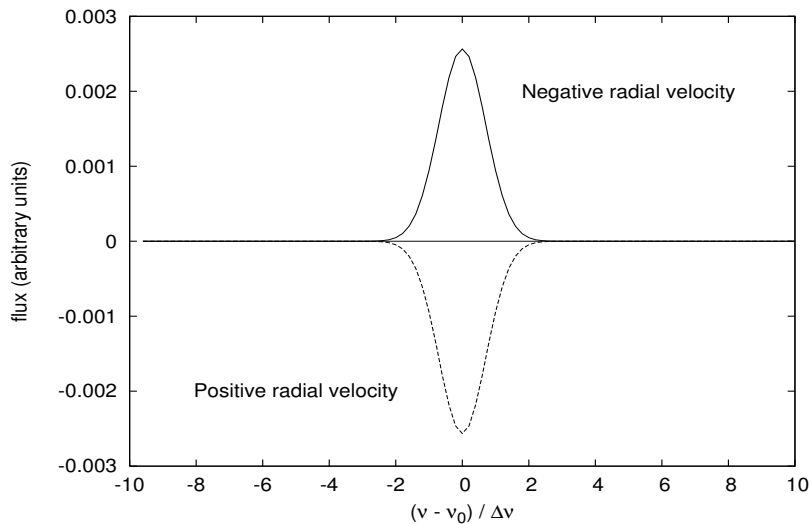


Figure 2.2: Profile of the emission function of a molecular cloud created by scattering of background CMB photons, taking into account the doppler broadening caused by the thermal motions of atoms or molecules. Positive radial velocity corresponds to motion away from the observer, and negative velocity for motion towards the observer. We get a positive intensity for scattering by cloud moving towards us, and vice versa. Broadening due to any kind of turbulent motion in the gas cloud is neglected, but can easily be taken into account.

## 2.1.2 Spectrum expected from CMB scattering

We have used the effect discussed here in a published work (Basu, Hernández-Monteagudo & Sunyaev 2004), where we estimated the integrated effect of scattering, or the distortion in the

## 2. RESONANT SCATTERING OF THE CMB PHOTONS

CMB power spectrum, by post-reionization atoms and ions in the redshift range $5 - 30$. The detailed spectrum of distortion caused by scattering on the moving atom, ion or molecule was not of interest, because we were discussing observation with broad-band detectors, whereas in the present chapter we are interested in discrete objects. In that work we solely focussed on the temperature fluctuations averaged over angles exceeding the dimensions of individual objects and halos, because we sought to set constraints on the mean metallicity abundances in the diffuse low density gas, particularly the IGM. In this subsection, we qualitatively discuss the nature of the spectrum resulting from scattering of CMB photons in resonant lines in a molecular cloud. We particularly compare the nature of the predicted signal with the Ly-$\alpha$ absorption lines in the spectrum of a quasar, and emphasize the distinctive features that might allow to separate out this much weaker signal. We also show the spectrum expected from a particular object, say a galaxy, both when we are able to resolve the object and otherwise.
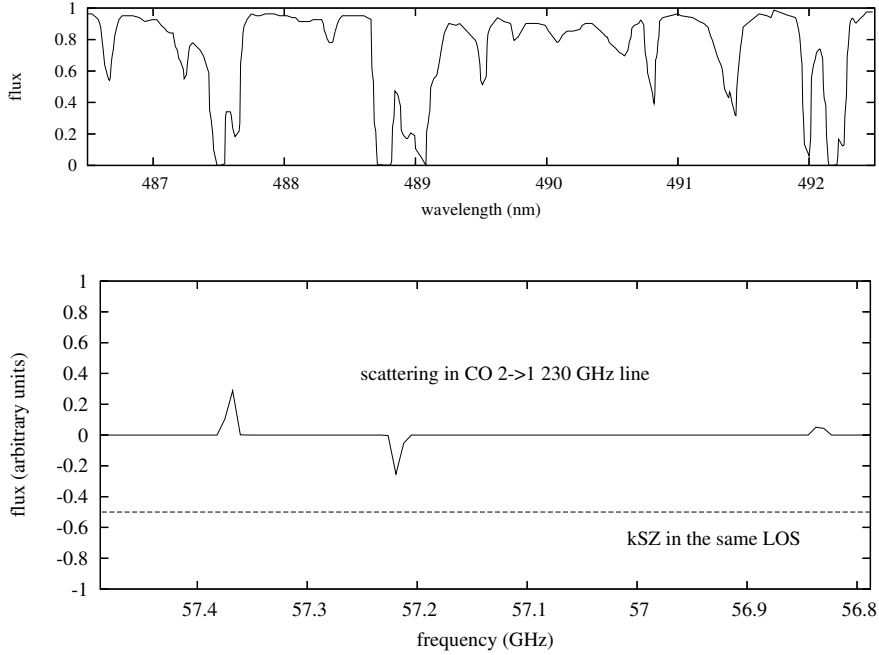


Figure 2.3: Spectrum of Ly-$\alpha$ forest towards a point source (quasar), and spectrum of scattering of CMB by the same set of gas clouds along the line-of-sight without any quasar in the background. The gas clouds are located at $z \sim 3$.

In Fig.(2.3) we show a schematic view of the spectrum expected along the line-of-sight, in case there is a background quasar present, and for the same line of sight without any background quasar but only for CMB. The absorbing molecular clouds are situated around $z = 3$, and the top panel shows a typical Ly-$\alpha$ absorption forest in the spectrum of a quasar situated in the background.

We note that there is only absorption features present, or reduction of background flux, since quasars being point sources, there can only be loss of photons from the line of sight. In the bottom panel, we show a schematic view of scattering features in the same set of molecular gas along the line-of-sight. The main distinguishing feature is that there is both increment and decrement of background flux (CMB blackbody), depending upon the direction of motion of the cloud. We assumed only the most damped Ly-$\alpha$ systems are dense enough to have neutral molecular gas shielded from the ionizing background. Also shown for comparison is the kinematic SZ signal coming from inter-galactic electrons, which is flat in frequency spectrum.

### 2.1.3 Temperature distortion from primordial anisotropies

In the preceding discussion we have assumed for simplicity that the intensity of background radiation is isotropic, and neglected the presence of primordial anisotropies. These primordial anisotropies have amplitudes of the order of $10^{-4} - 10^{-5}$ in the microwave sky, and will be suppressed by the same resonant scattering we have been discussing when one looks through the gas cloud. Since one of our main objectives is to discuss the amplitude of scattering signal from nearby galaxies, whose angular dimension can extend from several arc minutes to one degree scale, we must also consider this additional temperature fluctuation present on those scales. For objects of smaller angular size (few arc seconds) one can neglect the contribution from primordial anisotropies.

We here present only an order of magnitude estimate for this secondary effect. For formulation of the problem we follow Zel'dovich & Sunyaev (1980), where the same effect was discussed for Thomson scattering by cold electrons in clusters, without any peculiar motion of the scattering cloud. The starting point is to note that the primordial intensity field contains angular fluctuations at all angular scales

$$I(\mu') = I_0 \left[ 1 + a\mu' + b \left( \mu'^2 - \frac{1}{3} \right) + \sum_{n=3}^{\infty} C_n P_n(\mu') \right] \tag{2.11}$$

where $P_n$ are the Legendre polynomials, and $\mu' = \cos\theta$ and the angle $\theta$ is measured from some suitable axis. This observed intensity at the direction $\mu'$ will be suppressed by the same scattering optical depth $\tau_\nu$ as discussed previously, if a gas cloud happens to be in the same direction. Now, the resonant scattering couples only with the monopole and quadrupole of the intensity in the same way as electron scattering, and hence the scattered intensity in the direction of the gas cloud will be

$$I_1(\mu') = I(\mu') \left( 1 - \tau_\nu \right) + I_0 \tau_\nu \left[ 1 + E_1 b \left( \mu'^2 - \frac{1}{3} \right) \right] \tag{2.12}$$

Here the first term is simply the suppression of primordial fluctuations in the direction of the cloud, stating that the fraction $\tau_\nu$ of photons are lost from the line of sight due to scattering. The second term contains the scattered monopole and quadrupole part (obviously no dipole will be present if the scatterer is at rest with respect to CMB), and also proportional to $\tau_\nu$. $E_1$ is a constant for

## 2. RESONANT SCATTERING OF THE CMB PHOTONS

the particular resonant transition involved, and have amplitude of the order 0.1 for pure Rayleigh indicatrix.

Therefore The fluctuation in the background intensity inside the object will be $\Delta I/I_0 = (I_1(\mu') - I(\mu'))/I_0$, and using the same factor $(e^x - 1)/xe^x$ we can write the corresponding temperature fluctuation as

$$\frac{\Delta T(\nu)}{T_0} = -\tau_\nu \frac{e^x - 1}{xe^x} \left[ a\mu' + (1 - E_1)b \left(\mu'^2 - \frac{1}{3}\right) + \sum_{n=3}^{\infty} C_n P_n(\mu') \right]$$

$$= -\tau_\nu \left[ \bar{a}\mu' + \bar{b}\left(\mu'^2 - \frac{1}{3}\right) + \sum_{n=3}^{\infty} \bar{C}_n P_n(\mu') \right] \tag{2.13}$$

Comparing this expression with the formula for motion induced dipole anisotropy, $\Delta T(\nu)/T_0 = \tau_\nu \beta_\parallel$, we see that for any object of given size, the magnitude of this secondary effect compares roughly as the ratio of primordial temperature fluctuation at that scale to $\beta_\parallel$. We also note that one can not separate out the contribution of primordial dipole from the motion induced dipole at line frequency, since the component of primordial dipole in the direction of motion (angle between the directions corresponding to $\mu$ and $\mu'$, where $\mu$ marks the direction on motion of the object) will always be present in the observed signal. However if one takes the magnitude of primordial dipole to be low ($\sim 10^{-5}$ or less), the observed dipole will be a good tracer of the peculiar motion of the scatterer.

We can confirm that the temperature fluctuation generated by motion is dominant over this suppression of primosdial anisotropies at all angular scales by some simple order of magnitude estimate. To estimate $\beta_\parallel$, we assume the linear regime of structure formation, which gives $v(z)/c \approx v(0)/c \, (1+z)^{-\frac{1}{2}}$. (This relation is true only for matter dominated universe, but we can ignore the corrections due to a particular cosmological model for the present estimates at $z > 1$.) $v(0)$ is the present-day value of large-scale peculiar velocity, which one can take roughly as 600 km s$^{-1}$, but we remember that this velocity distribution is Gaussian and we have the probability of higher velocities in individual objects. Since the scattering effect will be proportional to the radial component of this motion towards us, we can write $v_\parallel(z) = v(z)/\sqrt{3}$, yielding $v_\parallel(z)/c = 1.15 \times 10^{-3} \, (1+z)^{-\frac{1}{2}}$. Hence for objects one can resolve, i.e. for galaxies in the local universe, we have $\beta_\parallel \approx 10^{-3}$. The intrinsic dipole can not be separated, so we compare the amplitude of scattered intrinsic quadrupole with this value. The effect will be maximized for $\mu' = 1$, and standard $\Lambda$CDM model we have $l(l+1)C_l/2\pi = 1000\mu K^2$ at $l = 2$. Hence the contribution of scattered quadrupole is more than 80 times smaller for the above value of $\beta_\parallel$. However, the temperature power spectrum has its maximum around 1° scale, but even there the maximum probable temperature fluctuation from the background mean is only 80 $\mu$K. This immediately shows the amplitude of motion-induced signal to be about 30 times higher in average.

The important point to remember about primordial temperature anisotropies is that they are frequency independent. This means we can separate the small contribution coming from suppression of primordial fluctuations by observing the same patch of sky away from the resonant frequency. CMB anisotropy probes like WMAP has presented us with high angular resolution all sky CMB maps, and hence the contribution from any particular hot or cold spot can be estimated and subtracted from such maps.

## 2.2 Amplitude of the scattering signal

After discussing the general properties of the scattering signal, we now present the formulation for observable properties of the object like brightness temperature of the object or the beam-averaged flux as might be expected from observation of individual objects. This will help us to set limits on the column density of the scatterer, or mass of the neutral molecular gas, in terms of the characteristics of a fiducial experiment. After presenting the necessary formulation, we inspect which atomic, ionic or molecular lines are most suitable at various redshift ranges. Then we shall proceed to one application: detection of molecular gas from scattering in the nearby universe from scattering. Our main example for application of scattering from individual objects, the detection of peculiar motion of galaxies, is discussed in the next chapter.

The optical depth in scattering is expressed as the product of the number density of the atoms or molecules with the scattering cross-section along the line-of-sight:

$$\tau_\nu = \int n_i \; \sigma(\nu) \; dl \qquad (2.14)$$

Here $n_i$ is the number density (in cm$^{-3}$) of the species $i$ under study, and $\sigma(\nu)$ is the scattering cross-section at line frequency $\nu$. The cross-section for resonant scattering is expressed in terms of the oscillator strength of the transition invovlved, which have the following form (see, e.g., Rybicki & Lightman 1985 for definitions)

$$\sigma(\nu) = \frac{\pi e^2}{m_e c} \; f_i(\nu) \; \varphi(\nu) \qquad (2.15)$$

$$f_i(\nu) = \frac{m_e c}{8\pi e^2} \; \frac{g_u}{g_l} \left( 1 - \frac{\varpi_u}{\varpi_l} \frac{g_l}{g_u} \right) \; \frac{c^2}{\nu^2} \; A_{ul} \qquad (2.16)$$

Here $f_i(\nu)$ is the oscillator strength of the particular transition, which is expressed in terms of level degeneracy and transition rate. $\varpi_u$ and $\varpi_l$ are the fraction of atoms/molecules present in the upper and lower transition levels, and $g_u$ and $g_l$ are the respective statistical weight. $A_{ul}$ is the radiative de-excitation probability from upper to lower level, which dominates over collisional de-excitation in the low density regimes that we are interested in. The term inside the parenthesis takes into account the necessary correction for the induced emission in presence of the CMB due to finite population of the upper level. The line profile, $\varphi(\nu)$, can be assumed to be a gaussian.

## 2. RESONANT SCATTERING OF THE CMB PHOTONS

Therefore expressed in terms of the column-density of the scatterer, $N_i = \int n_i dl$, the optical depth due to resonant scattering can be written as

$$\tau_\nu = \varpi_l N_i \; \frac{1}{8\pi} \left( \frac{g_u}{g_l} \right) \left( 1 - \frac{\varpi_u}{\varpi_l} \frac{g_l}{g_u} \right) \; \frac{c^2}{\nu^2} A_{ul} \; \varphi(\nu) \tag{2.17}$$

This optical depth creates a distortion in the brightness temperature of the CMB temperature according to the relation $\Delta T / T_{\mathrm{CMB}}(z) = \tau_\nu \beta_\parallel(z)$, as shown in the previous section. $x$ is the shorthand for $x \equiv h\nu/kT_{\mathrm{CMB}}(z) = h\nu_{obs}/kT_0$, where $T_0$ is the temperature of the background radiation today, and $\nu_{obs}$ is the observing frequency. The mean intensity received today due to scattering in the object is readily obtained in comparison with $B_\nu$, the mean intensity of the thermal radiation of the CMB, from the relation (following Zel'dovich & Sunyaev 1969)

$$\frac{\Delta J_\nu}{B_\nu} \;=\; \frac{\mathrm{d}\,\ln B_\nu}{\mathrm{d}\,\ln T} \; \left( \frac{\Delta T}{T} \right) \;=\; \frac{xe^x}{e^x - 1} \; \left( \frac{\Delta T}{T} \right) \tag{2.18}$$

where both $I_\nu$ and $B_\nu$ are at $\nu_{obs}$. Hence using eqn.(2.1) for the $B_{\nu_{obs}}$, and remembering that $\nu_{obs} = \nu/(1+z)$, the received intensity gets the following form

$$\Delta J_\nu^{obs} = \frac{xe^x}{(e^x - 1)^2} \; \frac{2h\nu^3}{c^2} \; (1+z)^{-3} \; \tau_\nu \; \beta_\parallel(z) \tag{2.19}$$

We can simplify the expression in eqn.(2.17) if we write the quantity in the parentheses $(1 - \varpi_u g_l / \varpi_l g_u)$ as $(1 - \exp(-x))$, because we are interested in the limit $T_{EX} \approx T_{CMB}$, i.e. when level populations are completely governed by background CMB temperature, which will be the case for very low density gas in thermal equilibrium with the CMB. Since the usually reported observable quantity is the velocity integrated flux over the telescope beam ($I_{\mathrm{obs}} = \int I_\nu \; dv \; d\Omega$), we write the intensity in the same form

$$I_{\mathrm{obs}} = \frac{hc}{4\pi} \; \frac{\Omega_{beam}}{(1+z)^3} \; \frac{x}{(e^x - 1)} \; \varpi_l N_{\mathrm{CO}} \frac{g_u}{g_l} \; A_{ul} \; \beta_\parallel(z) \tag{2.20}$$

In this expression $\Omega_{beam}$ is the telescope beam-width. This observed intensity, integrated ober the line profile, is the usually reported quantity from experiments. For the small scattering signal, a suitable unit would be mJy·km s$^{-1}$, and we use thhe eqn.(3.3) to estimate the possibility of observation from future far-IR or sub-mm experiments.

The results for such computations are shown in Fig.(2.4) and (2.5), which assumes some mean velocity of the objects in accordance with the typical velocity of large-scale motion in the linear theory of growth of density perturbations. We have used a rather large beam-width of almost 1 square arc minutes for demonstration purposes, but theis plot clearly shows that the two lowest rotational levels of CO are most suitable for scattering CMB photons at low redshifts ($z \lesssim 0.1$), as many more CMB photons are available for scattering at these frequencies. The far-IR fine-structure lines become effective only at high ($z \gtrsim 3$) redshifts, but they can be of importance for future milli-arcsecond resolution experiments like ALMA. We shall return to these issues in a subsequent chapter.
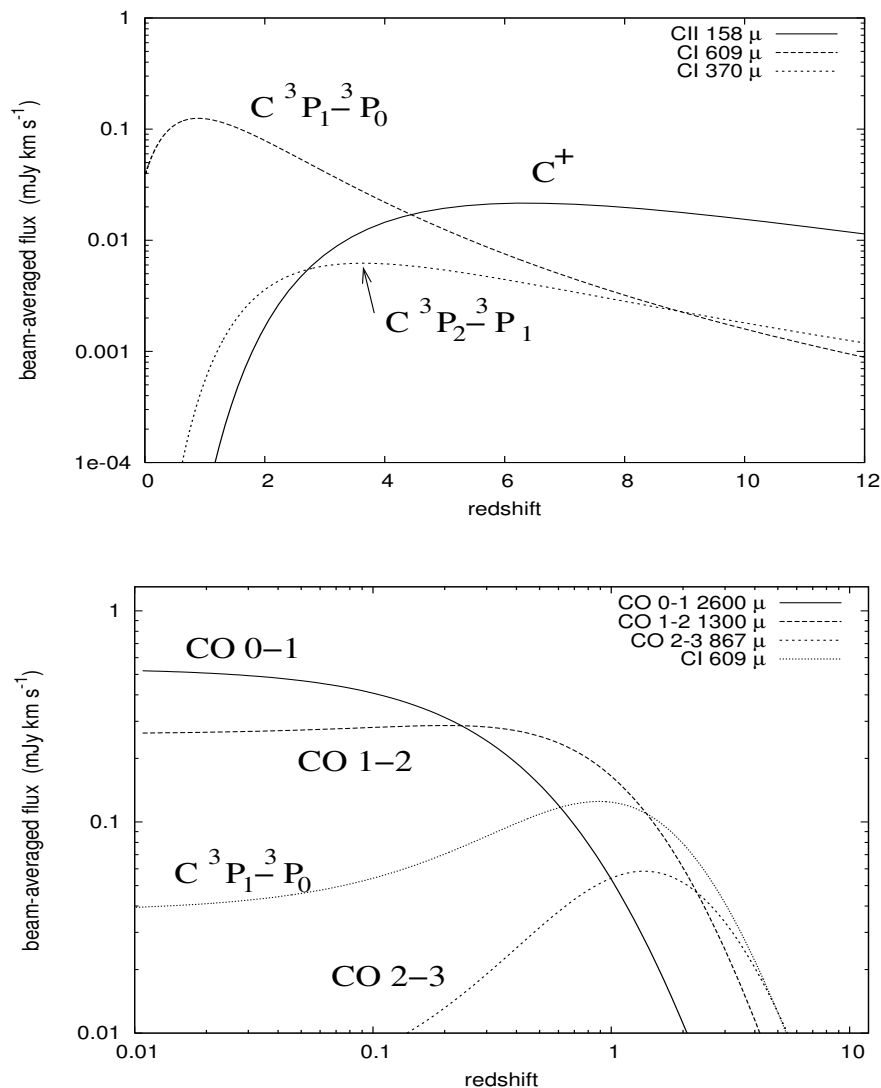
Figure 2.4: Expected flux arising from scattering of CMB photons, averaged over a $50'' \times 50''$ beam, from various species of **carbon**. The column densities for $C^+$ and neutral C are taken as $10^{14}$ cm$^{-2}$, whereas the column density for CO molecule is chosen to be a factor of 10 lower, at $10^{13}$ cm$^{-2}$. We neglect any redshift evolution in abundances for this discussion. This figure demonstrates the usefulness of the first two rotational lines of CO, as well as the 492 GHz fine-structure transition of neutral carbon, to probe individual objects at low redshifts. The peculiar velocity of the objects vary as $\beta_{\parallel}(z) \approx 10^{-3}(1+z)^{-\frac{1}{2}}$.
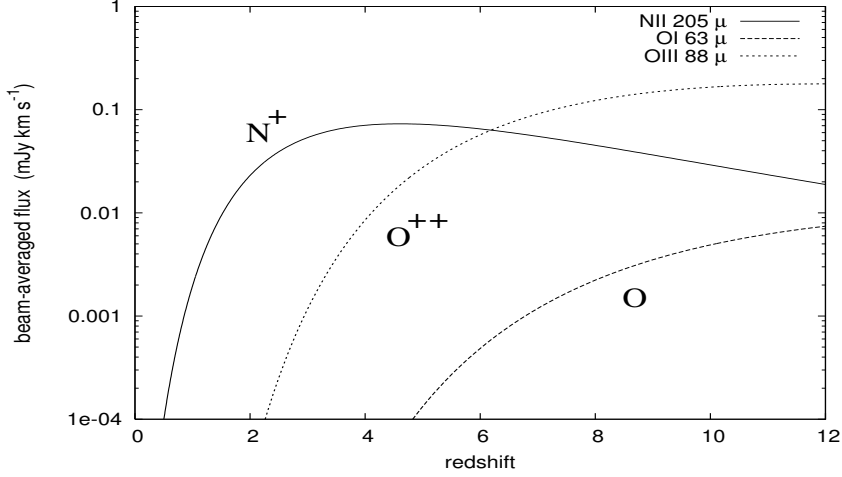
Figure 2.5: Same plot as before, showing the flux expected from scattering by other atomic and ionic fine-structure lines. Plotted above are the three most important FS lines of elements other than carbon: the neutral oxygen $63\mu$, doubly ionized oxygen $88\mu$, and singly ionized nitrogen $205\mu$. The column density for all these species is taken at an uniform $10^{14}$ cm$^{-2}$, without any change in abundance with redshift. The short wavelengths of these lines make them unsuitable for scattering CMB at low redshifts, but for redshifts $z \gtrsim 3$ they become important.

### 2.2.1 Application: column densities of molecular gas

Here we present a simple example for the application of the scattering formulation presented so far. We shall try to estimate the column density of CO moleules, $N_{\mathrm{CO}}$, as can be probed from its lower rotational lines. Our main application for scattering in individual objects, viz. detection of peculiar motion in nearby galaxies, shall be discussed in the next chapter.

We derive the limiting column density of CO molecules that can be probed with future experiments like ALMA[1] from the observation of scattering. We assume that the abundance of CO molecules is low, so that the cloud is optically thin in CO lines ($\tau_\nu < 1$). We also assume a very low density gas where line emission from collisional excitation will be more important only for the lowest rotational transition. To begin, from eqn.(3.3) we write the expression for column density of CO molecules

$$N_{\mathrm{CO}} = \frac{4\pi}{hc}\ \frac{(1+z)^3}{\Omega_{beam}}\left(\frac{e^x - 1}{x}\right)\ \frac{g_l/g_u}{\varpi_l A_{ul}}\ \frac{I_{\mathrm{CO}}}{v_\parallel(z)/c} \tag{2.21}$$

which we can rewrite, remembering $x = kT_0/h\nu_{obs}$, in terms of the observing frequency of the experiment

$$N_{\mathrm{CO}} = 3.6\times10^{15}\mathrm{cm}^{-2}\ \left(\frac{1+z}{2}\right)^3\left(\frac{\Omega_{beam}}{5''\times5''}\right)^{-1}\ \frac{1}{\varpi_u}\left(\frac{A_{ul}}{10^{-7}\ \mathrm{s}^{-1}}\right)^{-1}\left(\frac{\nu_{obs}}{100\ \mathrm{GHz}}\right)^{-1}$$

___
[1]ALMA website: http://www.eso.org/projects/alma/

18

| Experiment / Instrument | Frequency (GHz) | Wavelength ($\mu$m) | Angular Resolution | Sensitivity (mJy) | Freq. res. (km s$^{-1}$) |
|---|---|---|---|---|---|
|  | 35 - 100 | 8500 - 2700 | $0.5''$ - $0.1''$ | 0.77 | 25 |
| ALMA | 100 - 300 | 2700 - 1300 | $0.1''$ - $0.05''$ | 1.2 | 25 |
|  | 300 - 400 | 1300 - 730 | $0.05''$ - $0.04''$ | 2 | 25 |
|  |  |  |  |  |  |
| Herschel SPIRE | 500 - 1500 | 200 - 600 | $20''$ - $40''$ | 140 | 600 |
| Herschel PACS | 1600 - 5000 | 60 - 180 | $50''$ | 3 | 175 |
|  |  |  |  |  |  |
| SOFIA | 500 - 2000 | 60 - 700 | $20''$ | 100 | 20 |

Table 2.1: Spectroscopic sensitivities for current and future IR & sub-mm instruments, in increasing order of frequency. Instruments capable of low resolution spectroscopy are also chosen depending on their frequency coverage. The angular resolution of ALMA is computed assuming an intermediate configuration of 64 antennas, between compacts array and maximum baseline, yielding a resolution of $0.05'' \times (350/\nu_{obs}(\mathrm{GHz}))$. Spectral sensitivities of ALMA are from Butler & Wootten (1999), and values for Herschel and SOFIA are taken from respective project websites.

$$\times \ \mathcal{B} \ \left(\frac{v_\parallel(z)/c}{6 \times 10^{-4}}\right)^{-1} \left(\frac{I_{\mathrm{CO}}}{\mathrm{mJy \ km \ s^{-1}}}\right) \tag{2.22}$$

For example, if we consider the CO $2 \to 1$ 230.7 GHz line, scattering at $z = 1$, the observing frequency will be 115.4 GHz. The population at the upper level is $\varpi_2 = 0.11$, and we have $A_{ul} = 7.36 \times 10^{-7}$ s$^{-1}$. $\mathcal{B}$ is the shorthand for the term in parenthesis in eqn.(2.16), and is roughly 0.8. This corresponds to a column density of $3.0 \times 10^{15}$ cm$^{-2}$ for an intensity of 1 mJy km s$^{-1}$. For the same sensitivity the $3 \to 2$ 346 GHz line corresponds to a column density of $1.2 \times 10^{16}$ cm$^{-2}$ because $\varpi_3 = 0.006$, and the limits obtained from higher rotational transitions are even worse for very low excitation. However we have assumed the mean value of the large scale motion for these estimates: the limits will go lower for objects with very high peculiar velocity. Also for nearby galaxies (like in the Virgo cluster) scanning with a broader beam ($\sim$ 0.5 square arc minute) can probe column densities a few times $10^{13}$ cm$^{-2}$ in the CO 230.7 GHz line for similar instrument sensitivity.

For reference, we have tabulated the published intrument specifications of some of the future far-IR and sub-mm experiments. Obviously the instrument with the maximum possibility to detect individual objects from scattering should be ALMA, with its excellent angular and spectral resolution, and sensitivity extending below mJy level. The frequency coverage of ALMA will ve particularly suitable for studying the CO rotational lines, as well as the FS lines of neutral carbon. Air- ans space-borne infrared experiments like SOFIA and Herschell might become useful for studying the effect of scattering in atomic and ionic FS lines at higher redshifts.

# Chapter 3

# Scattering & Peculiar Motion of the Galaxies

## 3.1   Scattering signal in presence of emission

The effect of resonant scattering in presence of peculiar velocities in far-IR or sub-millimeter lines is extremely attractive, as it might allow us to infer peculiar motions of nearby galaxies in the CMB rest frame. Using higher rotational transitions of CO molecule, or fine-structure lines of neutral carbon, we can also probe the peculiar motion of galaxies at low or intermediate redshifts ($z \lesssim 5$). In this separate section we investigate this possibility as an application of scattering observation in individual objects.

As shown in the previous section, the formulation for the change in the background CMB temperature due to resonant scattering in molecular or fine-structure lines is extremely simple, it consists of only *two* parameters: the optical depth of the scattering cloud at the line frequency, $\tau_\nu$, and the component of its peculiar motion in the CMB rest frame in the direction of the observer, $\beta_\parallel$ (Dubrovich 1977, Maoli et al. 1994),

$$\frac{\Delta T_b}{T_\gamma} \; = \; - \; \tau_\nu \; \beta_\parallel \tag{3.1}$$

The negative sign comes from the convention of taking $\beta_\parallel$ positive for motion away from the observer, which gives a decrement in $\Delta T_b$. We take the case of CO molecules as our example, since we shall be focusing on the scattering in CO rotational lines in nearby galaxies. The change in the brightness temperature observed from scattering, and the velocity integrated intensity, have the form

$$\Delta T_b^{\mathrm{obs}}(\nu) = T_0 \; \varpi_l N_{\mathrm{CO}} \; \frac{c^2}{8\pi\nu^2} \; \frac{g_u}{g_l} \big(1 - \exp(-x)\big) \; A_{ul} \; \varphi(\nu) \; \beta_\parallel \tag{3.2}$$

$$I^{\mathrm{obs}} = \frac{hc}{4\pi} \; \frac{1}{(1+z)^3} \; \frac{x}{(e^x - 1)} \; \varpi_l N_{\mathrm{CO}} \frac{g_u}{g_l} \; A_{ul} \; \beta_\parallel(z) \tag{3.3}$$

The later have units of mJy km s$^{-1}$ sr$^{-1}$. We shall be using this expression to estimate the column density, and hence optical depth, of the scattering species in a fully resolved gas cloud.

### 3.1.1 Simultaneous observations of scattering and emission

We saw that the amplitude of the scattering signal depends on two parameters: the peculiar motion of the objects towards us, and the optical depth in the line frequency. The optical depth in turns depends upon the column density of the scatterer. Hence if we try to estimate the peculiar motion of galaxies from a decrement of background CMB temperature (which can only be caused by scattering), we must have an accurate idea about the column density of the scatterer. This is where the simultaneous observation of scattering and emission in two different lines become useful. It has never been observed previously because the observation of scattering signal requires very high instrument sensitivity, and also existence of CO molecules in low density regions of galaxies. As we shall see in the next chapter, different rotational levels of CO have different critical densities when scattering becomes observable in that transition. e.g. collisions with hydrogen become more effective for the lowest lying CO rotational level at densities around $2-3$ cm$^{-3}$, whereas for the next transition this density is almost 10 cm$^{-3}$. For galaxies moving with upto 1500 km s$^{-1}$, both density limits become 3- or 4-times higher. So it can very well happen that in one line we have emission, and in other we have scattering, from the same molecular cloud. Simultaneous observations at two different frequencies will give us *independent* estimate on the density and optical depths.

Let us consider the two lowest transitions of CO rotational system: J=0-1 115 GHz, and J=1-2 230 GHz. Let us consider the local universe, with $T_{EX} \approx T_0$ where $T_0 = 2.726$ K. We assume from this low density cloud we have emission due to collision at 115 GHz, but emission is negligible at 230 GHz. If in this neutral cloud the most dominant partner is hydrogen atoms, then the integrated line intensity at 115 GHz for optically thin emission from a homogeneous gas can be written as

$$I_{115 \text{ GHz}} = \frac{hc}{4\pi} \, N_{\text{CO}} \, n_{\text{H}} \, \varpi_0 \, \gamma_{01} \tag{3.4}$$

We can compute the level population at the lowest level, $\varpi_0$, easily under the assumption $T_{EX} \approx T_{CMB}$, and use this column density with eqn.(3.3) to get the line integrated flux at 230 GHz from scattering

$$I_{230 \text{ GHz}} = \left( \frac{x_{12}}{\exp(x_{12}) - 1} \right) \frac{g_2}{g_1} \, \varpi_1 \, \left[ \frac{I_{115 \text{ GHz}}}{n_{\text{H}} \, \varpi_0 \, \gamma_{01}} \right] A_{21} \, \beta_{\parallel} \tag{3.5}$$

where $x_{21} \equiv h\nu_{21}/kT_0$. This immediately gives us, in the approximation $T_{EX} \approx T_0$ such that $\varpi_0 = 0.712$ and $\varpi_1 = 0.281$, an expression for the radial component of velocity in the CMB rest

frame

$$\beta_\parallel = 1.36 \times 10^{-2} \left(\frac{n_H}{10 \text{cm}^{-3}}\right) \left(\frac{I_{230 \text{ GHz}}}{I_{115 \text{ GHz}}}\right) \tag{3.6}$$

where we assumed a 60 K gas cloud in which $\gamma_{01} = 4.75 \times 10^{-10}$ cm$^3$ s$^{-1}$ (Balakrishnan et al. 2002), and we have $A_{21} = 7.36 \times 10^{-7}$ s$^{-1}$ (Chandra et al. 1996).

We still have the uncertainty about the neutral hydrogen density in the gas cloud, for which we can use observation at yet another frequency, like the 21 cm line. We can also use the fine-structure line emission for neutral carbon 492 GHz line, as from Fig.(4.5) we see that collision with neutral hydrogen atoms becomes effective at much lower densities in producing line emission if this FS doublet. So we will have line emission from neutral carbon at 492 GHz similarly as before

$$I_{492 \text{ GHz}} = \frac{hc}{4\pi} \, N_C \, n_H \, \varpi_0^{CI} \, \gamma_{01}^{CI} \tag{3.7}$$

which can be used to get an estimate for $n_H$. Using eqn.(3.6) therefrom we can estimate the peculiar motion of the cloud or galaxy.

We point out that the simple formalism for line emission presented here assumed uniform density gas, without the effect of clumping. In reality for a moderately large beam-width or for an object at larger distance we must emply some filling factor into the computation. For our simple estimate, however, we neglect these complications.

### 3.1.2 Density limit for the effectiveness of scattering

We briefly point out here the densities which can be probed with scattering, a more detailed discussion on this topic can be found in the next chapter. We concentrate on predominantly neutral gas, where the main collision partner for CO molecules will neutral hydrogen atoms or $H_2$ molecules. The brightness temperature from emission can be written as

$$T_b^{em} = T_\gamma \, \frac{c^2}{8\pi\nu^2} \, \frac{(e^x - 1)^2}{xe^x} \, \varpi_l \, N_{CO} \, n_H \, \gamma_{lu} \, \varphi(\nu) \tag{3.8}$$

where $n_H$ density of the neutral hydrogen atoms (in cm$^{-3}$), and $\gamma_{lu}$ is the collision rate (in cm$^{-3}$s$^{-1}$) from lower to upper level. If we compare this with the brightness temperature arising from scattering in the same line, we arrive at the expression of density at which both scattering and emission contribute equally to the brightness temperature

$$n_{H/H_2} = \frac{xe^x}{(e^x - 1)^2} \, \left(1 - \frac{\varpi_u \, g_l}{\varpi_l \, g_u}\right) \, \frac{g_u \, A_{ul}}{g_l \, \gamma_{lu}} \, \beta_\parallel \tag{3.9}$$

Below this *critical density* the gas cloud will not be visible in scattering anymore as the scattering effect will be dwarfed by the emission due to collisions. If we assume the average peculiar motion of galaxies in clusters with respect to the CMB rest frame, which scales roughly as $600(1 + z)^{\frac{1}{2}}$

km s$^{-1}$, such that for local universe the radial component of motion is roughly 350 km s$^{-1}$, then this density corresponds to about $\sim 1$ hydrogen molecule per cm$^3$, or about $\sim 10$ hydrogen atoms per cm$^3$, in neutral gas. In some massve clusters like Virgo, however, the galaxies can attain unusually high peculiar velocities, of the order of $1500 - 2000$ km s$^{-1}$. Then this density limits when scattering becomes effective correspondingly becomes higher, as can be seen from Fig.(3.2) for Virgo cluster galaxy M 99.

Since we have for low densities $(1 - \varpi_u g_l/\varpi_l g_u) \approx (1 - e^{-x})$, we can approximately write the critical density of hydrogen atoms (or molecules) when a gas cloud becomes visible in scattering as

$$n_{\mathrm{H/H_2}} \approx \frac{x}{e^x - 1} \frac{A_{ul}}{\gamma_{lu}} \beta_{\parallel} \tag{3.10}$$

where, as before, $x$ is the shorthand for $x \equiv h\nu/kT_{\mathrm{CMB}}(z) = h\nu_{obs}/kT_0$. Now one can see clearly how higher density objects can be probed by scattering if the peculiar motion is high, from the direct dependence of this critical density on $\beta_{\parallel}$. We are particularly interested in galaxies having a positive radial velocity, i.e. galaxies moving away from us with high velocity, since that will give rise to *decrement* in the background temperature because of scattering. Such negative signal is the unique characteristic of the scattering phenomenon. Strong scattering signal will also be expected from galaxies moving towards us, but since that signal will have the same feature as line emission, it will be impossible to distinguish the scattering case from emission from an increase in background temperature.

## 3.2 Peculiar motion of nearby galaxies

In this section we discuss the expected change in brightness temperature of galaxies for some low CO column density, which we take fixed at $10^{13}$ cm$^{-2}$. However to minimize the effect of collision we shall assume that the neutral gas has no more than $\sim 10$ hydrogen atoms per cm$^3$ in the scattering cloud. Such extremely low-density objects may provide insufficient shielding for the CO molecules from the ionizing UV background, and detection of the scattering signal might prove to be very difficult. However, we note that such column densities for the CO molecules are at the present observational limit in our Galaxy, deduced from the UV spectra obtained by *Copernicus* satellite (Crenny & Federman 2004). It is significantly lower than the column densities obtained from millimeter wavelength studies of emission from molecule-rich gas (e.g. Lambert et al. 1994). Detection of scattering signal from very high velocity galaxies, therefore, may prove to be an important tool for detecting the presence of very low density neutral gas.

We emphasize at this point that in the following discussion we have neglected the rotation velocity of the spiral galaxies. For face-on spirals like the M99 in Virgo cluster this is not a problem, as the scattering signal only depends on the radial component of peculiar motion, but

**Change in Brightness Temperature for Local Group Galaxies**

| Name of Galaxy | $V_r$ (km s$^{-1}$) | Position $(l, b)$ | $V_{corr}$ (km s$^{-1}$) | $V_{pec}^{\mathrm{CMB}}$ (km s$^{-1}$) | $\Delta T_b$ for J=1-0 at 115 GHz | $\Delta T_b$ for J=2-1 at 230 GHz |
|---|---|---|---|---|---|---|
| LMC | 275 | $280.2°, -33.3°$ | +58 | +333 | -30 | -9 |
| SMC | 148 | $302.8°, -44.3°$ | $-34$ | +114 | -10 | -3 |
| M 31 | $-315$ | $121.2°, -21.6°$ | $-290$ | -605 | +55 | +16 |
| M 32 | $-205$ | $121.1°, -21.9°$ | $-291$ | -496 | +45 | +13 |
| M 33 | $-181$ | $133.6°, -31.5°$ | $-287$ | -468 | +43 | +12 |
| M 110 | $-241$ | $120.2°, -21.4°$ | $-291$ | -532 | +48 | +14 |
| IC 1613 | $-232$ | $129.7°, -60.5°$ | $-330$ | -562 | +51 | +15 |
| IC 342 | 31 | $121.0°, -26.7°$ | $-322$ | -301 | +26 | +7 |

Table 3.1: Expected change in the brightness temperatures from scattering in the CO 115.3 GHz and 230.6 GHz rotational lines. The radial velocity is for the center of the galaxy, ignoring rotation. Considering rotation will result in an increase and decrease from these mean values on the two ends of the spiral arms of an inclined galaxy. The correction velocity, $V_{corr}$, takes into account the Sun's motion in the CMB rest frame, and explained in Fig.(3.1). The change in brightness temperature is computed for a CO column density of $N_{\mathrm{CO}} = 10^{13}$ cm$^{-2}$ and line width 50 km s$^{-1}$. The brightness temperatures are in units of $\mu$K $\cdot$ km s$^{-1}$.

for most galaxies the rotation will result in an increase of temperature distortion at one side of the galaxy and a decrease on the other side. For simplicity we have limited our analysis only to the mean center-of-mass motion of the galaxies, and for more accuracy the radial component of the rotational velocity must be added and subtracted on the two opposite sides. It is also worth to remember that the main component of peculiar motion actually comes from the large-scale motion of the galaxies, as can be seen from the fact that the motion of our Galaxy as a whole in the CMB rest frame is larger than the rotational velocity of the Sun around the center.

### 3.2.1 Brightness temperature of Local Group galaxies

We now focus attention to our neighboring galaxies, and try to predict the expected increment or decrement in the brightness temperature due to scattering in the CO lines. The obvious reason for studying these nearby objects is that one can resolve small low-density regions inside this galaxies with single-dish telescopes, and of course the absence of any Hubble motion or baricentric velocities in the observed $V_r$ reduces the uncertainty in estimating peculiar motion. However, most of our local group members, apart from LMC and SMC, are moving towards us, which will give a increment in brightness temperature from scattering. Such increment will be impossible to distinguish from the emission signal coming from the same lines. Also relatively weak peculiar motions of these galaxies forbid studying of most of the density ranges via scattering.

We see that for local group of galaxies, none of them have strong outward motion, and therefore we should get only increment in the background temperature. Only our two neighboring galaxies

LMC and SMC move away from us, and might give us a *decrement* in the CMB temperature. Since temperature decrement is the most definitive sign for scattering signal, we consider galaxies outside our local group, in Virgo cluster, where the high mass of the cluster gives rise to very strong peculiar motions.

### 3.2.2 Correction due to Sun's proper motion in the CMB frame
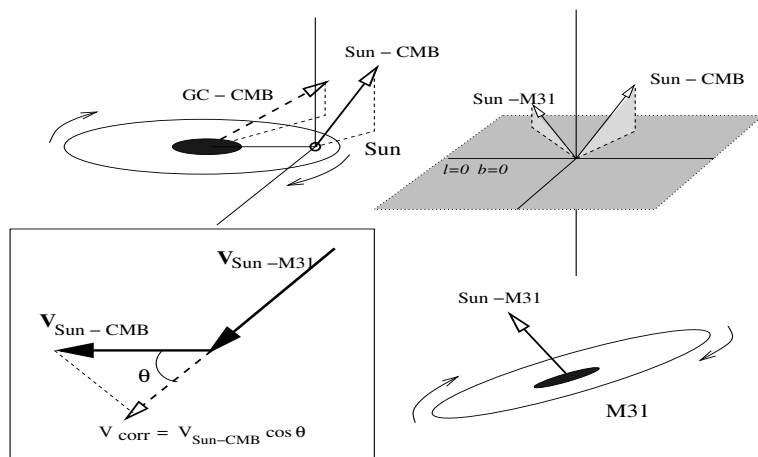


Figure 3.1: Schematic diagram for vector addition, trying to illustrate the approach used for the correction of our own proper motion in the CMB rest frame. The galaxy in the example is chosen to be M 31 (Andromeda), and for the time being we neglect its rotation and focus on its center-of-mass motion. Center of M 31 is situated at the galactic coordinates $(l, b) = (121.2°, -21.6°)$, and has *heliocentric* radial velocity of 315 km s$^{-1}$ towards us. Our own heliocentric motion is 370 km s$^{-1}$ in the direction $(l, b) = (264.4°, 48.4°)$, thus making an angle of $\Theta = 156°$ between the vectors *Sun-M31* and *Sun-CMB*. The correction velocity due to Sun's proper motion in the CMB rest frame is therefore $V_{\text{Sun-CMB}} \cos(\pi - \Theta)$, directed in the opposite direction on M 31 for velocity addition.

For estimating the change in brightness temperature at the resonant frequency due to peculiar motion of the galaxies, we must take into consideration our own motion with respect to the CMB. This heliocentric velocity in the CMB rest-frame has been accurately measured from the cosmic dipole by COBE DMR instrument, and we know the Sun is moving with a velocity 369.5 km s$^{-1}$ towards the direction $(l, b) = (264.4°, 48.4°)$ in the CMB rest-frame (Kogut et al. 1993). We correct for this motion by adding a correction velocity, $V_{corr}$, to the observed radial motion of the galaxy

$$V_{corr} = -\vec{n} \cdot \vec{V}_{Sun-CMB} \tag{3.11}$$

where the unit vector $\vec{n}$ points towards the galaxy, or a section of the galaxy, under study. In this way, we pick up the component of the Sun-CMB motion in the direction *opposite* to the direction of the galaxy, $V_{corr} = -(V_{Sun-CMB} \cos\theta)$ where $\theta$ is the angle between our direction of motion

with respect to the CMB and the galaxy's motion towards us (Fig.3.1). This $V_{corr}$ can then be added to the radial motion of the galaxy to get its absolute peculiar motion (more accurately, the component of absolute motion in our direction) in the CMB rest-frame. The result for such velocity estimation and prediction of temperature change due to scattering is listed in Table(3.1) and (3.2).

It is worthwhile to remember that the effect of scattering is sensitive only to the proper motion of the galaxy in the CMB rest frame. Hence for galaxies beyond the local group we must correct for the Hubble expansion either by assuming some definite Hubble constant and distance to the object, or by taking a fixed baricentric velocity of the galaxy cluster and aubtracting it from the observed radial motion. We employ he later technique for analysis of Virgo cluster.

### 3.2.3 Peculiar motion of galaxies in the Virgo cluster

Next we consider some galaxies from nearby Virgo galaxy cluster, both because of its proximity and because the high mass of Virgo gives rise to unusually high peculiar velocity of some of the galaxies. There are many well-defined spirals in the central region of Virgo whose large angular dimensions may allow us, with future facilities like ALMA, to study small outer sections of the galaxies with very low density. For a distance of almost 20 Mpc, the value of Hubble expansion at Virgo is approximately 1300 km s$^{-1}$, and we must subtract this value from the observed radial motion of the galaxies in the cluster. We show below that because of the very high peculiar velocities inside the Virgo cluster, temperature decrement as low as $-100\mu$K can be observed in galaxies like M88 and M99.

To derive the peculiar motion of the member galaxies in Virgo, we proceed as following. The observed radial motion of the galaxies has *three* components:

$$V_r = V_h + \vec{V}_{pec} \cdot \hat{n} + \vec{V}_{gal} \cdot \hat{n} \tag{3.12}$$

where $V_h$ is the Hubble expansion velocity at the center of the Virgo cluster, $V_{pec}$ is the peculiar motion of the cluster as a whole in the CMB rest frame (motion in the Great Attractor potential), and $V_{gal}$ is the Virgocentric peculiar motion of the galaxy itself. $\hat{n}$ is the unit vector in our direction to pick the appropriate radial component. The effect of scattering under discussion does not depend on the Hubble expansion velocity, as the scattering of CMB photons by atoms and molecules depends only on their velocity in the CMB rest frame. We can subtract the $V_h$ term by assuming some definite Hubble constant (e.g. $H_0 = 71$ km s$^{-1}$Mpc$^{-1}$from WMAP data, Spergel et al. 2003) and multiplying it by the distance of Virgo cluster ($\sim 18$ Mpc, from observations of Cepheids, Freedman et al. 1994). Alternatively, we can subtract a fixed *cluster velocity* from the observed radial motion of the galaxy, and take the remainder as the galaxy's peculiar motion in the CMB rest frame. This cluster velocity already has the Hubble expansion term inside it

$$V_{cl} = V_h + V_{pec} \equiv 1200 \;\; \text{km s}^{-1} \tag{3.13}$$

**Peculiar Motion and Change in Brighness Temperature for**
**Virgo Cluster Galaxies in CO Lines**

| Name of Galaxy | $V_r$ (km s$^{-1}$) | $V_{pec}$ (km s$^{-1}$) | Position $(l, b)$ | $V_{corr}$ (km s$^{-1}$) | $\Delta T_b$ for J=2-1 ($\mu$K $\cdot$ km s$^{-1}$) |
|---|---|---|---|---|---|
| NGC 4406 (M 86) | -227 | -1487 | $279.1°, 77.6°$ | +263.1 | +32.8 |
| NGC 4569 (M 90) | -235 | -1495 | $288.5°, 75.6°$ | +330.5 | +31.2 |
| NGC 4419 | -261 | -1521 | $276.5°, 76.6°$ | +330.4 | +31.9 |
| | | | | | |
| IC 3453 | +2559 | +1299 | $281.4°, 76.9°$ | +328.9 | -43.6 |
| NGC 4388 | +2524 | +1264 | $279.1°, 74.3°$ | +336.2 | -42.9 |
| NGC 4254 (M 99) | +2407 | +1147 | $270.4°, 75.2°$ | +334.6 | -39.7 |
| NGC 4607 | +2257 | +997 | $293.5°, 74.6°$ | +331.0 | -35.6 |

Table 3.2: Galaxies in the Virgo cluster, and the predicted change in brightness temperature from scattering in the CO 230 GHz line. We take CO column density to be equal to $10^{13}$ cm$^{-2}$, and broadening of the line as 50 km s$^{-1}$. High-velocity galaxies in the direction both towards us and away from us are chosen to demonstrate the effect of increment or decrement of brightness temperature due to scattering. $V_r$ is the observed radial motion (heliocentric velocity) of the galaxy. The correction velocity $V_{corr}$ is explained through Fig.(3.1). For estimating the peculiar velocity (radial component), we have subtracted from the observed radial motion the baricentric velocity of the Virgo cluster, which we assumed to be 1200 km s$^{-1}$.

This value of baricentric velocity of Virgo cluster comes from observations of Federspiel, Tammann & Sandage (1998), and we use this fixed value to obtain the peculiar motion of the galaxy: $V_g^{\text{CMB}} = V_r - V_{cl}$. This of course leaves the room for uncertainty from the peculiar motion of the cluster *itself* in the CMB frame, and the actual result can increase or decrease due to this uncertainty. Finally, we correct for our own peculiar motion in the CMB rest frame by the method described previously, and the result for such computations and corresponding increment or decrement in brightness temperatures are tabulated in Table(3.2).

In the table we have only shown the scattering brightness for the second rotational line, as this transition allows us to probe higher densities in scattering. The main distinguishing feature is the *sign* of change in brightness temperature, which is clearly demonstrated. If we assume some low density gas, with molecular hydrogen density $\sim 10$ cm$^{-3}$, then we shall have emission from the $J = 0 - 1$ 115 GHz line, and simultaneous measurement of scattering and emission will allow us to obtain independent measure of the column density of CO molecules. For an assumed column density of $10^{13}$ cm$^{-2}$ and molecular density of $\sim 10$ cm$^{-3}$, the brightness temperature in emission in the first rotational line is 35 $\mu$K, which is of course always positive in sign.

EXAMPLE: M99 (NGC 4254)

## 3. SCATTERING & PECULIAR MOTION OF THE GALAXIES

M99 (NGC 4254) is a face-on spiral galaxy in the central region of the Virgo cluster, which has a strong positive heliocentric velocity: it is moving away from us at 2407 km s$^{-1}$. This is a bright galaxy (a member of the Messier catalog) having diameter of about 5 arc minutes. This galaxy is a very good candidate for observing a decrease in the background CMB temperature due to scattering in the CO lines, which is a definite signature of the scattering effect. Hence we study this galaxy as a typical example. Such high value of peculiar motion also sets the critical density higher, upto which scattering signal dominates. This enhances the possibility of observing the scattering signal in diffuse neutral gas. From eqn.(3.10) we know that the critical density below which scattering becomes more effective varies linearly with the peculiar velocity, and the result for both collisions with H$_2$ molecule and neutral hydrogen atoms is shown in Fig.(3.2) for M99. We remark that such low values of density in the neutral gas lies at the limit the of present day observation, made from observation of CO absorption lines in the UV bands against continuum of a background star. The lowest column densities of CO reported to date is from the archived *Copernicus* data (Crenny & Federman 2004), which is of the order of $10^{12} - 10^{13}$ cm$^{-2}$, and requires a neutral hydrogen density $10 - 200$ cm$^{-3}$. Under such low density environments CO may only reach a fraction of its equilibrium abundance, which can make promising the study of rotational lines of some transitional ions like CH$^+$.
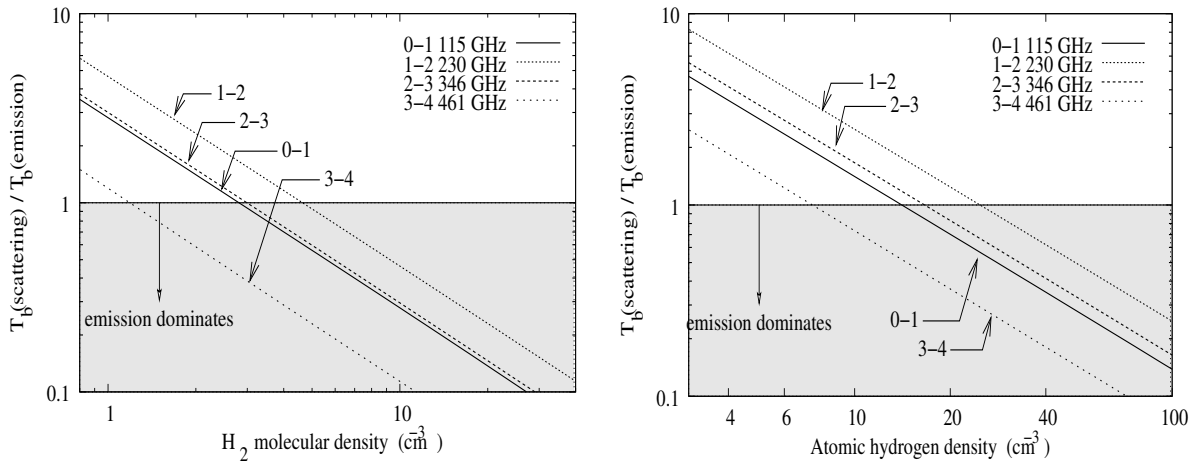


Figure 3.2: Critical density for effectiveness of emission from collision in case of the Virgo cluster galaxy M 99, which has a peculiar velocity of +1147 km s$^{-1}$. The figures show the change in the ratio of brightness temperature in scattering and emission from a gas cloud in CO lines as function of densities. In *left* we show the effect of collision with H$_2$ molecules, and in the *right* the effect of collision with hydrogen atoms. The shaded region marks the domain when the object can not be seen anymore from scattering, as it gets dwarfed by line emission. The labels marked $J - J'$ are the four lowermost rotational transitions of CO.

We briefly describe the formalism we have used to obtain the predicted decrement in brightness temperature for the M99 galaxy. The radial velocity for M99 is 2407 km s$^{-1}$, moving *away* from us.

As descibed above, we subtract from this velocity the baricentric velocity of Virgo cluster, 1200 km s$^{-1}$, to obtain a velocity 1207 km s$^{-1}$as the peculiar motion of the galaxy in *our frame*. The center of M99 is located, in galactic coordinates, at $(l, b) = (270.4°, 75.2°)$, which gives the component of $V_{Sun-CMB}$ in the *opposite* direction of the galaxy as 334.6 km s$^{-1}$. This velocity is added to the observed peculiar motion of M99 to obtain its peculiar velocity in the CMB rest frame in our direction, which we plug into eqn.(3.2). We use a gaussian line profile with broadening 50 km s$^{-1}$, and CO column density of $10^{13}$ cm$-2$ inside our beam. Under very low density the excitation temperature is practically equal to the background CMB temperature, 2.726 K. The predicted temperature decrement for M99 is tabulated in Table(3.2), along with other high-velocity galaxies in the Virgo cluster.

We conclude this section by emphasizing the importance of having an independent estimator for peculiar velecities of galaxies in fields and especially inside clusters, by the method of scattering described in this chapter, if CO or other suitable molecules are found in sufficiently low density medium. The Virgo cluster is often taken as the *zero-point* for determination of the Hubble constant (Tammann & Sandage 1985, Pierce & Tully 1988, Lu et al. 1994), and measuring the distance of Virgo from Cepheids and thereby estimating its redshift was one of the Hubble Telescope key projects (Freedman et al. 1994). Estimating the infall velocity of the Local Group towards Virgo is further important as it provides a very local test for the density parameter $\Omega_0$ (Sandage et al. 1972, Silk 1974 etc.). Furthermore there are evidences that Virgo itself is moving towards the Great Wall (Hoffman et al. 1995). There have been various direct estimates to measure the Virgo cluster velocity using many different techniques, using Cepheids, the 21cm HI line, or Tully–Fischer relationship (see Davis & Peebles 1983 for a review). A detailed modeling of the velocity distribution of the nearby clusters and also the motion of the Local Group in the potential of the Great Attractor has been attempted by many groups, which in turn depends on the estimate of the radial motion of the clusters in the Local Group rest frame (Jerjen & Tammann 1993, Lu, Salpeter & Hoffman 1994, Giovanelli et al. 1998 etc.). The method we are proposing can prove to be extremely important in such analyses, as it provides an independent method of estimating the radial motions directly in the CMB rest frame. However it will be very difficult to pick up the signal of scattering from galaxies, firsly because of its very low amplitude, but more importantly because of such low density gas must be very rare and not been studied yet in nearby and Virgo cluster galaxies. Only for a very few objects with strong *positive* radial velocty, it might become possible with the next-generation of smaller but very sensitive sub-mm instruments, to detect a temperature decrement in the CO $2 - 1$ 230 GHz line, for example, from moderately low density neutral gas. Small one-dish but very sensitive intruments, using new sophisticated detectors now designed for ALMA, APEX, ACT and other similar experiments, will be suitable for searching for absorption in CO lines due to peculiar velocity. For nearby Virgo cluster galaxies with dimensions

of several arc minutes, the sub-arc minute resolution provided by such single dish will be sufficient for scanning the outer regions of the galaxies for any possible decrement in CMB temperature coinciding with the CO $2 - 1$ transition, which will show the existence of resonant scattering.

# Chapter 4

# The Three Critical Densities

## 4.1   Effect of collision in dense regions

In this section we shall be analyzing how the scattering signal compares with the emission in the same lines under different physical conditions. This section is somewhat pedagogic in nature, but an understanding of these different density limits is necessary in order to compare scattering and emission signals from an object. For example for CO, the scattering signal that we are trying to estimate can only be of relevance in very low density neutral gas, because at higher densities collisional excitation of higher levels will be significant, and line emission will start to dominate. At very high densities, collisional excitation and de-excitation will completely determine the level populations, but such high densities ($N > 100 - 1000$ cm$^{-3}$) are only expected in the giant molecular clouds. Hence between these two extremes there are domains when both scattering and emission take place, and it is our purpose to analyze their relative importance.

This combined effect of resonant scattering in presence peculiar velocities in sub-mm lines of molecules like CO, where CMB contains lots of photons for scattering, is very attractive. We tried to explore this possibility, however found that the densities at which the effect becomes observable is extremely low, and may be almost non-existent in the neutral gas regions of Milky-Way and nearby galaxies. In addition we found that there is practically no chance to observe individual objects in the various fine-structure lines of other atoms and ions that are relevant for CMB observations. We have seen that the effect of scattering is proportional to $\beta_\parallel \tau_\nu$, where $\beta_\parallel = v_\parallel/c$ is the radial component of peculiar motion and $\tau_\nu$ is the line optical depth, multiplied to the temperature of background CMB radiation, $T_0$. In this chapter we shall compare the influence of collision with neutral or molecular hydrogen, and also electrons, and discuss *three* types of critical densities: i) the density below which scattering dominates the brightness of the object, ii) the density range where both scattering and emission co-exist, but emission is stronger than scattering. Above this second critical density collisions change the population of the levels significantly. And iii), the third critical density is well-known and discussed in text-books, where collisional de-excitation

dominates over radiative de-excitation, and the excitation temperature of the levels approaches the kinetic temperature of the surrounding gas. Observation of effect from scattering and peculiar motions in individual objects is possible only for densities lower than the first critical density. Such low density objects might be very difficult to find.

However, we remember that resonant scattering in the lines of molecules and atoms is also responsible for changing the *angular distribution* of the CMB in the direction of the gas cloud. It tends to decrease the deviations of the brightness of the background sky from the mean brightness, which is termed as blurring or suppression of primordial anisotropies, and also causes a redistribution of the scattered intensity due to its peculiar motion. This effect is essentially similar to the one discussed for cold electrons in clusters by Zel'dovich & Sunyaev (1980), and has been described by Maoli et al. (1993) for primordial molecules and by Basu et al. (2004) for atoms and ions. For individual objects this effect is very small because $\beta_{\parallel}$ is very low, and also the optical depth in low density regions is also very low. But as it has been shown in Basu et al (2004), contribution of emission in the lines from small individual objects are much less important than the coherent smoothening of CMB fluctuations at small scales from all the objects in the sky, which allows us to pick up the *integrated* signal of scattering by measuring the change in CMB fluctuations. Hence the conclusions of the present work is as following: the effect proposed by Dubrovich and others is difficult to observe in individual objects, but might be possible to observe through blurring of CMB anisotropies at low multipoles ($l \sim 10 - 200$) measured with broad-band CMB telescopes. This is possible because the later method permits us to observe all the objects below the second critical density, where scattering as a process is significant. This opens the way to observe primordial molecules and early chemical enrichment of the universe.

### 4.1.1 Analytic solution for two-level systems

First we shall present some simple analytic solutions for two-level fine-structure systems to get an understanding of the influence of collisions in changing level populations. The formulation presented here is standard, and can be found in many textbooks (e.g. Osterbrock 1988 or Genzel 1991). We present the definition of excitation temperature for a given transition, which we shall be using to demonstrate the effect of collision at different densities. We are, of course, interested in the very low density limits when the excitation temperature is practically equal to the background radiation temperature of CMB photons.

Collisions with electrons (or hydrogen atoms in the case of neutral gas) cause emission from the same atomic and ionic fine-structure lines and hence change the observed $\delta C_l$-s by producing an additional and independent signal on the top of the scattering signal, we compute the deviation of the equilibrium excitation temperature of a two-level system from the background cosmic microwave radiation temperature as a function of the overdensity of the enriched region. The result

of collisions will be to cause a change in the population of atoms and ions in their ground state, and we estimate the required overdensity for causing a given amount (30% or 50%) of change.

We consider a two-level system (like CII or NIII ion) for simplicity, whose population ratio between the two levels is determined by the *excitation temperature*, $T_{EX}$, defined as

$$(\varpi_u/\varpi_l) = (g_u/g_l) \exp\left[-h\nu/kT_{EX}\right] \tag{4.1}$$

where $\varpi_u$ and $\varpi_l$ are the relative fraction of atoms/ions in *upper* or *lower* levels, respectively, and $g_u$ and $g_l$ are the statistical weights of each level. The equilibrium population ratio is obtained by solving the statistical balance equation:

$$\varpi_u \left(A_{ul} + B_{ul}J_\nu + n_e\gamma\right) = \varpi_l \left(\frac{g_u}{g_l}B_{ul}J_\nu + \frac{g_u}{g_l}n_e\gamma_{ul}e^{-h\nu/kT_K}\right) \tag{4.2}$$

Here $A_{ul}$ and $B_{ul}$ are the Einstein coefficients for spontaneous and stimulated emission, and $J_\nu$ is the source function, which in our case is the background radiation field of CMB photons, $J_\nu \equiv (2h\nu^3/c^2)[\exp(h\nu/kT_{CMB}) - 1]^{-1}$. $T_{CMB}$ is the radiation temperature at redshift $z$, defined by $T_{CMB} \equiv T_0(1 + z)$, with $T_0 = 2.726$ K. $n_e$ is the electron density inside the object at redshift $z$, connected to its overdensity $\delta$ by the following: $n_e(z) \equiv \bar{n}_e(z)\,(1 + \delta)$, where $\bar{n}_e(z) = 2.18 \times 10^{-7}(1 + z)^3$ cm$^{-3}$. $\gamma_{ul}$ is once again the collisional de-excitation rate (in cm$^3$ s$^{-1}$), and $T_K$ is the kinetic temperature of the electrons, which we assume to be roughly constant at $10^4$ K. Then from eqn.(4.1) we can express the overdensity as a function of excitation temperature:

$$1 + \delta = \frac{A_{ul}\left[(1 + \Gamma)e^{-h\nu/kT_{EX}} - \Gamma\right]}{\bar{n}_e(z)\,\gamma_{ul}\left[e^{-h\nu/kT_K} - e^{-h\nu/kT_{EX}}\right]} \tag{4.3}$$

where $\Gamma \equiv [\exp(h\nu/kT_{CMB}(z)) - 1]^{-1}$, and we have used $B_{ul} = (c^2/2h\nu^3)A_{ul}$. Eqn.(4.3) is exact, which can be further simplified in the Wien limit (which is of interest to us in the redshift range $z \in [5, 30]$) and using the fact that $T_{CMB}(z) \ll T_K$,

$$1 + \delta = \frac{A_{ul}\left[e^{-h\nu/kT_{EX}} - e^{-h\nu/kT_{CMB}(z)}\right]}{\bar{n}_e(z)\,\gamma_{ul}\left[1 - \frac{h\nu}{kT_K} - e^{-h\nu/kT_{EX}}\right]} \tag{4.4}$$

Now we express the excitation temperature in terms of a given amount of deviation of the ground state population of the atom/ion, from the ground state population solely determined by the CMB temperature. This ratio can be written as

$$\frac{\varpi_{low}(T_{EX})}{\varpi_{low}(T_{CMB})} = \frac{1 + \frac{g_u}{g_l}\exp(-h\nu/kT_{CMB}(z))}{1 + \frac{g_u}{g_l}\exp(-h\nu/kT_{EX})} \tag{4.5}$$

This ratio should always be less that unity, i.e. $T_{EX} \geqslant T_{CMB}$, as collisions will tend to excite atoms or ions from their ground state. However, a very large over-density is needed in order to produce any significant amount of deviation from the CMB equilibrium, as can be seen from
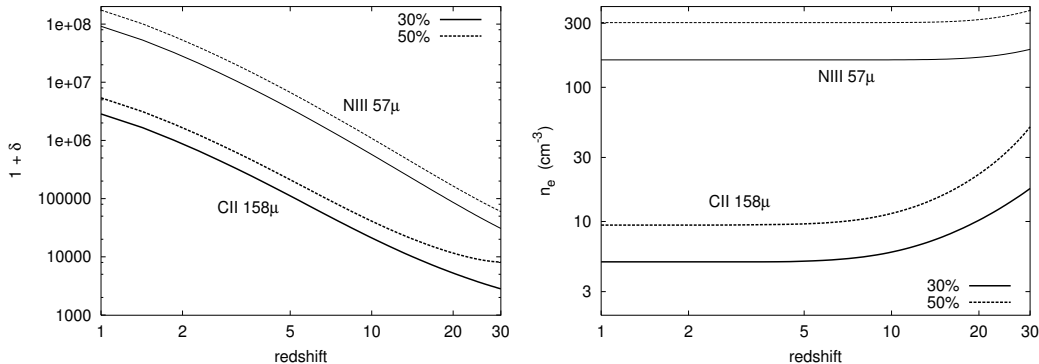
Figure 4.1: Overdensity and actual electron number density required to cause significant deviation of the excitation temperature from the background cosmic microwave temperature, as function of redshift. Shown here are the cases for CII and NIII fine-structure singlets. The thick lines are for CII ion,and the thin ones are for NIII ions. The pair of solid and dashed lines correspond to 30% and 50% decrease in the optical depth for the same column density, respectively.

Fig.(4.1) for the case of CII $158\mu$ and NIII $57\mu$ transitions. These two transitions are picked as they both arise from two-level fine-structure splitting, but results are similar for all other relevant atoms and ions. Such high densities are expected in the dense clouds where intense star formation is taking place; however, in a sufficiently large volume the ratio $\langle n_e n_{X_i}\rangle/\langle n_e\rangle\langle n_{X_i}\rangle$ (where $n_{X_i}$ is the ion density) will be small enough to guarantee the effectiveness of the scattering process.

### 4.1.2 Change in level population in multilevel systems

Now we proceed to solve the statistical equilibrium equations for a multilevel system. Our main purpose is to solve for the level populations of the CO rotational system, but we have also used the same method for solving fine-structure doublets like OI and NII. The method to determine and solve the detailed balance euations is described in Appendix B. In what follows, we take CO as our standard example.

The detailed statistical balance equation for an arbitrary number of levels, including the effect of induced upward and downward transitions in presence of CMB photons, can be written as

$$n_i \sum_k \left(R_{ik} + C_{ik}\right) = \sum_k n_k \left(R_{ki} + C_{ki}\right) \tag{4.6}$$

with

$$R_{ik} = A_{ik} + J_\nu B_{ik} \quad \text{and} \quad C_{ik} = n_{\text{H}_2}\gamma_{ik}$$

Here $R_{ik}$-s are the radiative transition probabilities including the induced transition effects, and $C_{ik}$-s are the collisional transition probabilities which relate to the hydrogen molecule number
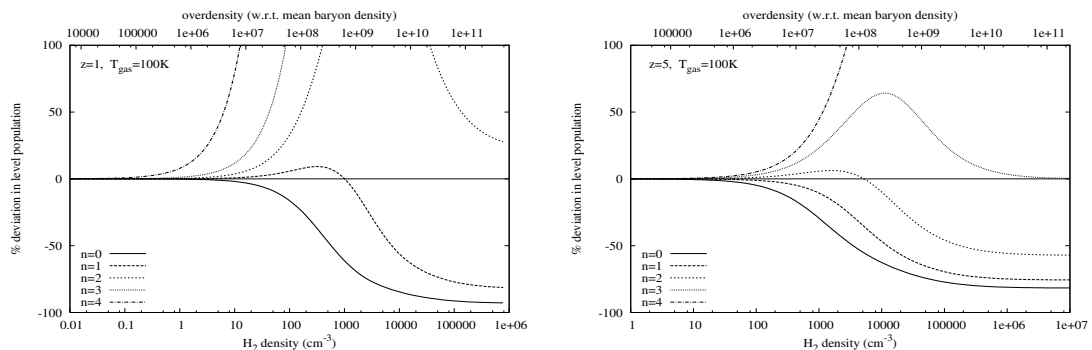
Figure 4.2: Percentatge deviation in the population of CO rotational levels, at a particular redshift: $z = 1$, (*left*) and $z = 5$, (*right*). This plot shows how population of individual levels change due to collisions at different densities of molecular gas. The percentage of molecules at the lowest level can only decrease, as the increasing amount of collisions will tend to populate the upper levels. For $J = 1$ and higher levels, the population first increase as that from the lower levels are reduced, but they also start to decrease as even higher levels get occupied.

density (or neutral hydrogen number density, depending on which species is predominant) as $C_{ik} = n_{H_2} \gamma_{ik}$. For CO molecule, we have considered collisional rates for upto 15 levels, which gives sufficient accuracy at the redshifts and densities of interest, excluding only very overdense regions ($\delta > 10^{10}$) at redshifts $z > 10$. The data concerning the A-coefficients for these transitions are taken from Chandra et al.(1996), and the collisional rates of CO with $H_2$ molecules are taken from Flower & Launay (1985). Data for neutral hydrogen collision with CO are from Green & Thaddeus (1976).

The result for such computations is shown in Fig.(4.2). Here we show how population of individual rotational levels of CO changes as function of hydrogen molecular density at a particular redshift, assuming a hot molecular gas of temperature 100K. We see that because of the downward transitions from higher levels due to collisions, the percentage population of some lower levels actually *increase* in certain density range, before dropping down again. The most interesting fact that even upto $H_2$ densities of several hundred molecules per cm$^3$, which corresponds to an overdensity of roughly $10^7$ at $z = 5$, the change in level population is negligible from pure thermal equilibrium. This is shown in Fig.(4.3). Here we plot the required molecular gas densities at various redshifts to cause a 30% change in the level populations. Scattering will be dominant over line emission unless densities cross such critical values. In fact we can consider *three* types of critical densities: standard critical density is where $T_{EX}$ becomes equal to $T_{gas}$, i.e. when collisional de-excitation probability from the upper level dominates over radiative rates. In this chapter we are introducing two additional critical densities. First type corresponds to the density when brightness temperature of an uniformly dense object is contributed mostly from emission, and we shall discuss this in the next subsection. The second is one when we begin to change level

35
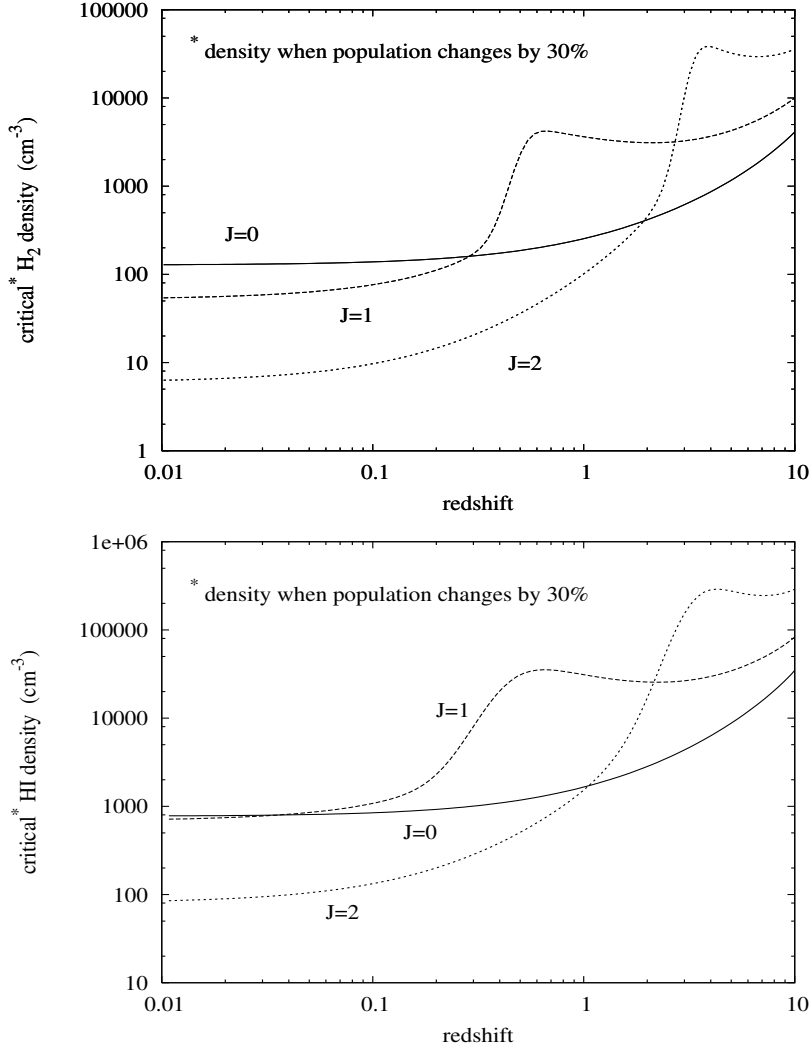
Figure 4.3: The evolution of the critical density for CO rotational levels with redshift. This plot shows the density limits which causes 30% deviation in any given level population, as a result of collisions with $H_2$ molecules *(top)* or neutral hydrogen atoms *(bottom)*. This is the density when collisions start to affect level populations significantly, and scattering as a process becomes insignificant. We have termed this density as our *second* critical density, whereas the first critical density is at which an individual object becomes no longer visible in scattering. We note that the density limits shown in this figure does not depend on the velocity of peculiar motion of the object, and is determined only from atomic or molecular properties.

populations significantly, as shown in Fig.(4.3). The third type is the well-know classical definition of critical density for local thermodynamic equilibrium condition.

In principle any source other than the CMB (e.g. stellar disks) radiating in the sub-mm wavelengths can influence the level populations of CO rotational lines. But their effect will be significant only at the very dense core of the gas clouds, very near to the source of the radiation, and over large distances CMB will be dominant by far. This can be easily verified if we consiter the influence of a single stellar disk, which at wavelengths around $1000\mu$ has luminosity roughly $10^{-2}$ L$_\odot$ (Chiang & Goldreich 1997). This means CMB photons at this frequency will be dominant at a distance of roughly 4700 A.U., or only 0.02 pc. Hence for molecular clouds of size several pc, especially at outer low density regions, one needs to consider only the effect of CMB for calculating level populations.

## 4.2 Scattering brightness vs. emission brightness

Finally we consider the condition when the brightness temperature of an individual objects gets dwarfed by the emission in lines. This density limit is crucial as it determines whether we can expect to observe the scattering signal from pointed observations of low density gas inside a galaxy. We shall see this density depends directly on the peculiar motion of the gas cloud, and consequently one can probe higher densities through scattering in a high velocity galaxy inside massive clusters, as we saw in out discussion on Virgo cluster galaxies in Chapter 2.

In order to compare the brightness temperature of a source in both emission and scattering, we consider the simplistic situation of uniform over-density inside any given volume, neglecting the effect of gas clumping and filling factors. We recall that the volume emissivity is given by

$$j_\nu^{\rm em} = \frac{h\nu}{4\pi}\ n_{\rm H_2} n_{\rm CO}\ \varpi_l\ \gamma_{lu}\ \varphi(\nu) \tag{4.7}$$

where $n$-s denote the number densities in cm$^{-3}$, and $\gamma_{lu}$ is the collision rate (in cm$^{-3}$s$^{-1}$) from lower to upper level. This is valid when density is not too high, i.e. when $n < n_{crit}$, where $n_{crit} \equiv A_{ul}/\gamma_{ul}$ is the standard critical density (e.g. Osterbrock 1988). This emissivity gives rise to the observed line flux according to $\Delta I_\nu = \int j_\nu (1+z)^{-3} dl$, and using the relation $\Delta T_b/T_0 = [(e^x-1)/xe^x]\ \Delta I_\nu/B_\nu$ with $T_0$ as present-day CMB temperature, we get

$$T_b^{\rm em} = T_0\ \frac{c^2}{8\pi\nu^2}\ \frac{(e^x-1)^2}{xe^x}\ \varpi_l N_{\rm CO} n_{\rm H_2} \gamma_{lu}\ \varphi(\nu) \tag{4.8}$$

We compare this with the brightness temperature from scattering given in eqn.(3.2), and arrive at the follwing ratio

$$\frac{T_b^{\rm sc}}{T_b^{\rm em}} = \frac{xe^x}{(e^x-1)^2}\ \left(1 - \frac{\varpi_u}{\varpi_l}\frac{g_l}{g_u}\right)\ \frac{g_u}{g_l}\frac{A_{ul}}{\gamma_{lu}}\ n_{\rm H_2}^{-1}\ \beta_\parallel \tag{4.9}$$

The result for this ratio is shown in Fig.(4.4), for collision with H$_2$ molecule, as well as for collision with neutral hydrogen. This is our *first* type of critical density, when brightness temperature
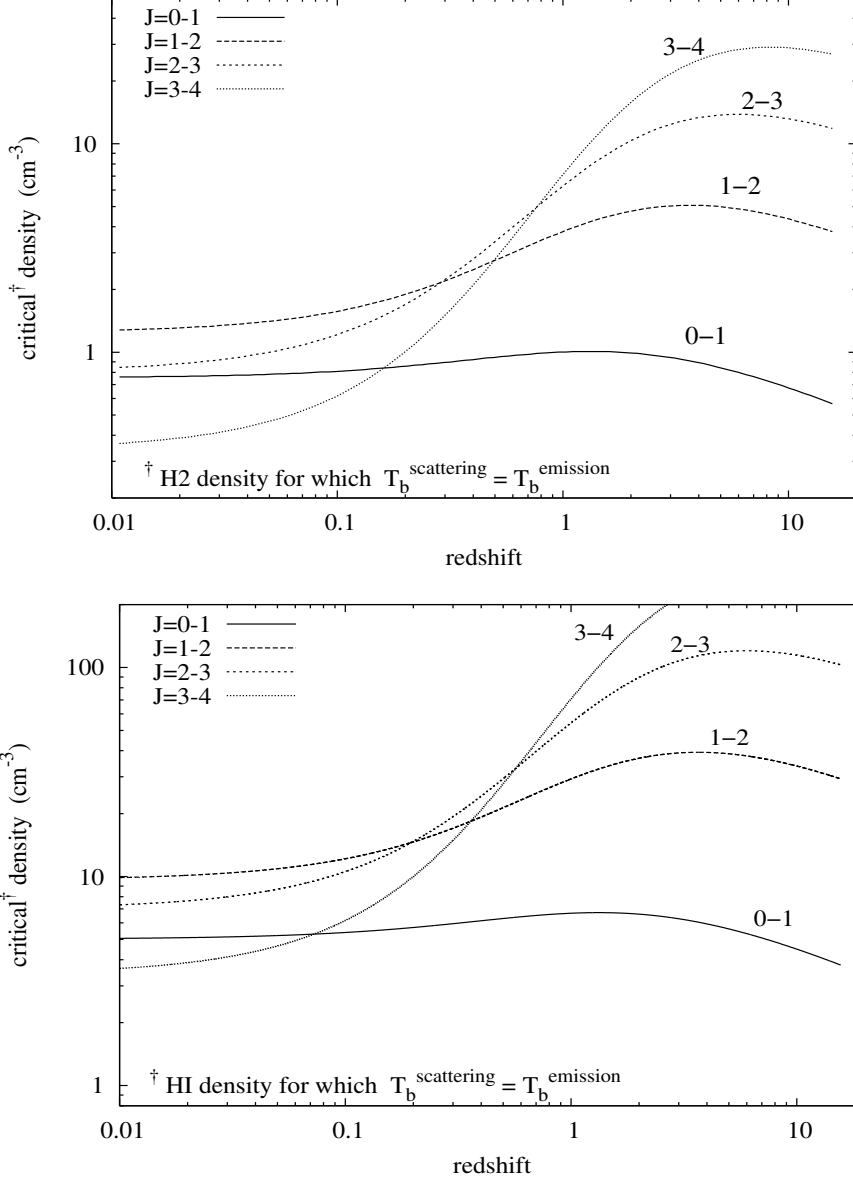
Figure 4.4: The *first* type of critical density, when the brightness temperature in emission becomes equal to that in scattering. The results are for CO rotational levels, in collision with $H_2$ molecules (**top**), and with neutral hydrogen atoms (**bottom**). This figure assumes the mean peculiar velocity of large-scale motion, which scales with redshift as $\beta_\parallel(z) \approx 2 \times 10^{-3}/\sqrt{1+z}$, and is further divided by $\sqrt{3}$ to get radial component in any direction. For individual objects with high peculiar velocities (like galaxies in the Virgo cluster) this density limit goes correspondingly higher.

in emission of an uniformly overdense object will start dominating over the brightness temperature in scattering. Of course this ratio neglect any effect of clumping, and hence this is strictly the lowest critical density limit when one can resolve the gas cloud into small homogeneous clumps. The effect of non-zero clumping in a large volume will raise this ratio, provided that CO is present in sufficient amount in the under-dense parts.

Some physical understanding of the ratio in eqn.(4.9) can be obtained if we express it alternatively in terms of critical density, stated above as $n_{crit} \equiv A_{ul}/\gamma_{ul}$, with the transformation relation of collision rates: $\gamma_{lu} = \gamma_{ul}(g_u/g_l)\exp(-h\nu/kT_{gas})$. Then this ratio can be written approximately as

$$\frac{T_b^{\mathrm{sc}}}{T_b^{\mathrm{em}}} \approx \frac{xe^x}{(e^x-1)^2} \left(1 - \frac{\varpi_u}{\varpi_l}\frac{g_l}{g_u}\right) \frac{n_{crit}}{n_{\mathrm{H_2}}} \beta_\parallel \tag{4.10}$$

assuming the kinetic temperature of the gas to be much larger ($T_{gas} \sim 50 - 100$ K) than the rotational temperature of the CO levels. The standard critical densities at such gas temperatures are $n_{crit} \sim 2000$ cm$^{-3}$ for the J=0-1 transition, and $n_{crit} \sim 10^4$ cm$^{-3}$ for the J=1-2 transition. Recalling that $\beta_\parallel \sim 10^{-3}$, we immediately see that the brightness temperature in emission will be equal to that in scattering in the first rotational level when density of the object is $\sim 1$ cm$^{-3}$, and for the second rotational level when density is a few times more. We also note that for low densities $(1 - \varpi_u g_l/\varpi_l g_u) \approx (1 - e^{-x})$, therefore this ratio can be further simplified as

$$\frac{T_b^{\mathrm{sc}}}{T_b^{\mathrm{em}}} \approx \frac{x}{e^x-1} \frac{A_{ul}}{\gamma_{ul}} n_{\mathrm{H_2}}^{-1} \beta_\parallel \tag{4.11}$$

We note that the factor $(e^x-1)^{-1}$ is the photon occupation number for the CMB, which decreases exponentially below $z \lesssim 1$ for the far-IR fine-structure lines. This explains why only the two lowest rotational levels of CO molecule are most effective in producing a signal by scattering.

## 4.2.1 The three critical densities

Therefore, we have encountered *three* types of critical densities in this chapter, characterizing the effect of collision in an atom or molecule. The first type is important for observation of individual objects, as it determines when an object can no longer be visible from the change in its brightness temperature caused by scattering. This density depends linearly with the peculiar velocity of the objects, hence one has better chance of observing the scattering signal in galaxies with high peculiar velocity. The second critical density is when the level populations start to deviate significantly as a result of collision, which we have arbitrarily defined for a change of 30% from the fraction governed by $T_{CMB}$ alone. Between the first and second critical densities, scattering as a process still compares with that of emission, and we shall see in a subsequent section (Ch.5) that one can pick up the *integrated* signal of scattering from all objects below the second critical density through the power spectrum distortions of the CMB. Above the third critical density, which is

## 4. THE THREE CRITICAL DENSITIES
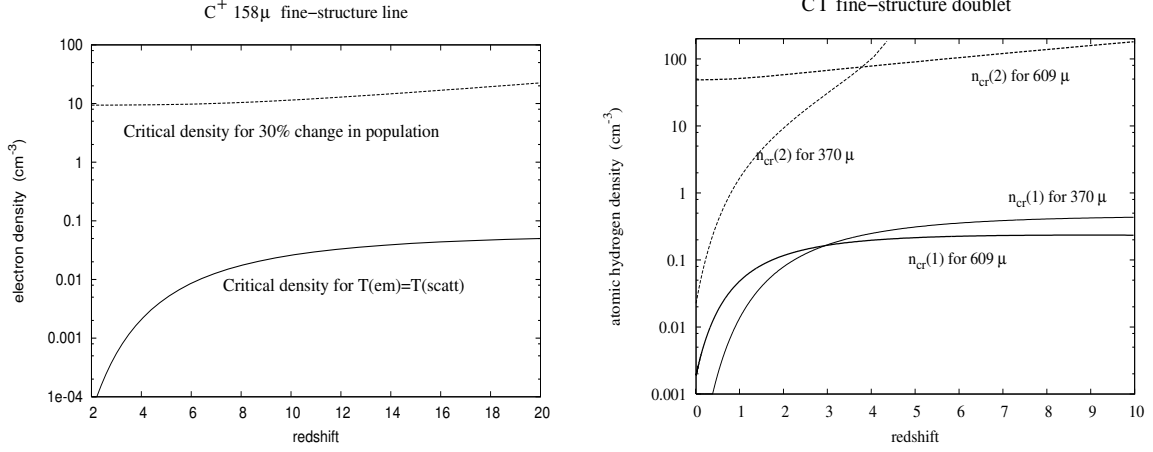


Figure 4.5: Two types of critical densities for neutral and singly ionized carbon fine-structure lines, as function of redshift. **Left:** Result for the ionized carbon FS singlet, in collision with electrons at $\sim 10^4$ K. The first critical density is extremely low here as collisions of $C^+$ with electrons are extremely effective in exciting this system. **Right:** Results for CI FS doublet in collision with *atomic hydrogen*, showing both the $609\mu$ (thick lines) and the $370\mu$ (thin lines) fine-structure lines. The first type (marked *(1)*, solid lines) is when brighness temperature of an object is dominated by the effect of line emission. The second type (marked *(2)*, dashed lines) is when population of the levels change by 30%, and collisional process starts to dominate.

defined classically by the ratio $A_{ul}/\gamma_{ul}$, scattering is no longer of significance and one can expect only emission in the lines.

These three densities are best understood in terms of the change of the excitation temperature of the transition, defined through eqn.(4.1). We show in Fig.(4.6) for the second CO rotational transition of 230 GHz. We plot how the excitation temperature varies in a wide range of $H_2$ molecular densities at $z = 0$. The excitation temperature is defined in terms of level populations, $\varpi_u/\varpi_l = g_u/g_l \exp(-h\nu_{ul}/kT_{ex})$, and is equal to the background CMB radiation temperature at low densities. As the density increases, excitation temperature starts to deviate significantly from CMB temperature, and it asymptotically reaches the gas kinetic temperature at very high densities. We note that even when $T_{ex}$ is equal or nearly equal to the $T_{CMB}$, emission can be more effective. The gray area marks the density range when scattering can dominate over emission in the CO line.

We make some brief remarks about the excitation temperature at the third critical density, when the collisional process dominates completely. For two-level systems, it is very easy to write the excitation temperature at $n = n_{crit}$ where $n_{crit} \equiv A_{ul}/\gamma_{ul}$ (see, e.g. Genzel 1991). In presence of CMB radiation with temperature $T_{CMB}$, we get the following formula

$$T_{\mathrm{EX}} = \frac{T_{\mathrm{CMB}} + \frac{h\nu}{k}}{1 + \frac{h\nu}{kT_{kin}}} \approx \left[ \left( \frac{h\nu}{k} \right)^{-1} + T_{kin}^{-1} \right]^{-1} \qquad (4.12)$$
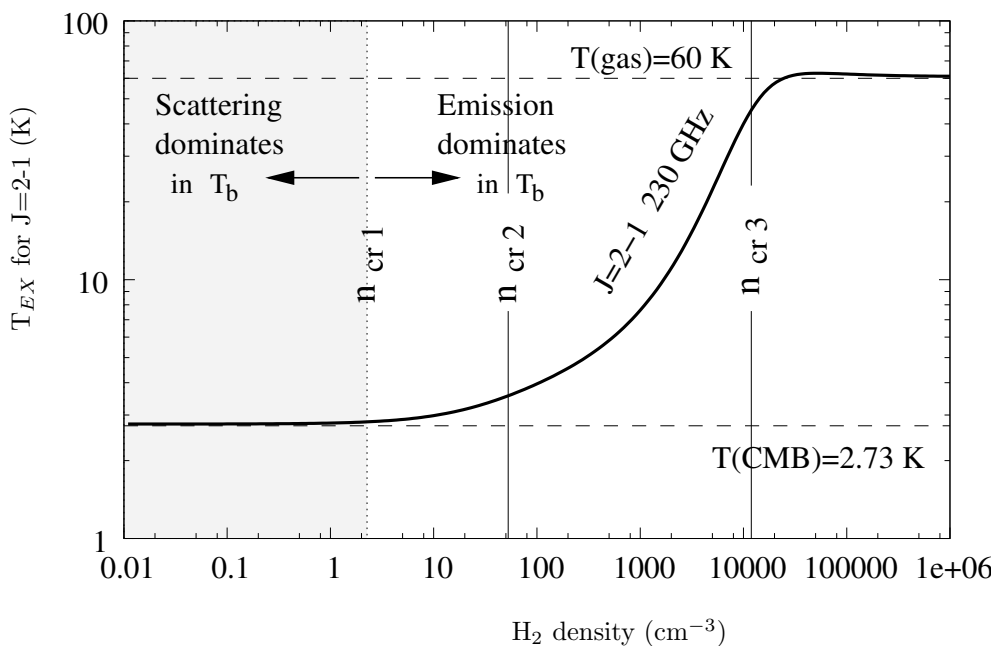
Figure 4.6: Three kinds of critical density discussed in this section, for the *second* rotational transition of CO molecule at $z = 0$. $n_{cr1}$ is the average density of an object above which its brightness temperature due to emission starts dominating over that from scattering. $n_{cr2}$ is the density when population of any given level starts to deviate significantly from its thermal equilibrium value set by the background CMB temperature. The density limit in the plot corresponds to 30% deviation. The third critical density, is the classical one, defined as $n_{cr3} = A_{ul}/\gamma_{ul}$ for that particular transition. Above this density collisional de-excitation probability from the upper level starts to dominate and the effect of radiation field becomes insignificant.
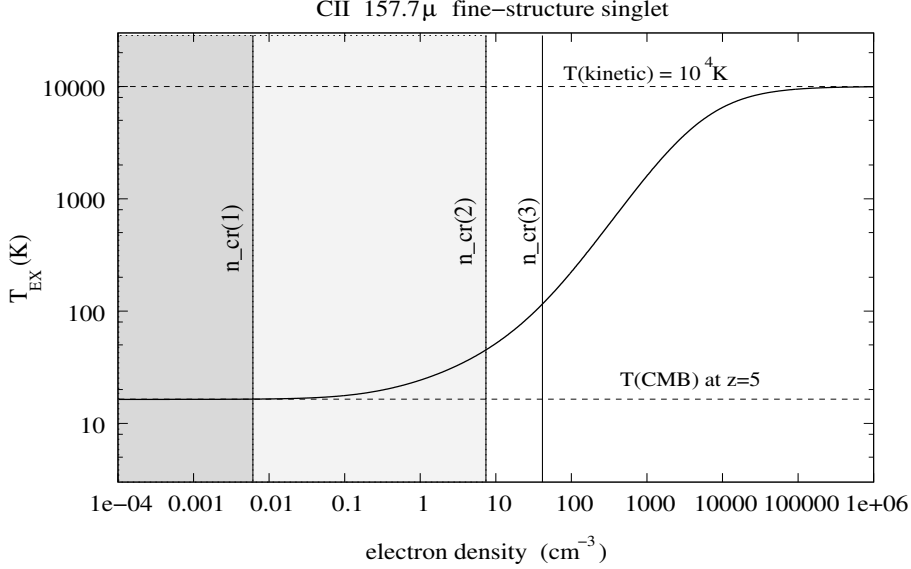
Figure 4.7: Excitation temperature for $C^+$ 2-level system at z=5, again showing the location for the three critical densities characterizing the importance of the scattering process at various densities of electrons. The background CMB radiation has temperature about 16 K, and the kinetic temperature of electrons is $10^4$K. The first critical density, below which an object will be visible from scattering, is unacceptably low for such ionic fine-structure transitions, because they are very easily excited by collisions of electrons. Objects with densities between the first and the second critical densities might leave their signature of scattering through distortion in the angular temperature fluctuations of the CMB, which is the topic the of next chapter.

where the second step is valid under the approximation $h\nu/k \gg T_{\mathrm{CMB}}$ at that redshift. This shows clearly that with the above definition of critical density, we have $T_{\mathrm{EX}} \neq T_{kin}$ at that limit if $T_{kin}$ is much larger than the level energy, $T_{\mathrm{EX}}$ approaches asymptotically the kinetic temperature of colliding electrons only at much higher densities, as shown in Fig.(4.7). Here we have shown the case for $C^+$ 157.7$\mu$ two-level system in $10^4$K electron gas at redshift $z = 5$, so that $T_{\mathrm{CMB}}$ is about 16 K. $A_{ul}/\gamma_{ul} = 50$ cm$^{-3}$ for collisions with electrons, and the exitation temperature at this density is about 106 K, far below the $10^4$K asymptote. Collisional process completely dominates the level populations above this density, as had been discussed. Since these ionic fine-structure transitions are very easily excited collisionally by electrons, we have unacceptably low values for electron density when an object will be visible in scattering (the first critical density in figure). For computing this limit, however, we have again used the mean radial component of large-scale velocities at $z = 5$, which is about 140 kn s$^{-1}$.

To summarize, one has the possibility to observe individual objects through scattering only when the average density inside is below the first critical density. This density marks the point when collisions become more effective in producing photons in the line, thereby dwarfing the
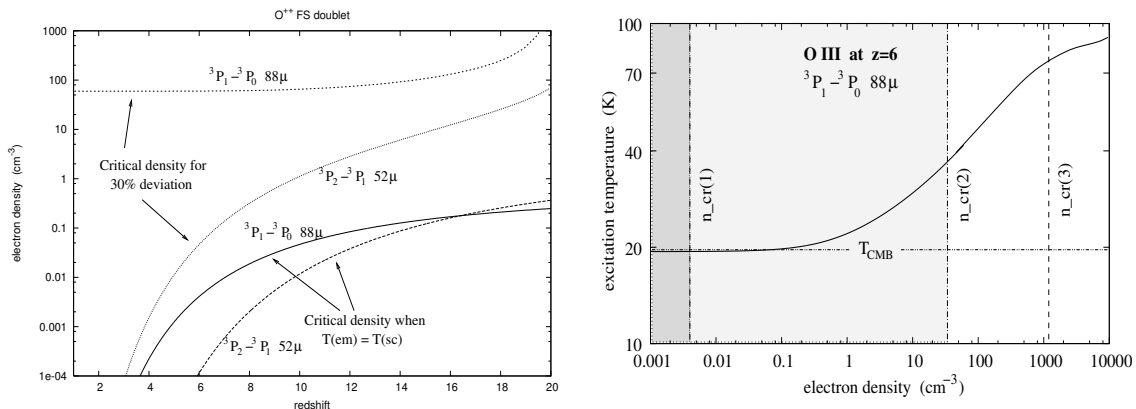
Figure 4.8: Another illustration of the concept of the three critical densities, with the help of $O^{++}$ $88\mu$ and $52\mu$ fine-structure doublet. In the *left* we show the redshift evolution of these densities, and in the *right* the case for the $^3P_1$-$^3P_0$ $88\mu$ line at $z = 6$, as such far-IR lines can only scatter CMB photons effectively at high redshifts. We plot both critical densities for the collision with electrons: the first one when brightness temperatures in scattering and emission become equal, and the second one when population in the lower transition level changes by 30%. We see that the first critical density corresponds to extremely low values, as the collision rates with electrons for these ionic lines are very high. The third critical density, $A_{ul}/\gamma_{ul}$, is 1700 cm$^{-3}$ for the $88\mu$ line, and 4350 cm$^{-3}$ for the $52\mu$ line, where collisions completely dominate level populations.

scattering signal. For atomic and ionic fine-structure lines in hot diffuse plasma, this transition occurs at very low densities because electrons are very effective collision partners for such lines. In neutral gas where the dominant collision partner is atomic or molecular hydrogen, one might have the possibility to observe individual objects through scattering in CO rotational lines, or even the neutral carbon FS lines. Especially in objects where the peculiar motion is particularly high, e.g. in Virgo cluster galaxies, this first critical density can be as high as $\sim$ 10-20 in neutral gas, making observation of temperature decrement through scattering a possibility. We must mention that CO may only be partially protected from the ionizing UV background under such low density environment, because of insufficient shielding by $H_2$ molecules. However the lower dissociation rate of CO compared to $H_2$ (Röllig 2002) can make trace amount of CO present at a fraction of its equilibrium abundance. The present day limit of existence of CO in low density neutral gas comes from the analysis of archived *Copernicus* data (Crenny & Federman 2004) of UV absorption against background stars, with CO column densities upto $\sim 10^{12} - 10^{13}$ cm$^{-2}$ and a corresponding neutral hydrogen density of $10 - 200$ cm$^{-3}$. The non-equilibrium processes in such low density environments can give rise to higher abundances of some other transitional species like $CH^+$. Therefore observation of temperature decrement by scattering in CO lines can in reality prove to be very difficult.

## 4. THE THREE CRITICAL DENSITIES

The scattering, as a process, is still comparable with line emission above the first critical density, unless the level population starts to change significantly due to collision. This marks the second critical density in our discussion, which we have defined as the point when level population changes by 30%. Above this density the radiation field due to CMB no longer controls the level population, and the amplitude of the scattering signal decreases rapidly. However, there is the possibility to pick up objects between the first and the second critical densities, from the *integrated* signal of scattering of all sources in the sky. This is because the contribution of emission from small individual sources is less important at large angles, where coherent smoothing of primordial CMB temperature fluctuations due to scattering is significant. This is the topic of the next chapter and the main conclusion of our work. We shall see that due to the frequency dependent nature of resonant scattering, one has the possibility to pick up the coherent scattering signal in correlation with the primordial temperature fluctuations in the CMB. The individual size of the scattering cloud is no longer important, because in the limit of very low optical depth one can safely assume the scatterers to be *uniformly* distributed in the sky. In other words, the mean free path of the scattered photons is much larger than the individual size of the objects, so the integrated scattering signal does not depend on the precise location of the scattering cloud. As a result of non-zero correlation (Hernández-Moteagudo & Sunyaev 2004) between the density fluctuations at the last scattering surface and at the epoch of scattering, the scattering signal is enhanced; and because of the frequency dependence its detection is no longer constrained by the limit of cosmic variance. Now we discuss the nature of this integrated signal of scattering, and the corresponding modifications in the CMB power spectrum.

# Chapter 5

# Distortion in the CMB Power Spectrum

## 5.1  Background and motivation

High precision observations of CMB anisotropies are giving us unique information about the angular distribution of CMB fluctuations, as well as their spectral dependence in a very broad frequency range. HFI and LFI detectors of PLANCK spacecraft will provide unprecedented sensitivity in 9 broad band ($\Delta\nu/\nu \sim 20 - 30\%$) channels, uniformly distributed in the spectral region of the CMB where contribution of different foregrounds are expected to be at a minimum. CMBpol and other proposed missions are expected to reach noise levels 20 - 100 times lower than that of PLANCK HFI with technology already available (Church 2002). The WMAP satellite was designed to provide measurements of the CMB temperature anisotropies in the whole sky with an average sensitivity of $35\mu$K per $0.3° \times 0.3°$ pixel at the end of the mission (Bennett et al. 2002, Page et al. 2002). Once such sensitivity limit is reached, the WMAP data will be the first real-life test for all those attempts to estimate, with extremely high precision, the key parameters of our universe using this sensitivity (Bond, Efstathiou & Tegmark 1997, Einsestein, Hu & Tegmark 1999, Prunet, Sethi & Bouchet, 2000). Indeed, after the first 12 months of operation, the WMAP team is recovering the first multipoles of the CMB power spectrum with an accuracy of a few percent (Hinshaw et al. 2003).

In this chapter we are presenting an additional use of the tremendous sensitivity of PLANCK and CMBpol, and ground-based experiments like ACT, APEX and SPT. We propose to look for or to place upper limits on the abundances of heavy elements present in the inter galactic medium and/or in optically thin clouds of gas everywhere in the redshift range $[1, 500]$. We shall focus on the fine-structure lines of neutral (CI, OI, SiI, FeI, ...) and ionized (CII, NII, OIII, ...) atoms, which might provide information about the epoch of first star formation and ionization history of the universe. Limits on abundances of heavy atoms and ions can be obtained by utilizing the

frequency dependent opacity that will be generated by scattering of background photons by these species; giving rise to different $\delta C_l$-s in different observing bands of the experiments. Although Planck HFI is expected to detect the combined signal from the strongest lines, like OI $63.2\mu$, CII $157.7\mu$ and OIII $88.4\mu$, future multichannel broadband CMB anisotropy experiments like CMBpol might permit to detect contributions from these lines separately from the epoch when dark ages were terminating, universe became partially ionized and heavy element production begun. It is important that the polarization signal arising due to resonance scattering depends strongly on the properties of the transition (Sazonov et al. 2002), and together with the temperature signal will permit us to separate contributions of different species.

The observed primordial acoustic peaks and angular fluctuations should not depend on the frequency at all. This is connected with the nature of Thomson scattering which produces these fluctuations both in the time of recombination of hydrogen in the universe (Peebles & Yu 1970, Sunyaev & Zel'dovich 1970) and during the secondary ionization of the universe (Sunyaev 1977, Ostriker & Vishniac 1986, Vishniac 1987, and more recently Gruzinov & Hu 1998, da Silva et al. 2000, Seljak, Burwell & Pen 2000, Springel, White & Hernquist 2001, and Gnedin & Jaffe 2001). In this context, WMAP polarization measurements have recently shown strong evidence favouring an early reionization scenario, with $z_r = 20^{+10}_{-9}$ (Kogut et al. 2003, 95% confidence). But if any amount of chemical elements are present during the dark ages, then these species will be able to scatter the CMB in their fine-structure lines. This scattering would not only partially smooth out primordial CMB anisotropies, but in addition will generate new fluctuations through the Doppler shift of the line associated with the motion of matter connected with the growth of density perturbations. The main difference with Thompson scattering is that the latter is giving us equal contribution over the whole CMB spectrum, whereas the discussed line scattering would give different contribution to different observing channels placed at different parts of the spectrum. Likewise, the contribution in this case would be restricted to a very *thin* slice in the universe. Hence there is a possibility to detect contribution from the lines with high transition probabilities, even though the typical optical depth we would find is very small ($\tau_\nu < 10^{-4}$). Since every line is able to work only in a given range of redshift, having observations on different wavelengths can give an upper limit to abundances of different species at different epochs. This method relies critically in the fact that intrinsic CMB temperature fluctuations are frequency independent. Therefore, in the absence of other frequency-dependent components, the difference of two CMB maps obtained at different frequencies must be sensitive to the difference in abundance of resonant species at those redshifts probed by the frequency channels. For this reason, this method is particularly sensitive to the possible presence of any frequency-dependent signal coming from foregrounds.

The idea to use the line transitions of atoms and molecules for modifying the CMB power spectrum is not new. Dubrovich (1977, 1993) proposed the use of rotational lines of primordial molecules (LiH, HD etc.) as a source of creating new angular fluctuations in the CMB, and

there have been attempts to observe these molecules at high redshifts (de Bernardis et al. 1993). Varshalovich, Khersonskii and Sunyaev (1978) were trying to estimate the spectral distortions of CMB due to absorption in fine-structure lines of oxygen and carbon at redshifts around 150-300 where the temperature of electrons should be lower than the temperature of CMB due to different adiabatic indices of radiation and matter (see Zel'dovich, Kurt & Sunyaev 1968). Suginohara et al.(1999) probed the possibility of detecting excess flux due to emission in these lines coming from very over-dense regions in the universe. Recently Loeb (2001) and Zaldarriaga & Loeb (2002) (hereafter ZL02) computed the distortions connected with the recombination of primordial Lithium and scattering in the Lithium resonant doublet line. Unfortunately the wavelength of fine-structure 2P-2S transition of Lithium atoms is too short and will be unobservable by PLANCK and balloon instruments. On the very low frequency domain, future experiments like SKA and LOFAR might detect signal from neutral hydrogen 21 cm line, which also carry important ioformation from high redshifts (Sunyaev & Zel'dovich 1975, Madau, Meiksin & Rees 1997). We consider below the ground-state fine-structure lines of heavier elements, with wavelengths of the order of $50 - 200\mu$, which will in principle be observable with PLANCK and CMBpol if they are present in the redshift range $[1, 500]$. The problem of overcoming their extremely small optical depth comprises the main idea of this thesis.

We will not discuss in detail the origin and ways of enrichment of the inter-galactic gas by heavy elements. This certainly requires existence of massive stars, supernova explosions, stellar and galactic winds, and even jets from disks around young stars with cold molecular gas (Yu, Billawala & Bally 1999). The main goal of this part is to show that the announced sensitivity of PLANCK detectors might permit us to set very strong upper limits to the time of enrichment of inter-galactic gas by heavy elements, the time of reionization, and maybe even to detect the heavy elements in the inter-cluster medium. The census of baryons in the local universe (Fukugita et al. 1998) shows that most of the baryon remains unobserved, and the proposed method might set way to detect its existence at high redshifts, when it had moderate or low temperature. These missing baryons are centainly out of stars, interstellar gas and intergalactic gas in clusters and groups of galaxies. However, we know that such baryons should exist because they have been detected by WMAP at the last scattering surface at $z \simeq 1100$, and are also necessary to justify the observed abundance of deuterium and $^6$Li in the early universe. Due to the wide range of redshifts under study, and the uncertain degree of mixture and clumpiness of our species in the interstellar and inter-galactic medium, we shall assume that all elements are smoothly distributed in the sky. In other words, in the present chapter we shall address exclusively the homogeneous low density optically thin case, where effects related to strong over-density of gas and collisional excitation are excluded and left as subject of an upcoming work. Resonant scattering effects will produce the discussed signal even if all the gas in the enriched plasma has over-density up to $10^3$. Under this *smooth* approximation, we will find that the effect of resonant species on the CMB power spectrum

will be particularly simple, especially in the high multipole range. Indeed, in the small angular scales, we shall show that the induced change in the $C_l$'s is given by $\delta C_l \simeq -2\,\tau_{X_i} C_l$, where $\tau_{X_i}$ is the optical depth induced by the resonant scattering of species $X$ and $C_l$ is the primordial CMB power spectrum, which is currently the main target of most CMB experiments.

## 5.2 Basic approach and formulation

We now discuss the method of obtaining the deviations in the CMB power spectrum by resonance scattering of atoms and ions, and using this deviation to constrain their abundance during the dark ages. The interaction of CMB photons with atoms and ions will mostly consist of resonant scattering with either an atomic or a rotational/vibrational transition, depending on the species under study. This scattering introduces a frequency dependent term in the evolution equation for the photon distribution function, which results in a frequency dependence drag-force. However, based on the same arguments of Zaldarriaga & Loeb (2002), we can safely ignore this drag-force as long as the characteristic time of drag exerted by these species is far larger than the Hubble time, which is indeed the case due to the low optical depths under consideration. Thereafter we detail how we introduce the optical depth due to the resonant transition ($\tau_{X_i}$) in the CMBFAST code (Seljak & Zaldarriaga, 1996). We consider a particular resonant transition $i$ for a given species $X$, with rest-frame resonant frequency $\nu_i$. The total optical depth encountered by CMB photons on their way from the last scattering surface to us is then obtained by adding the contributions from all lines to the standard Thomson opacity:

$$\tau = \tau_T + \sum_i \tau_{X_i} \tag{5.1}$$

In order to calculate $\tau_{X_i}$, we shall recur to the formula which gives the optical depth of a resonant transition in an expanding medium (Sobolev 1946),

$$\tau_{X_i}(z) = f_i\,\frac{\pi e^2}{m_e c}\,\frac{\lambda_i n_{X_i}(z)}{H(z)} \tag{5.2}$$

where $f_i$ is the absorption oscillator strength of the resonant transition, $\lambda_i$ is the corresponding wavelength (in rest frame), $n_{X_i}(z)$ is number density of $X$ species at redshift $z$, and $H(z)$ is the Hubble parameter at that epoch. The oscillator strength depends on $\lambda_i$, the Einstein coefficient of the transition $A_{ul}$, and the degeneracy of the levels involved in it:

$$f_i = \frac{m_e c}{8\pi^2 e^2}\frac{g_u}{g_l}\,\lambda_i^2 A_{ul} \tag{5.3}$$

A simple and elegant treatment following Gunn & Peterson (1965) using $\delta$-function line profile, instead of thermally broadened gaussian for the same line, gives same value of optical depth.

Further modifications are made to this formula to take into account the finite populations in the upper transition levels, which is important for atomic fine-structure transitions, where excitation temperature for them is comparable to the radiation temperature at high redshifts. Also the effect of non-zero cosmological constant can not be neglected in the low redshift universe of interest. Considering these facts, we obtain the following formula for optical depths:

$$\tau_{X_i}(z) \;=\; 1.7 \times 10^{-6} \; \left(\frac{\mathfrak{X}_{X_i}(z)}{10^{-6}}\right) \left(\frac{\mathcal{S}(z)}{\mathcal{S}(z=10)}\right) \; \left(\frac{\lambda_i}{100 \; \mu}\right) \left(\frac{f_i}{10^{-9}}\right) \; \mathcal{B} \tag{5.4}$$

Here $\mathfrak{X}_{X_i}(z)$ is the ratio between the number density $N_{X_i}(z)$ of the atomic or ionic species $X$ under consideration, with respect to the baryon number density at the same redshift: $N_b(z) = 2 \times 10^{-7} \; (1+z)^3 \; \mathrm{cm}^{-3}$. i.e. $\mathfrak{X}_{X_i}(z) = N_{X_i}/N_b$ presents the evolution of abundance of the given species due to element production, ionization and recombination processes. We propose to constrain the minimum abundance that can be detected at that redshift in *solar units*, or $[X]_{min} \equiv \mathfrak{X}_{X_i}(z) / \mathfrak{X}_{\odot}$, where, for example, $\mathfrak{X}_{\odot} = 3.7 \times 10^{-4}$ for carbon. $\mathcal{S}(z)$ gives the redshift dependence of optical depth in a $\Lambda$CDM universe: $\mathcal{S}(z) = (1+z)^3 \, [(1+z)^2(1+\Omega_m z) - z(2+z)\Omega_\Lambda]^{-\frac{1}{2}}$ (see, e.g., Bergstrom 1998) , and $\lambda_i$ is the wavelength in micron. The final term $\mathcal{B}$ accounts for the actual fraction of atom/ion present in their ground state, and is governed solely by the temperature of background radiation at the redshift of scattering. For a two-level system, this fraction is simply

$$n_l = [1 + (g_u/g_l) \; \exp(-h\nu_i/kT_0(1+z))]^{-1} \tag{5.5}$$

We also include here the correcting term for the induced emission in the presence of the CMB and finite population of the upper level:

$$\mathcal{B} = n_l \; \times \; \left[1 - \exp\left(-\frac{h\nu_i}{k_B T_0(1+z)}\right)\right] \tag{5.6}$$

The resonance scattering on ions and atoms in thermal equilibrium with black body radiation does not change its intensity. However, the observed CMB also has finite primordial angular fluctuations. The effect of resonant scattering is to decrease these angular fluctuations, and to bring the system more close to thermodynamic equilibrium. Therefore resulting fluctuations observed on the frequency of the line should differ from the situation on other frequencies which are far from the resonance.

At low multipoles peculiar motions arising due to the growth of large scale density perturbations become important. All ions or atoms are moving in the same direction and change the frequency of CMB photons during resonant scattering. This leads to generation of new anisotropies of background.

## 5.2.1 Method of computation

Our approach to model the coupling between these heavy species and CMB photons will be similar to that outlined in Zaldarriaga & Loeb (2002). In their paper they discussed modifications of CMB spectrum by presence of primordial Lithium atoms. Here we extend their analysis to other atoms and ions. We also discuss the necessary changes that are enforced while extending this method to all resonant species.

As a first step, we describe the modifications introduced in the CMBFAST code in order to compute the effect of resonant transitions. We consider a given resonant transition $i$ of a given species $X$, with a resonant frequency $\nu_{X_i}$. For a fixed observing frequency $\nu_{obs}$, the redshift at which that species interacts with the CMB is $1 + z = \nu_{X_i}/\nu_{obs}$, and its opacity can be written, in general, as $\dot{\tau}_{X_i} = \tau_{X_i} \mathcal{P}(\eta)$, with a normalized profile function $\int_0^{\eta_0} d\eta' \mathcal{P}(\eta') = 1$. We shall model this profile with a gaussian:

$$\dot{\tau}_{X_i} = \tau_{X_i} \frac{\exp\left(-\frac{(\eta-\eta_{X_i})^2}{2\sigma_{X_i}^2}\right)}{\sqrt{2\pi\sigma_{X_i}^2}} \tag{5.7}$$

where $\tau_{X_i}$ is the optical depth for the specific transition, $\eta_{X_i}$ is the conformal time corresponding to the redshift $1 + z_{X_i} = \nu_{X_i}/\nu_{obs}$ where scattering takes place, and $\sigma_{X_i}$ is the width of the gaussian. For a fixed transition, this width should be given by the thermal broadening of the line. For the sake of simplicity, we shall take $\sigma_{X_i} \sim 0.01\eta_{X_i}$.

Once the line optical depth has been characterized, (as shown in Section 2), the new opacity term with a gaussian profile is added to the standard Thompson opacity,

$$\dot{\tau} = an_e\sigma_T + \sum_i \tau_{X_i} \frac{\exp\left(-\frac{(\eta-\eta_{X_i})^2}{2\sigma_{\eta_{X_i}}^2}\right)}{\sqrt{2\pi\sigma_{\eta_{X_i}}^2}}, \tag{5.8}$$

and this in turn is used to compute the visibility function $\Upsilon(\eta)$, defined as

$$\Upsilon(\eta) = \dot{\tau}(\eta)e^{-\tau(\eta)}. \tag{5.9}$$

This scattering introduces a frequency dependent term in the evolution equation for the photon distribution function, which results in a frequency dependence drag-force. However, based on the same arguments of Zaldarriaga & Loeb, we can safely ignore this drag-force as long as the characteristic time of drag exerted by these species is far larger than the Hubble time, which is indeed the case due to the low optical depths under consideration. These are the modifications we introduced in the CMBFAST code in order to compute the CMB power spectrum under the presence of scattering by atoms and ions.

### 5.2.2 Nature of distortion in the CMB power spectrum

We next give a simple description of the modification of the power spectrum of the CMB when it encounters a resonant species. As mentioned in the Introduction, our first hypothesis will be that the species responsible for the scattering are homogeneous, isotropic and smoothly (i.e., not clumped) distributed in the Universe, at least during the epoch of interaction with the CMB. One may argue that heavy species are located in halos where the first stars are produced and that their distribution in the sky can non be regarded as *smooth*. In this case, the final effect would depend on the typical angular size of the patches in which the species have been spread and on their total sky coverage. This work will observe the case where those scattering patches percolate in the sky, giving rise to a smooth, homogeneous picture. The case of patchy distribution of emitting sources will be addressed in a forthcoming work, where collissional processes are studied in an extremely dense optically thick environment.

In the conformal Newtonian gauge, (also known as the longitudinal gauge), the $k$-mode of the photon temperature fluctuation at current epoch is given by (Hu & Sugiyama 1994)

$$\Delta_T(k, \eta_0, \mu) \;=\; \int_0^{\eta_0} d\eta \, e^{ik\mu(\eta-\eta_0)} \big[ \Upsilon(\eta) \left( \Delta_{T0} - i\mu v_b \right) + \; \dot{\phi} + \psi - ik\mu\psi \big] \qquad (5.10)$$

Here we have neglected the polarization term (which contributes at most with a few percent of the temperature amplitude). $\eta$ denotes the conformal time, $\Upsilon \equiv \dot{\tau}(\eta) \exp -\tau(\eta)$ is the visibility function and $\tau(\eta) = \int_\eta^{\eta_0} d\eta' \dot{\tau}(\eta')$ is the optical depth. $\Delta_{T0}$ accounts for the intrinsic temperature fluctuations, $v_b$ for the velocity of baryons and $\phi$ and $\psi$ are the scalar perturbations of the metric in this gauge. We have also neglected all tensor perturbations. If we now introduce the optical depth associated to a resonant transition as a Dirac delta of amplitude $\tau_{X_i}$ placed at $\eta = \eta_{X_i}$,

$$d\tau(\eta) = \sigma_T n_e(\eta) d\eta + \tau_{X_i} \delta(\eta - \eta_{X_i}) d\eta, \qquad (5.11)$$

we readily obtain that the original anisotropies have been erased by a factor $e^{-\tau_{X_i}}$, whereas new anisotropies have been generated at the same place:

$$\Delta_T(k, \eta_0, \mu) \;=\; e^{-\tau_{X_i}} \Delta_{T_{orig}}(k, \eta_{X_i}, \mu) \;+\; \Delta_{T_{new}}(k, \eta_{X_i}, \mu) \qquad (5.12)$$

In real space, if we assume that $\tau_{X_i} \ll 1$, the Dirac delta approximation for the resonant transition (eq.(5.11)) translates into

$$\frac{\delta T}{T_0}(\mathbf{n}, z=0) = (1 - \tau_{X_i}) \, \frac{\delta T}{T_0}(\mathbf{n}, z_{X_i}) + \tau_{X_i} \, \left. \frac{\delta T}{T_0} \right|_{new}^{lin} (\mathbf{n}, z_{X_i}) \;+\; \mathcal{O}\left[\tau_{X_i}^2\right] \qquad (5.13)$$

Here, $\mathbf{n}$ is the unitary vector denoting the observing direction, and $\delta T/T_0|_{new}^{lin}(\mathbf{n}, z_{X_i})$ is the linear in $\tau_{X_i}$ term of the newly generated anisotropies (in what follows, our temporal coordinate will be denoted by redshift or conformal time $\eta$ indiferently). We remark again that we are assuming that

the species is homogeneously distributed, so that $\tau_{X_i}$ does not depend on position. Let us now consider two different observing frequencies: the first one corresponds to the scattering redshift $z_{X_i}$, and the another corresponds to a scattering redshift too high to expect any significant presence of the species $X$. If we compute the correlation function, $\langle \frac{\delta T}{T_0}(\mathbf{n_1}, z = 0) \cdot \frac{\delta T}{T_0}(\mathbf{n_2}, z = 0) \rangle$, in both cases, we find that the difference of these quantities will be equal to:[1]

$$\Delta \left( \langle \frac{\delta T}{T_0}(\mathbf{n_1}, z = 0) \cdot \frac{\delta T}{T_0}(\mathbf{n_2}, z = 0) \rangle \right) =$$

$$\tau_{X_i} \Bigg( - 2 \langle \frac{\delta T}{T_0}(\mathbf{n_1}, z_{X_i}) \cdot \frac{\delta T}{T_0}(\mathbf{n_2}, z_{X_i}) \rangle$$

$$+ 2 \langle \frac{\delta T}{T_0}(\mathbf{n_1}, z_{X_i}) \cdot \frac{\delta T}{T_0} \Big|_{new}^{lin} (\mathbf{n_2}, z_{X_i}) \rangle \Bigg) + \mathcal{O} \left[ \tau_{X_i}^2 \right] \tag{5.14}$$

That is, the term linear in $\tau_{X_i}$ of $\Delta \left( \langle \frac{\delta T}{T_0}(\mathbf{n_1}, z = 0) \cdot \frac{\delta T}{T_0}(\mathbf{n_2}, z = 0) \rangle \right)$ is the sum of two different contributions: the suppression of original fluctuations (which, as we shall see, dominates at small angular scales), and the cross-correlation of the newly generated anisotropies with the intrinsic CMB field. The first term (suppression) does not depend on the potential or velocity fields during scattering, but only on the intrinsic CMB anisotropy field. Moreover, we must remark that those contributions are evaluated *at scattering epoch*[2]. Hence, if the resonant scattering takes place *before* reionization, the changes in the correlation function (or in the power spectrum, as we show below) will be sensitive to the CMB anisotropy field *before* being processed by the *re*-ionized medium. In the Appendix A we give a detailed computation of the change in the power spectrum due to a resonant line, which were done by C.Hernández-Monteagudo. As we concentrate in the optically thin limit, it is possible to make a power expansion on the optical depth $\tau_{X_i}$:

$$\delta C_l \equiv C_l^{X_i} - C_l = \tau_{X_i} \cdot \mathcal{C}_1 + \tau_{X_i}^2 \cdot \mathcal{C}_2 + \mathcal{O}(\tau_{X_i}^3). \tag{5.15}$$

In this equation, $C_l^{X_i}$ and $C_l$ refer to the angular power spectrum multipoles in the presence and in the absence of the $X_i$ resonant transition, respectively. For the limit of very small $\tau_{X_i}$ one can retain only the linear order, and a direct identification of $\delta C_l$ with the abundance $[X](z)$ is possible by means of eq.(5.4): the change induced in the CMB power spectrum will be proportional to the abundance of the species responsible for the resonant scattering. In agreement with what has been established when studying $\Delta \left( \langle \frac{\delta T}{T_0}(\mathbf{n_1}, z = 0) \cdot \frac{\delta T}{T_0}(\mathbf{n_2}, z = 0) \rangle \right)$, we find that $\mathcal{C}_1$ changes sign at some multipole $l_{cross}$: positive values of $\delta C_l$ imply generation of new anisotropies ($l < l_{cross}$), whereas anisotropies are suppressed for $l > l_{cross}$ (see figure 5.1 at very low $l$). In the Appendix A

---

[1]This type of manipulations of the correlation function/power spectrum which avoids the Cosmic Variance limit is possible as long as the weak signal (signal induced by scattering in this case) has different spectral dependence than the CMB.

[2]The dependence on cosmic epoch of eqs. (5.13,5.14) has been simplified. We again refer to Appendix A for a formal derivation.

we note that positive values of $\delta C_l$ (generation) are due to the non-zero correlation existing between anisotropies generated during recombination and those generated during the resonant scattering. This correlation is due to the coupling of $k$ modes of the initial metric perturbation field in scales of the order or larger than the distance separating the two events (recombination at redshift 1100 and resonant scattering at redshift 5-25).



PSfrag replacements

$\log([O]_{min}/[O]_\odot)$
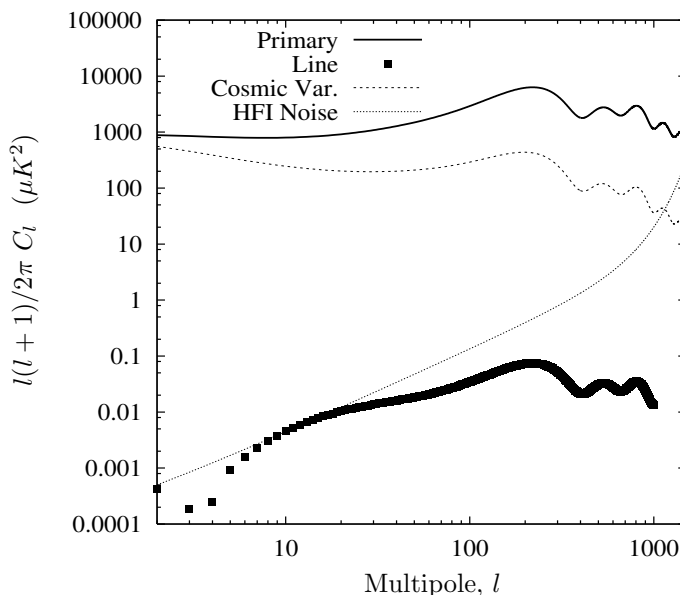
Figure 5.1: The nature of temperature anisotropy that will be marginally detectable with Planck HFI 143 GHz channel, using $63\mu$ OI line. Abundance is taken from the table(5.2), as $5.3 \times 10^{-4}$ solar at redshift 32. Here **Primary** denotes the measured temperature anisotropy (*upper line*), $C_l^{pri} + \delta C_l \approx C_l^{pri}$, and **Line** denotes the newly generated anistropy, $|\delta C_l|$, arising from line scattering (*bottom, with filled squares*). This $|\delta C_l|$ is obtained by taking the difference from the 100 GHz channel, and changes sign around $l = 3$. The corresponding noise level is denoted by **HFI noise**. Also shown is the cosmic variance limit (*short-dashed line*) for comparison.

### 5.2.3 $\delta C_l$'s at small angular scales

With respect to the high-l range, we find that the change induced in the power spectrum takes a very simple form:

$$\delta C_l \simeq -2 \, \tau_{X_i} \, C_l \tag{5.16}$$

where $C_l$ is the intrinsic power spectrum. This dependence is identical to the effect of reionization on the power spectrum at small angular scales. Indeed, in that scenario, if the optical depth due to electron scattering during this epoch is given by $\tau_{reio}$, then we have that for $l \gg 1$ the intrinsic CMB power spectrum generated at recombination is suppressed by a factor $1 - \exp(-2\tau_{reio})$, or

$\approx -2\tau_{reio}$ if $\tau_{reio} < 1$. So in both (resonant and Thompson) scatterings, the shape of the induced change in the power spectrum is particularly simple and equal to $\delta C_l \simeq -2\tau\, C_l$, for a given optical depth $\tau$ and intrinsic power spectrum $C_l$. This simplifies considerably the effect of reionization on the $\delta C_l$'s induced by resonant transitions. Indeed, if the symbol $\Delta^{reio}$ denotes the difference of a given quantity evaluated in the presence and in the absence of reionization, then we have that, for high $l$, $\Delta^{reio}(C_l) = -2\tau_{reio}\, C_l$ and $\Delta^{reio}(\delta C_l) = -2\tau_{reio}\,(\delta C_l)$. This is shown in figure (5.2), where we plot the quantities $V \equiv \left|C_l^{reio}/C_l - 1\right|$ and $W \equiv \left|\left|\delta C_l^{reio}/\delta C_l\right| - 1\right|$, that is, the relative change of $C_l$ and $\delta C_l$ due to the presence of reionization. We have taken $\tau_{reio} = 0.17$. We see that, for high $l$, both $V$ and $W$ approach the limit $V \simeq W \simeq 2\,\tau_{reio}$, i.e., the effect of reionization is identical in the two cases.
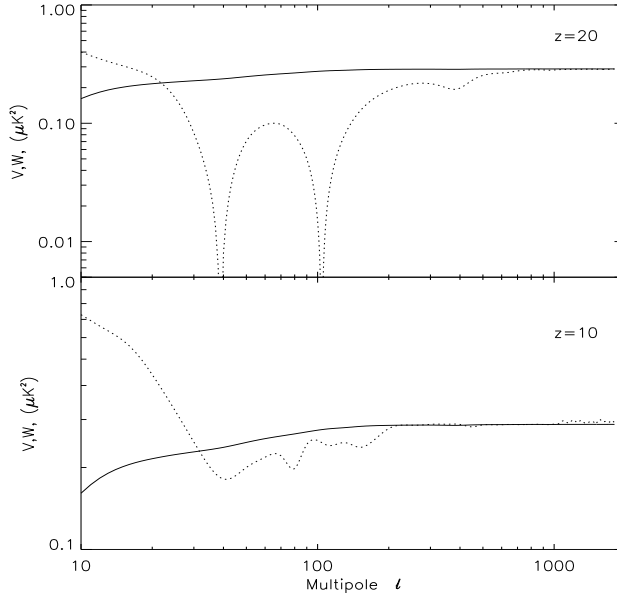


Figure 5.2: For two lines placed at different redshifts, ($z = 20$ in the top, $z = 10$ in the bottom), we plot the quantities $V$ (solid lines) and $W$ (dotted lines), defined as $V \equiv \left|C_l^{reio}/C_l - 1\right|$ and $W \equiv \left|\left|\delta C_l^{reio}/\delta C_l\right| - 1\right|$, respectively. In both cases, in the limit of high $l$, these quantities tend to $2\,\tau_{reio}$, where $\tau_{reio}$ was taken to be 0.17. In both panels, $\tau_{X_i} = 10^{-3}$.

## 5.2.4 Measuring $\delta C_l$'s and abundances

Next we investigate the limits of detectability of the optical depth of atoms and ionss in current and future CMB missions. Our starting point is the expected uncertainty in the obtained $C_l$'s from any CMB experiment (Knox 1995):

$$\sigma_{C_l}^2 = \frac{2}{(2l+1)\,f_{sky}}\left(C_l + w^{-1}B_l^{-2}\right)^2.\tag{5.17}$$

In this equation, $C_l$ is the underlying CMB power spectrum, $f_{sky}$ is the fraction of the sky covered by the experiment, and $w$ is the pixel weight given by $w^{-1} = \sigma_N^2 \Omega_{pix}$, with $\sigma_N$ the noise amplitude for pixels of solid angle $\Omega_{pix}$. $B_l$ is the beam window function, and we shall approximate it by a gaussian. We are assuming that the noise is gaussian, uniform and uncorrelated. The first term in parentheses of eq.(5.17) reflects the uncertainty associated to the cosmic variance. In the ideal case of an experiment with no noise, this would be the unavoidable uncertainty when identifying the *observed* $C_l$'s to the $C_l$'s corresponding to a particular cosmological model. However, our interest focuses on the comparison of power spectra measured in different frequency channels with respect to a *measured* reference power spectrum, (which is supposed to be free of any *contamining* species of atoms and/or ions). Under the assumption that the reference power spectrum contains only CMB and noise components, we can write the following expression for the uncertainty in the measured power spectrum difference between a *probe* channel and the reference channel:

$$\sigma_{\delta C_l}^2 = \frac{2}{(2l+1)f_{sky}} \Big[ \Big( \delta C_l^{prob} + w_{prob}^{-1} B_{l,prob}^{-2} \Big)^2 + \Big( w_{ref}^{-1} B_{l,ref}^{-2} \Big)^2 \Big]. \tag{5.18}$$

The indexes *prob* and *ref* refer to the *probe* and *reference* channel respectively, and the first term $\delta C_l^{prob}$ refers to the cosmic variance associated to the temperature anisotropies generated by the resonant species.

Let us now assume that a CMB experiment is observing at a frequency for which it is expected to see the effects of a resonant transition of a species $X$ at redshift $1 + z_{X_i} = \nu_{X_i}/\nu_{obs}$. One can then make use of eq.(5.15) to relate the minimum $\tau_{X_i}$ observable with the sensitivity of the experiment:

$$(\tau_{X_i})_{min} \simeq n \, \frac{\sigma_{\delta C_l}}{\mathcal{C}_1}. \tag{5.19}$$

The factor $n$ expresses the $\sigma$-level necessary to claim a detection. For all the results presented in this chapter, we have set the detection threshold at $3\sigma$, i.e. $n = 3$. Fig.(5.1) shows how a very low optical depth suffices to generate changes in the power spectrum (filled squares) which are big enough to overcome the combined noise of the two experiment channels being compared, (dotted line). Once this minimum optical depth is obtained, we can easily find the corresponding minimum abundance through eq.(5.4), which is one of the main goals of our work. In fact, this limit can be further improved by a factor of $\sim \sqrt{\Delta l}$ if one computes band power spectra on some multipole range $\Delta l$. We shall address the details of these issues in the next section, where we show that for PLANCK's HFI channels, values for the optical depth as low as $10^{-5} - 10^{-7}$ can be detected.

So far we are neglecting the problematic associated to the calibration between channels and the possible presence of foregrounds. Given the frequency dependent nature of the latter, the amplitudes and their characterization of the different galactic and extragalactic contaminants are critical for our purposes. We return to these issues in section 5, were we estimate the effect of

Planck HFI: Reference channel 100 GHz ($z = 46.5$)

| Frequency | Scattering redshift | $\tau$ for $10^{-2}[O]_\odot$ | angular scale | Minimum Abundance |
|---|---|---|---|---|
| 143 GHz | 32.2 | $9.9 \times 10^{-5}$ | $l = 12$ | $6.1 \times 10^{-4}$ |
| 217 GHz | 21.2 | $6.2 \times 10^{-5}$ | $l = 10$ | $2.0 \times 10^{-3}$ |
| 353 GHz | 12.5 | $3.1 \times 10^{-5}$ | $l = 8$ | $1.6 \times 10^{-2}$ |

Planck LFI: Reference channel 30 GHz ($z = 157.3$)

| Frequency | Scattering redshift | $\tau$ for $10^{-2}[O]_\odot$ | angular scale | Minimum Abundance |
|---|---|---|---|---|
| 44 GHz | 106.6 | $2.1 \times 10^{-4}$ | $l = 25$ | $5.7 \times 10^{-3}$ |
| 70 GHz | 67.1 | $1.7 \times 10^{-4}$ | $l = 19$ | $4.8 \times 10^{-3}$ |
| 100 GHz | 46.5 | $1.3 \times 10^{-4}$ | $l = 14$ | $4.2 \times 10^{-3}$ |

WMAP: Reference channel 23 GHz ($z = 205.4$)

| Frequency | Scattering redshift | $\tau$ for $10^{-2}[O]_\odot$ | angular scale | Minimum Abundance |
|---|---|---|---|---|
| 33 GHz | 142.8 | $2.4 \times 10^{-4}$ | $l = 29$ | $1.4 \times 10^{-1}$ |
| 41 GHz | 117.7 | $2.2 \times 10^{-4}$ | $l = 26$ | $1.2 \times 10^{-1}$ |
| 61 GHz | 76.8 | $1.8 \times 10^{-4}$ | $l = 21$ | $1.2 \times 10^{-1}$ |
| 94 GHz | 49.5 | $1.4 \times 10^{-4}$ | $l = 15$ | $1.3 \times 10^{-1}$ |

Table 5.1: Limit on neutral oxygen abundance using Planck and WMAP, from the 63 $\mu$ fine-structure line. The lowest frequency channel of each instrument is chosen as reference, and is assumed to be free of line contribution. Then each of the other channels act in a wide band of redshifts centered at scattering redshift $z_0$ (*column two*). We first compute the optical depth due to a fixed abundance (*column three*); and then find what optical depth, and hence abundance, will correspond to the instrument sensitivity (*last column*). The corresponding angular scales where this best limit is obtained is also shown (*column four*).

foreground contamination on our analysis.

## 5.2.5   Calculation of minimum detectable abundance

The basic idea of obtaining limits on abundances is described through Table(5.1), where we have shown results for individual detectors of Planck and WMAP. Each broad-band detector acts in a specific range of redshifts for a particular line, and we have tabulated the central redshift corresponding to the scattering of $63\mu$ OI line in *column two*. The lowest frequency channel of each instrument is assumed to be "clean" from line scattering, and thus used as reference. The central redshift for the reference channels are given at the top of each table. We use a fixed abundance ($10^{-2}$ solar) to obtain the optical depth in *column three*. Such small values of optical depths allow us to use the first-order approximation, and so we finally obtain the minimum optical depth , and hence the minimum abundance (*last column*, with respect to solar value) from the sensitivity level of the detector (at $3\sigma$ level). The angular scale where this best limit is obtained is also shown, which can be seen to increase with decreasing redshift, in correspondence with the increasing size of horizon length.
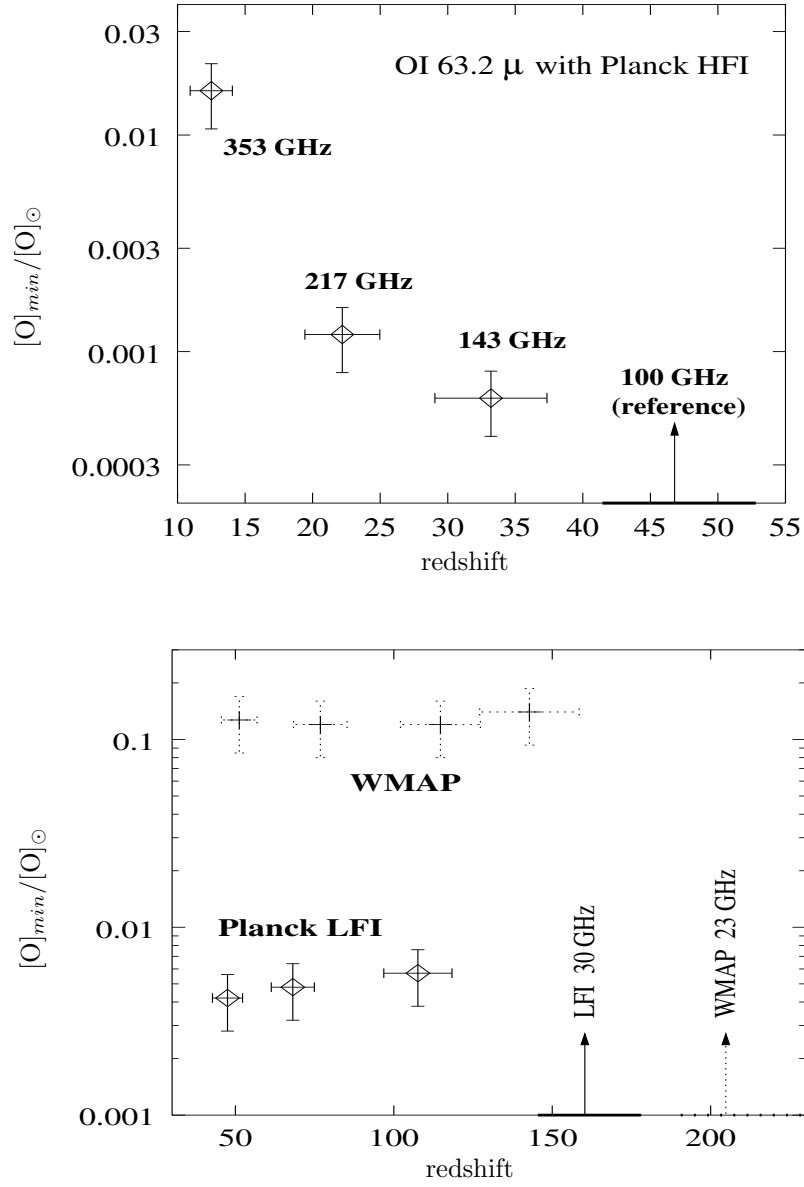
Figure 5.3: *Top*: Minimum abundance of neutral oxygen, from Planck HFI, with $63\mu$ line. Two data points are for 143 GHz and 217 GHz channels respectively, and position of the reference 100 GHz channel is shown by arrow. The thick horizontal line at the base of the arrow indicates the width of the reference channel. *Bottom*: Similar plot for Planck LFI and WMAP.

Fig.(5.3) shows this result graphically. For Planck HFI (*left panel*), these limits are obtained by taking difference from the 100 GHz channel (*position indicated by arrow*), which is our reference channel and assumed to be free of scattering effects. Two data points are for 143 GHz and 217 GHz channels respectively. The X-errorbar shows the bandwidth (assumed to be $\sim 25\%$), and Y-errorbar is given by $\Delta[X]_{min} \equiv [\partial[X]_{min}/\partial\delta C_l]\ \sigma_{\delta C_l} \approx [X]_{min}/3$ for limits obtained at $3\sigma$ level, where $\sigma \equiv \sqrt{\sigma^2_{C_l(1)} + \sigma^2_{C_l(2)}}$ and 1 & 2 denotes the two channels used for measuring $\delta C_l$-s (eqn.5.18). Similar plots from the same table with Planck LFI and WMAP are also shown in fig.(5.3). The bandwidths for the WMAP results are in accordance with the announcements of WMAP team (Page et al. 2003). Fig.(5.1) shows the expected behavior of $\delta C_l$-s when it is marginally detectable with the 143 GHz channel of HFI, limiting the oxygen abundance as low as $10^{-4}$ at redshift 30. We show both the measured temperature anisotropy and $\delta C_l$-s generated by line scattering in this plot. This line contribution touches the noise limit at around $l \sim 10$, showing the angular scale where best possible limit can be obtained. We see that this effect always lies much below the cosmic variance limit, but due to the frequency dependence of new anisotropies we are not constrained by this limit.

Fig.(5.4) shows the $l$-dependence of the minimum abundance obtainable. Its significance is pointed out in Appendix A, where we note that although suppression of primordial power spectrum of CMB occurs over all angular scales, new generation of anisotropy will only take place at low multipoles ($l \sim 10$) because the scattering takes place much later than recombination. Actually our method is strongest, and hence we can put most stringent limits, at that particular multipole value where Doppler generation is maximum. This multipole should correspond to the horizon scale at the epoch of scattering, and hence we will get better limits at larger angular scales when observing frequency is higher, i.e. scattering takes place at lower redshift. Exactly this behavior can be seen in fig.(5.4), where results from two HFI channels are shown. An important feature is that $l$-variation of $[X]_{min}$ is very slow, hence it is possible to take average limits from a band of multipoles of width $\Delta l$ instead of individual $l$, and thus improve the constraints by a factor of $\sqrt{\Delta l}$. This approach is demonstrated in Fig.(5.5), where the noise level of HFI chennels, and hence the minimum detectable abundance of the scattering species, is reduced by a factor of 3 by averaging the noise into bins of $\Delta l = 10$. In the present work, however, we show results without such averaging technique.

## 5.3 Main results for various atoms & ions

Now we present the results for selected atoms and ions and that can produce measurable distortions in the CMB spectrum. As mentioned previously, the focus will be on the fine-structure transitions

PSfrag replacements



PSfrag replacements
Multipole, $l$
$\log([O]_{min}/[O]_\odot)$
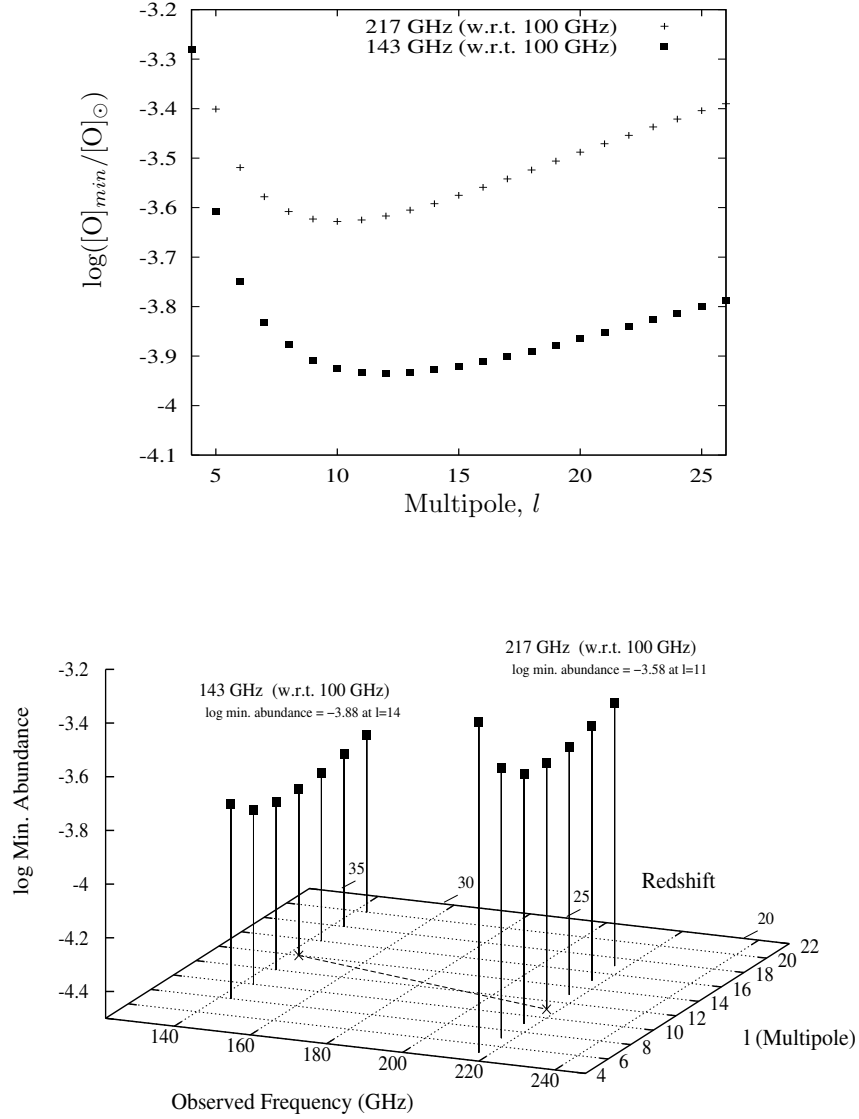
Figure 5.4: The minimum abundance of atomic oxygen at different multipoles, as deduced from Planck HFI 143 & 217 GHz channels. The reference channel used is 100 GHz, and the minima of such plots correspond to the $[X]_{min}$ values quoted in the text. We notice that angular scale for maximum deviation increases as the observed frequency increases, as discussed in the text.
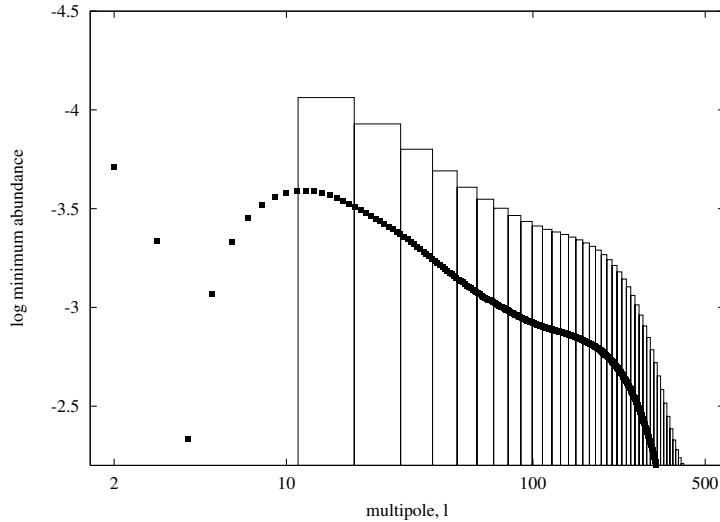
Figure 5.5: Figure showing how the prediction of minimum detectable abundance can improve if we average the instrument noise in bins of multipole $\Delta l$. This is possible because of the smooth variation of the scattering signal in a broad range of multipoles.

for atoms and ions , as their frequencies fall in the far-infrared and microwave range and are therefore perfectly suited to our purpose.

We divide this section into two parts: the first part shows results for all the important atomic and ionic species. In second part we briefly mention the contribution from the ovedense regions to the effect considered.

### 5.3.1    Scattering by atoms and ions of heavy elements

In this section we investigate the possibility of distorting the CMB power spectrum by scattering from neutral atoms like CI, OI, SiI, SI, FeI etc., as well as singly and doubly ionized species of heavy elements, like CII, NII, SiII, FeII, OIII etc. This is important for various reasons. The Gunn-Peterson effect permits us to prove that the universe was completely ionized as early as redshift 6, up to the position of most distant quasars known today. Recent results from WMAP satellite pushes the reionization redshift as far as $z = 20$, suggesting a complex ionization history (Kogut et al, 2003). There is extensive discussion about the nature of reionization, and also on the possibility for universe being reionized twice (Cen 2003). In any case, before the universe was ionized completely, there were regions of ionized medium around first bright stars and quasars. It will be difficult to prove that the universe was partially ionized using Ly-$\alpha$ line because of its extremely high oscillator strength, which makes the universe optically thick in this line even when the neutral fraction of Hydrogen is only $10^{-6}$ at $z = 6$. However, the infrared lines that we are discussing in this section have much weaker oscillator strength and therefore neutral gas is

| Atom/ Ion | Wavelength (in $\mu$) | Oscillator strength | HFI freq. (GHz) | Scattering redshift | $\mathcal{B}$ factor | Opt. depth for $10^{-2}$ sol. abun. | $[X]_{min}$ for $l = 10$ |
|---|---|---|---|---|---|---|---|
| **C I** | 609.70 | $1.33 \times 10^{-9}$ | 143 | 2.4 | 0.76 | $6.4 \times 10^{-6}$ | $5.3 \times 10^{-3}$ |
| | | | 217 | 1.3 | 0.92 | $3.9 \times 10^{-6}$ | $1.4 \times 10^{-2}$ |
| | | | 353 | 0.4 | 0.99 | $1.6 \times 10^{-6}$ | $2.1 \times 10^{-1}$ |
| | 370.37 | $9.08 \times 10^{-10}$ | 143 | 4.7 | 0.15 | $1.2 \times 10^{-6}$ | $2.8 \times 10^{-2}$ |
| | | | 217 | 2.8 | 0.09 | $3.7 \times 10^{-7}$ | $1.6 \times 10^{-1}$ |
| **C II** | 157.74 | $1.71 \times 10^{-9}$ | 143 | 12.3 | 0.79 | $1.8 \times 10^{-5}$ | $2.7 \times 10^{-2}$ |
| | | | 217 | 7.9 | 0.94 | $1.1 \times 10^{-5}$ | $7.7 \times 10^{-3}$ |
| | | | 353 | 4.4 | 0.99 | $5.6 \times 10^{-6}$ | $7.7 \times 10^{-2}$ |
| **N II** | 205.30 | $3.92 \times 10^{-9}$ | 143 | 9.2 | 0.76 | $1.1 \times 10^{-5}$ | $7.6 \times 10^{-3}$ |
| | | | 217 | 5.8 | 0.92 | $6.8 \times 10^{-6}$ | $8.6 \times 10^{-3}$ |
| | | | 353 | 3.1 | 0.99 | $3.5 \times 10^{-6}$ | $1.3 \times 10^{-1}$ |
| | 121.80 | $2.74 \times 10^{-9}$ | 143 | 16.2 | 0.16 | $2.1 \times 10^{-6}$ | $1.3 \times 10^{-1}$ |
| | | | 217 | 10.5 | 0.09 | $6.4 \times 10^{-7}$ | $3.4 \times 10^{-1}$ |
| **N III** | 57.32 | $4.72 \times 10^{-9}$ | 143 | 35.6 | 0.79 | $2.5 \times 10^{-5}$ | $2.3 \times 10^{-3}$ |
| | | | 217 | 23.4 | 0.94 | $1.5 \times 10^{-5}$ | $6.1 \times 10^{-3}$ |
| | | | 353 | 13.8 | 1.00 | $8.1 \times 10^{-6}$ | $3.1 \times 10^{-2}$ |
| **O I** | 63.18 | $3.20 \times 10^{-9}$ | 143 | 32.2 | 0.88 | $1.0 \times 10^{-4}$ | $5.3 \times 10^{-4}$ |
| | | | 217 | 21.2 | 0.96 | $6.3 \times 10^{-5}$ | $2.0 \times 10^{-3}$ |
| | | | 353 | 12.5 | 1.00 | $3.1 \times 10^{-5}$ | $2.2 \times 10^{-1}$ |
| | 145.53 | $1.85 \times 10^{-9}$ | 143 | 13.4 | .003 | $1.3 \times 10^{-7}$ | $1.6 \times 10^{-1}$ |
| **O III** | 88.36 | $9.16 \times 10^{-9}$ | 143 | 22.8 | 0.76 | $2.2 \times 10^{-4}$ | $3.5 \times 10^{-4}$ |
| | | | 217 | 14.8 | 0.92 | $1.4 \times 10^{-4}$ | $8.4 \times 10^{-3}$ |
| | | | 353 | 8.6 | 0.99 | $7.4 \times 10^{-5}$ | $1.2 \times 10^{-2}$ |
| | 51.81 | $6.55 \times 10^{-9}$ | 143 | 39.5 | 0.17 | $4.5 \times 10^{-5}$ | $1.4 \times 10^{-3}$ |
| | | | 217 | 26.0 | 0.10 | $1.4 \times 10^{-5}$ | $6.5 \times 10^{-3}$ |
| **Si I** | 129.68 | $6.24 \times 10^{-9}$ | 143 | 15.2 | 0.76 | $6.4 \times 10^{-6}$ | $6.9 \times 10^{-2}$ |
| | | | 217 | 9.8 | 0.92 | $4.2 \times 10^{-6}$ | $3.7 \times 10^{-2}$ |
| | 68.47 | $4.92 \times 10^{-9}$ | 143 | 29.7 | 0.19 | $1.8 \times 10^{-6}$ | $3.1 \times 10^{-2}$ |
| **Si II** | 34.81 | $7.74 \times 10^{-9}$ | 217 | 39.2 | 0.94 | $2.0 \times 10^{-5}$ | $4.8 \times 10^{-3}$ |
| | | | 353 | 23.4 | 0.99 | $1.0 \times 10^{-5}$ | $7.4 \times 10^{-3}$ |
| **S I** | 25.25 | $8.03 \times 10^{-9}$ | 217 | 54.4 | 0.96 | $6.0 \times 10^{-6}$ | $2.4 \times 10^{-2}$ |
| **Fe I** | 24.04 | $1.69 \times 10^{-8}$ | 143 | 86.4 | 0.83 | $3.2 \times 10^{-5}$ | $4.9 \times 10^{-3}$ |
| | | | 217 | 57.2 | 0.95 | $2.0 \times 10^{-5}$ | $7.7 \times 10^{-3}$ |
| | | | 353 | 34.4 | 0.99 | $9.7 \times 10^{-6}$ | $7.5 \times 10^{-2}$ |
| | 34.71 | $2.06 \times 10^{-8}$ | 143 | 59.5 | 0.02 | $9.2 \times 10^{-7}$ | $1.1 \times 10^{-1}$ |
| **Fe II** | 25.99 | $1.73 \times 10^{-8}$ | 217 | 52.9 | 0.95 | $1.9 \times 10^{-5}$ | $7.1 \times 10^{-3}$ |
| | | | 353 | 31.7 | 0.99 | $1.3 \times 10^{-7}$ | $7.4 \times 10^{-2}$ |
| **Fe III** | 22.93 | $3.09 \times 10^{-8}$ | 353 | 36.1 | 0.99 | $1.8 \times 10^{-5}$ | $4.2 \times 10^{-2}$ |

Table 5.2: Minimum abundance of the most important atoms and ions that can be detected from Planck HFI. We have used a fixed value of abundance (1% solar) to obtain the optical depth in the fine-structure transitions of any given species, and because of the very low values of optical depths, have used the linear relation from eqn.(5.19) to obtain the minimum detectable abundance for the sensitivity limit of Planck HFI. The $\mathcal{B}$ factor is the correction term obtained from eqn.(5.6). In the last column we have further improved the sensitivity by averaging the instrument noise in the multipole range $l = 10 - 20$. The 100 GHz channel has been used as reference for all the cases. We present central redshift for corresponding channel, however, in reality HFI will be able to give limits only for redshift intervals corresponding to the widths of frequency channels.

transparent in these lines up to very high redshifts, even if we assume solar abundance. This fact permits us to consider the possibility that Planck and other future CMB experiments setting very strong limits on abundance of neutral atoms in the early universe.

The effect of line emission to the thermal spectrum of CMB can be estimated in a simple order-of-magnitude way by the formulation given in Chapter 3. If there were significantly over-dense regions at high redshifts (up to $z \sim 20$) which were completely ionized and enriched with metal ions (e.g. $C^+$, $N^+$, $O^{++}$, $Fe^+$ etc.), then collisional excitation followed by radiative de-excitation will be a significant source of emission in the same fine-structure lines. However, to make line emission visible we need three factors: high abundance of the elements, high density of the electrons in the strongly over-dense regions and large amount of over-dense regions in the volume which we are investigating. Hence it is much more promising to study angular distortions of the CMB generated by scattering from the low density regions of the universe, rather than studying distortions in its thermal spectrum, for constraining heavy element abundances at high redshifts. Such low density inter-galactic gas is believed to contain most of the baryonic mass of the universe, and possibly exists as warm/hot gas with $10^5 < T_e < 10^7$ K today (Cen & Ostriker 1999). But at redshifts $z > 1$ this inter-galactic gas should have moderate ($T_e \sim 10^4$ K) or low ($T_e \sim T_{CMB}(z)$) temperature, and the proposed method of observing angular fluctuations caused by scattering from neutral or singly ionized atoms might set a direct way to detect its existence.

As mentioned above, the main contributors of opacities in the relevant frequency range are oxygen, nitrogen, carbon, sulfur, silicon, and iron, along with minor contributions mainly from phosphorus, aluminum, chlorine and nickel. The $63\mu$ fine-structure line of neutral oxygen gives strong constraint on neutral species at high redshift, but early reionization makes lines of CII, NII and OIII even more important. All data relating to fine-structure lines have been taken from the ISO line-list for far-IR spectroscopy (Lutz, 1998), and the Atomic Data for the Analysis of Emission Lines by Pradhan and Peng (1995). When necessary, this compilation was supplemented by the freely available NIST Atomic Database[1].

The basic idea of obtaining limits on abundances can be understood from Fig.(5.1) and Table(5.2). Each broad-band channel of HFI acts in a specific range of redshifts for a particular line, and we have tabulated the central redshift corresponding to the scattering for three most sensitive channels for several atomic and ionic fine-structure transitions. The lowest frequency channel of 100 GHz is assumed to be "clean" from line scattering, and thus used as reference. We use a fixed abundance ($10^{-2}$ solar) to obtain the optical depth in accordance with formula (5.4). Such small values of optical depths allow us to use the first-order approximation, and so we finally obtain the minimum optical depth , and hence the minimum abundance (*last column*, with respect to solar value) from the sensitivity level of the detector (at $3\sigma$ level). We have neglected signals below $l = 5$,

---

[1]http://physics.nist.gov/cgi-bin/AtData/lines_form

especially at the quadrupole or $l = 2$ where noise level is minimum, due to the fact that it will be very difficult to observe the predicted signal at such large angular scales due to the foregrounds. The best angular range for Planck HFI is $l \sim 10 - 30$, and we can average it over a multipole range $\Delta l$ and improve the detectibility by a factor of $\sqrt{\Delta l}$.

Fig.(5.1) shows the expected behavior of $\delta C_l$-s when neutral oxygen is marginally detectable with the 143 GHz channel of HFI, limiting the oxygen abundance as low as $10^{-4}$ relative to solar at redshift 30. We show both the measured temperature anisotropy and $\delta C_l$-s generated by line scattering in this plot. This line contribution touches the noise limit at around $l \sim 10$, showing the angular scale where best possible limit can be obtained. We see that this effect always lies much below the cosmic variance limit, but due to the frequency dependence of new anisotropies we are not constrained by this limit.

Part of the results of this section are summarized in Table 5.2. This lists all the atoms and ions on whose abundances we can put strong limits, and all these limits are computed at $3\sigma$ level. With HFI we have the possibility to use more than one probe channel to show different upper limits for the same species at different redshifts. This fact can be helpful to model the abundance history of the universe, and we present a general discussion in the next section.

### 5.3.2 Contribution from over-dense regions

Enrichment of primordial gas by heavy elements occurs due to supernova explosions of the first stars. High velocity stellar and galactic winds and low velocity jets from disks around forming stars, and objects of the type of SS 433 with baryonic jets carry enriched matter to a large distance from the forming stars. The observation of the most distant galaxies and quasars are showing that even most distant objects ($z \sim 5 - 6$) have chemical abundance on the level of solar (Freudling at al. 2003, Dietrich et al. 2003). At the same time there is a possibility that the low density matter, e.g. in future voids, will have extremely low abundance of heavy elements. Observational method we are proposing might permit us to observe ions and atoms of heavy elements in *diffuse matter*, with over-density lower than $10^3 - 10^4$ at redshifts $10 - 20$, and up to $\delta \sim 10^5 - 10^6$ at $z \sim 2 - 5$. This means that even Ly-$\alpha$ clouds are contributing to our effect. We should be careful only with the most damped Ly-$\alpha$ systems, and with dense gaseous nebulae of the type of Orion and dense giant molecular clouds. Diffuse gas in the galaxies and proto-galaxies should also contribute to our signal. In Chapter 3 we estimated the level of densities in the gas clouds, when the discussed effect is diminished by 30% or 50% in comparison with the case of diffuse inter-galactic space, and showed that over-densities greater than $10^3$ are needed at high redshifts before collisional effect begins to decrease amplitude of scattering signal. To summarize, the proposed method might permit us to get signal from all diffuse matter of the universe, excluding only the extremely over-dense, or optically thick clouds. It is probable that the over-dense regions were the first to be enriched by

heavy elements. Therefore it is important that the moderately over-dense regions of the universe are also contributing to the resonance scattering signal in the CMB angular fluctuations.

The simultaneous effect of free-free, line and dust emission from non-uniformly distributed over-dense regions at high redshifts, which are in non-linear stage of evolution and entering the state of intense star formation, produces an independent signal from the scattering effect considered in this chapter. The same lines which contribute to the $C_l$-s due to resonant scattering from extended low density regions, would also contribute to the power spectrum at smaller angular scales due to emission from over-dense regions. But over-dense objects like damped Ly-$\alpha$ absorbing systems and low density Ly-$\alpha$ clouds, together with stars, atomic and molecular gas in galaxies and hot gas in clusters, contains only 20% - 40% of the baryons in the universe (Fukugita et al. 1998, Penton et al. 2000, Valageas et al. 2001); meaning that resonance scattering from low density, optically thin gas with low temperature and moderate ($<10^3$-$10^5$, see discussion in Ch.3) over-density will always create its own distortion in the CMB power spectrum alongside the emission generated from denser regions. The former effect is sensitive to the mean density of resonant species, $\langle n_{X_i} \rangle$, whereas the latter probes the clumping of the matter, $\langle n_e\, n_{X_i} \rangle / \langle n_e \rangle \langle n_{X_i} \rangle$.

Both effects carry information about the abundances of atoms and ions averaged over the volume defined by multipole $l$ (or angular scale), and the frequency resolution of the detector which gives us the thickness of the slice in redshift space along line of sight. Future observations with sufficiently high spectral resolution might reveal that the signal due to suppression of primordial anisotropies at high $l$-s is analogous to the Ly-$\alpha$ forests averaged over a broad bandwidth ($\Delta z/z \sim$ 0.1-0.3). Resonant scattering effect is sensitive only to the mean density of the scattering species $\langle n_{X_i} \rangle$ in that volume, whereas the line radiation effect is connected with collisions and therefore its contribution to $C_l$'s depends on $\langle n_e n_{X_i} \rangle$ in the same volume. They are, thus, two independent effects that carry complementary information. This latter effect is sensitive to the most over-dense regions in the universe, and will be discussed in detail in the final chapter.

**Emission and change in the CMB thermal spectrum**

The line-emission processes results in a net injection of energy which should primarily be detectable via change in the thermal spectrum of CMB. However as have been mentioned, resonance scattering by atoms and molecules causes only an small change in photon energy, and thus in practice only modifies the angular power spectrum. Thomson scattering is still the dominant source of opacity; for example, if universe is completely reionized by $z = 20$, total Thomson optical depth is of the order of $\tau_{Thom} \sim 0.23$, whereas for singly ionized Carbon the optical depth for scattering at redshift 20 with the 157.7 $\mu$ line and full solar abundance is only $6.05 \times 10^{-3}$, which is about 40 times lower than $\tau_{Thom}$. But since this line opacity is frequency dependent, we have the possibility of detecting its effect on the CMB by our proposed method even when abundance is as low as $10^{-3}$ solar.

The effect of free-free and line emission to the thermal spectrum of CMB can be estimated in a simple order-of-magnitude way. If there were significantly over-dense regions at high redshifts (upto $z \sim 20$) which were completely ionized and enriched with metal ions (e.g. $C^+$, $N^+$, $Fe^+$ etc.), then collisional excitation followed by radiative de-excitation will be a significant source of energy input. In addition to that, free-free emission from the photoionized plasma along the line-of-sight (with electron temperature $T_e \approx 10^4 K$) will also play an important role. However, the FIRAS instrument on-board the COBE satellite has given us very strong limits for any possible distortion in the CMB spectrum (Fixsen 1996), permitting us to constrain the over-density $\langle n_e \rangle$ in any model of reionization. For example, if we consider free-free emission from a uniformly ionized universe upto redshift 20, temperature distortion observed today will be about $5.7 \times 10^{-8}$ K at 100 GHz, or near the peak of the CMB spectrum where most sensitive HFI channels are located. Comparing this with the limit on free-free distortion obtained from FIRAS data, $\Delta T_{ff} \leqslant 1.67 \times 10^{-5}$ K (Smoot & Scott 1996), we see that a mean over-density of $\sim 300$ is needed along the line-of-sight to make spectral distortions detectable at these frequencies. Distortions from collisionally excited line emission are even lower at these frequencies: e.g. with CII ion ($157\mu$) in hot electron plasma with 1% solar abundance at redshift 18, an over density of the order of $10^3$ is needed before effect of collision becomes important. Hence it is much more promising to study angular distortions of the CMB generated by scattering from the low density regions of the universe, rather than studying distortions in its thermal spectrum, for constraining heavy element abundances at high redshifts.

## 5.4 Effect of foregrounds

Before WMAP, the amplitude and spatial and frequency scaling of foregrounds had not been firmly established, and its modeling was merely in a preliminary phase. After their first mission year, WMAP's team have come up with a foreground model which is claimed to reproduce with a few percent accuracy the observed foreground emission (Bennett et al. 2003b). This and other future studies of foregrounds may provide a characterization of these contaminants such that their effect on our method can be minimized. We next proceed to estimate the impact of these contaminants on our method by the use of current foregrounds models.

We have adopted the *middle-of-the-road* model of Tegmark et al. (2000). This model studies separately the contribution coming from different components, giving similar amplitudes for those which are also modelled by the WMAP's team, (Bennett et al. 2003b). In this model, we will consider the contribution of five foreground sources, namely synchrotron radiation, free-free emission, dust emission, tSZ effect (Sunyaev & Zel'dovich 1972) associated to filaments and superclusters of galaxies, and Rayleigh scattering. The $l$-dependence of the power spectra was approximated by a power law for all foreground components, (except for tSZ, for which the model was slightly more
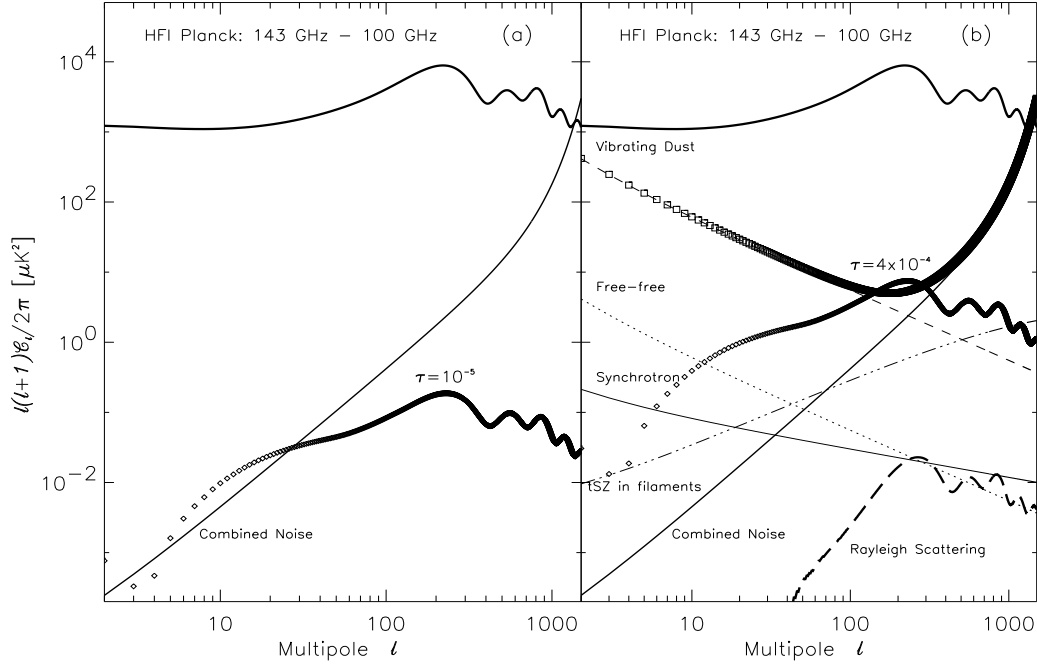
Figure 5.6: *(a)* Example of optical depth due to a resonant transition which can be detected by the HFI 100 GHz and HFI 143 GHz PLANCK channels in the absence of foregrounds. The upper thick solid line gives the reference model CMB power spectrum. Diamonds show the expected difference in the power spectrum from both channels due to the resonant scattering placed at $z = 25$ with $\tau = 1 \times 10^{-5}$. *(b)* Presence of foreground contamination after subtracting HFI 100GHz channel from HFI 143GHz channel. The reference $\Lambda$CDM CMB power spectrum is shown in thick solid line, whereas the instrumental noise after the map subtraction is shown in solid intermediate-thickness line. All thin lines refer to the foreground model as quoted as in Tegamrk et al. (2000): vibrating dust emission is shown by a dashed line, whereas free-free and synchrotron are given by a dotted and a solid thin line respectively. tSZ effect associated to filaments and superclusters is given by the triple-dot-dashed line. Rotating dust gives negligible contribution at these frequencies. Rayleigh scattering introduces some frequency-dependent variations in the $C_l$'s, but well below the noise level (thick dashed line at the bottom right corner). Diamonds show the amplitude of the change in the CMB power spectra induced by resonant species placed at $z = 25$ and $\tau = 3 \times 10^{-4}$.

sophisticated). The frequency dependence observed the physical mechanism behind each contaminant: simple power laws were adopted for free-free and synchrotron, whereas a modified black body spectrum was used for dust. For tSZ, the frequency dependence of temperature anisotropies is well known in the non-relativistic regime. All details about this modeling can be found in the paper of Tegmark et al. (2000). We are neglecting the contribution from the SZ effect generated in resolved clusters of galaxies which can be removed from the map. We are also assuming that all resolved point sources are excised from the map, and that the contribution from the remaining unresolved point sources ($\sigma_{ps}$ in eq.(10) of Tegmark et al.) can be lowered down to roughly the noise level. This may require the presence of an external point-source catalogue.

Fig.(5.6a) shows the expected precision level when foreground contaminations can be neglected, and Fig.(5.6b) shows the effect of foregrounds in our differential method to detect the presence of resonant species. Together with the power spectrum of our Standard $\Lambda$CDM model, (thick solid line at the top), we show the contribution from residuals of all foregrounds components under consideration, obtained after subtracting the HFI 100 GHz channel power spectra from the HFI 143 GHz one. The thin solid line corresponds to synchrotron emission, free-free emission is given by the dotted line; the dashed line gives the contribution of dust through vibrational transitions. The tSZ associated to filaments is shown by the triple-dot-dashed line, and the contribution from the combined noise of both channels is shown by the solid line of intermediate thickness which crosses the plot from the bottom left to (almost) the top right corners. At these frequencies, the contribution of rotating dust is negligible, and the most limiting foreground is dust emission by means of vibrational transitions. Finally, the last frequency dependent contribution that we have considered corresponds to Rayleigh scattering. As shown in Yu, Spergel & Ostriker 2001, hereafter YSO, Rayleigh scattering of CMB photons with neutral Hydrogen atoms introduce frequency dependent temperature fluctuations. However, provided that $\tau_{Rayleigh} \propto \nu^4$, this process is only effective at high frequencies ($\nu \gtrsim 300$GHz), causing deviations of measured power spectrum from the model $C_l$'s of the order of a few percent. YSO characterized the Rayleigh scattering by introducing in the CMBFAST code a frequency dependent effective optical depth and a frequency integrated drag force exerted on the baryons. This last modification, which was neglected when considering resonant scattering, couples the evolution of the different temperature multipoles ($\Delta_{T,l}$) for different frequencies. However, this coupling is exclusively due to the dipole term $\Delta_{T,1}$, which, at the light of their results, is very similar for all frequencies. Taking the same dipole term for every frequency allows us evolving a separate system of differential equation for each frequency. The frequency dependent changes in the angular power spectrum, ($\delta C_l/C_l(\nu)$), obtained under this approximation are almost identical to those in YSO. For each channel pair under consideration, we computed the residual in the power spectrum difference due to these frequency dependence temperature anisotropies. We checked that this effect was always subdominant. In Fig.(5.6b), the

impact of Rayleigh scattering is shown by a middle thick dashed line at the bottom-right corner of the panel, for the particular comparison of the 100GHz and 143GHz channels.

The addition of all contaminants (foregrounds + noise) is given by squares. Diamonds show the change in the power spectrum associated to a resonant transition placed at $z = 25$ for optical depth $\tau = 3 \times 10^{-4}$. After comparing with Fig.(5.6a) we can appreciate how the presence of foregrounds affects our method in two different ways: *a)* it increases the minimum $\tau$ to which the method is sensitive by about two orders of magnitude, *b)* it changes the range of multipoles to look at, due mainly to the large typical angular size of dust clouds. In the particular case of HFI 100GHz-143GHz channels, one should focus on the range $l \in [100, 200]$ once the dust component is included rather than in $l \in [3, 10]$ for the foreground-free case. Recurring again to the linear dependence of $\tau$ versus the abundance, eq.(5.4), we see that this model of foregrounds increases by about two orders of magnitude the minimum abundance on which future CMB missions will be able to put constraints.
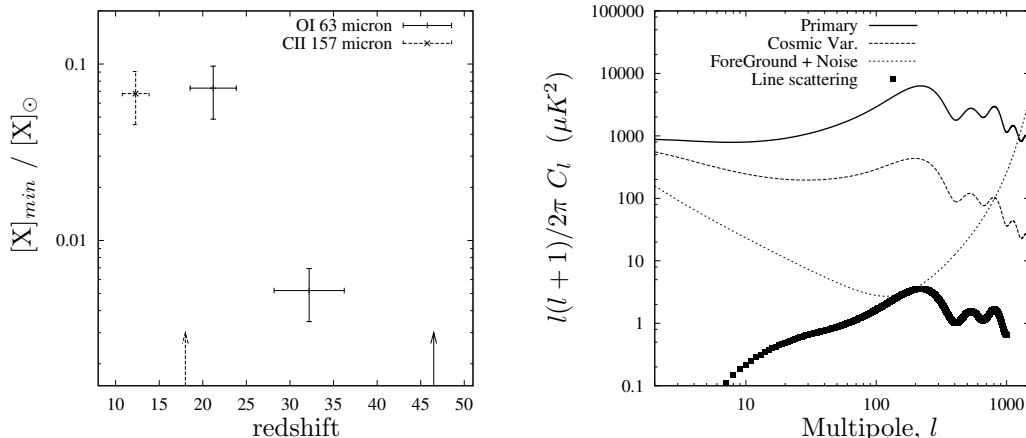


Figure 5.7: Minimum abundance of elements obtained when foregrounds are present. *Left :* Lowest abundance detectable of OI atoms with Planck HFI 143 & 217 GHz channels, and lowest value for CII ion with HFI 143 GHz channel. Arrows show position of reference channel for each. Here X denotes the atom/ion under study. *Right :* Nature of temperature anisotropy when neutral Oxygen abundance is $5.2 \times 10^{-3}$ solar at $z = 32$. We have shown again the primary temperature anisotropy and cosmic variance limit as before, but now the noise level is added with the *total* foreground emission at 143 GHz. As can be seen, best limit on abundance is obtained around $l \sim 175$.

Fig.(5.7) presents limits for atomic Oxygen and Singly ionized Carbon abundances when foreground emissions are present along with instrumental noise. We have used Planck HFI 143 and 217 GHz channels where these foreground contaminations are expected to be minimal. The angular scales where the best limits can be obtained from this combined noise+foreground map is also shown in the figure. In a similar fashion, for CO molecular abundance, the combined noise and foreground power spectrum for Planck HFI 143 GHz channel (again with 100 GHz channel

as reference) gives 0.05 $[C]_\odot$ at $z = 0.6$, and 0.08 $[C]_\odot$ at $z = 1.4$ respectively. Our hope is that with better understanding and modeling of these foreground emissions we will be able to reach a sensitivity level that is only constrained by instrumental noise.

One particular feature of minimum abundances obtained from foreground maps is worth mentioning. The presence of foregrounds significantly increases power in the lower multipoles, the main contributions coming from thermal emission from vibrating dust and free-free emission. Hence the combined foreground-noise curve have a minima around $l \sim 100$ (depending on instrument specifications), as can be seen from the *right* panel of fig.(5.7). Since we are comparing two different maps at two frequencies, the appropriate foreground-noise curve is also obtained from comparing two channels (HFI 100 and 143 GHz in this case). The $\delta C_l$ curve shown in the figure is obtained when neutral Oxygen abundance is 0.52% solar at redshift 32, using its 63 $\mu$ fine-structure line. The best constraint is obtained at $l = 175$, which is still much below the cosmic variance limit. At these smaller angular scales, the $\delta C_l$-s are essentially caused by suppression of primary anisotropy; whereas previously we had also generation at lower multipoles ($l \lesssim 10$) due to scattering at low redshift universe. Hence while obtaining limits from foreground (plus noise) maps, even though scattering redshift changes when observing frequency is changed, the angular scale corresponding to $[X]_{min}$ is insensitive to this change and does not correspond to the horizon scale at the epoch of scattering.

# Chapter 6

# Enrichment and Ionization Histories

## 6.1 The Ionization History of The Universe

Detection of the OI, CII and OIII lines of the two most abundant elements will permit not only to trace the enrichment of the universe by heavy metals, but also might open the way to follow the ionization history of the universe. According to recent models of stellar evolution very massive Pop III stars efficiently produce heavy metals like oxygen, carbon, silicon and sulfur (Heger & Woosley, 2002). The CNO burning phase of the stars appearing immediately afterwards will also produce large amount of nitrogen, and we can expect strong signal from the ionized nitrogen $205\mu$ line, as the time of evolution of the first stars is extremely short ($\sim 10^6$ years) in comparison with the Hubble time even at redshift 25.

The WMAP finding that universe has rather high optical depth due to secondary ionization at redshift $z_r = 20^{+10}_{-9}$ (Kogut et al. 2003, 95% confidence) forced many theoretical groups to return to the picture of early ionization due to Pop III stars (Cen 2003, Wyithe & Loeb 2003). One of the possible evolution scenario of abundances for the elements produced by these massive hot Pop III stars and intense star and galaxy formation is given in Fig.(6.1a). Here we consider two enrichment histories of the universe, with low ($A$) and high ($B$) metal abundances after reionization. The first phase of metal enrichment occurs during the epoch of Pop III stars, and at later epochs (redshift $3 - 5$) intense galaxy formation causes further rise in the metallicity. Later in this section we consider a third enrichment history with late reionization and metal injection.

In Fig.(6.1b) and (6.1c) , we sketch the relative ion fraction of the three most important atomic and ionic species under above-mentioned ionization history. We show two different reionization scenario: one for relatively cold stars when production OIII is less efficient (*case I*), and the other for hot stars and quasars which are able to keep oxygen fully ionized at all intermediate redshifts (*case*
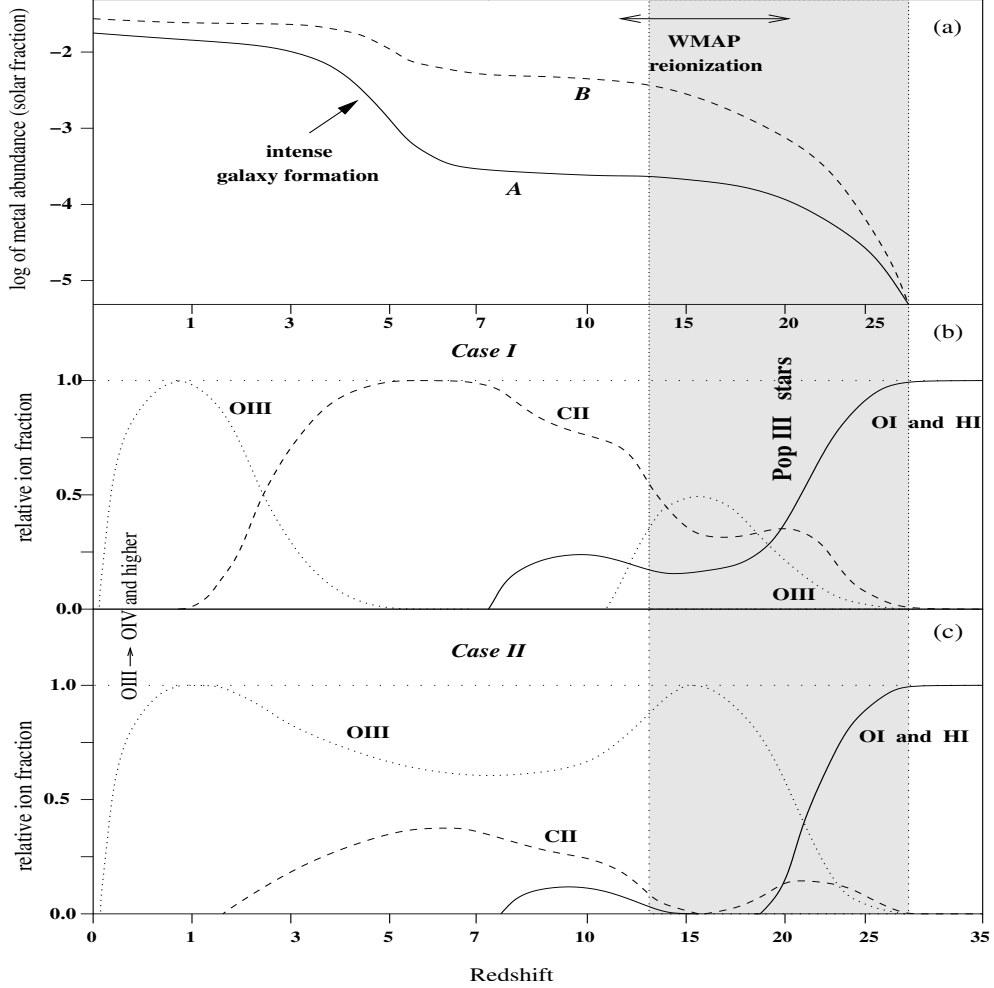
Figure 6.1: A schematic diagram for the abundance history of the universe. (*a*) The upper panel shows the global pattern of metal abundances, showing the two major epochs of enrichment of the IGM: first, during the peak of activity of massive Pop III stars around redshift $15 - 25$ (*shaded area*), and second, during the peak of galaxy formation around redshift $3 - 5$ when global rate of star formation reaches maximum. (*b*) Middle panel shows the relative fraction of three major atomic and ionic species: OI (or HI), CII and OIII, normalized so that the total abundance of all ions of a given element is close to unity at any redshift. The OI abundance closely follows the neutral hydrogen fraction of the universe because their almost similar ionization potential (see discussion in text). The redshift scale is chosen as $log(z + 5)$ to emphasize the redshift region $10 - 30$ of interest to this work. At very low redshifts ($z < 0.7$) the IGM gets heated to very high temperatures ($T \sim 10^5 - 10^7$ K) causing even higher ionized species to exist, e.g. OIII $\rightarrow$ OVI. (*c*) Lower panel shows another variation of relative ion fraction, where Pop III stars ionize all the oxygen around redshift 15, so that OIII have higher abundance and correspondingly OI and CII have lower abundance.
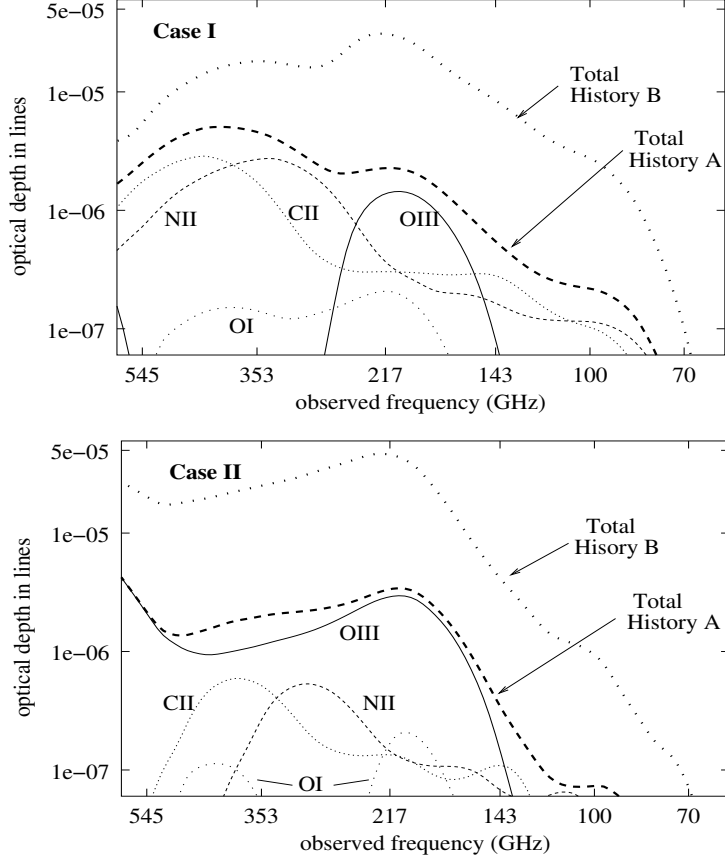
Figure 6.2:   Frequency dependence of optical depth in atomic and ionic fine-structure lines, in accordance with the abundance history sketched above. Shown here are the contributions from the four most important lines: neutral oxygen $63\mu$, doubly ionized oxygen $88\mu$, singly ionized nitrogen $205\mu$ and singly ionized carbon $158\mu$, and their total contribution for each histories. History of NII ion is taken as similar to that of CII ion.

II). Line of OI should give us an information about creation of oxygen before Universe was strongly ionised. Relative growth of CII line (see Fig.2b) will mark the time when carbon will be ionised in large ionised regions which do not completely overlap or will be partially ionised everywhere (we can not dinstinguish this two variants of ionization history using large angle observations). Potential of CI ionization (I=11.26 eV) is lower than that of HI. Therefore CII fraction might be higher than that of HII and OII in the beginning of secondary ionization. At the same time OI fraction should follow that of HI because ionization potentials are so close (I=13.62 and 13.60 eV correspondently). Pop III stars should be very hot, and therefore they are able to ionize helium early enough. Simultaneously OIII should become abundant ion because ionization potential of OII (I= 35.12 eV) is higher than that of HeI but smaller then that of HeII.
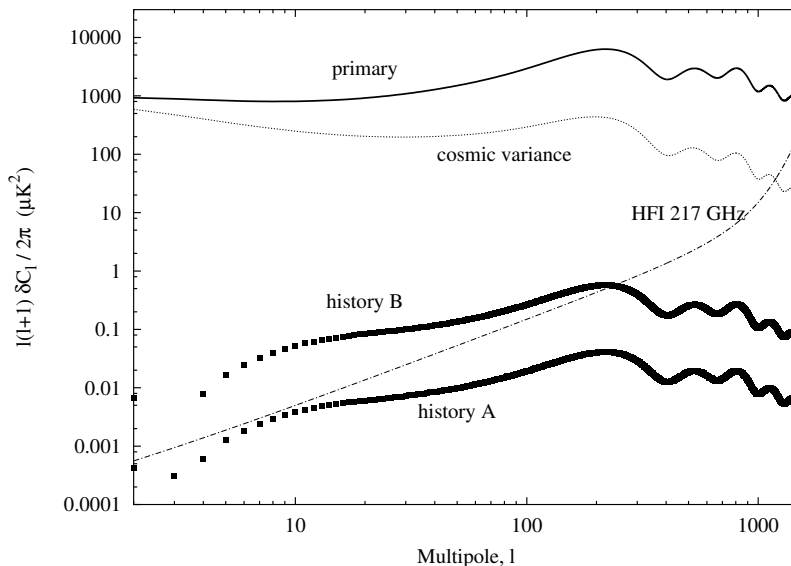
Figure 6.3: Predicted distortion in the CMB power spectrum as a result from scattering by OIII $88\mu$ line, for both history A (low abundance) and history B (high abundance).

Fig.(6.3) shows how the difference in global metallicities from history A and history B produce different levels of distortion in the CMB power spectrum. The example is chosen for OIII $88\mu$ fine-structure line as seen by the HFI 217 GHz channel, where the contribution comes from scattering at redshift $\sim 15$. The two histories presented here gives almost an order of magnitude difference in global metallicity at that redshift, which translates into an order of magnitude difference in the $\delta C_l$-s. We see that for $l \gtrsim 20$ both curves are exactly similar, demonstrating that at small angles we have $\delta C_l \simeq -2\tau C_l^{\mathrm{prim}}$. This fact will be demonstrated in further detail in the next subsection. Here we see how Planck HFI can put constraints on the enrichment history of the universe by ruling out certain models of abundances.

In Fig.(6.4) we show the angular dependence of the temperature anisotropy generated by resonant line scattering for the three important HFI channels. The abundance of CII ion is kept fixed at 10% solar, so that the lower observing frequency (i.e. higher scattering redshift) has a higher value of optical depth in the same line. The left-side of each curve is dominated by Doppler generation of new anisotropy, and hence are positive. The righ-side is dominated by suppression of primordial anisotropy and hence $\delta C_l$-s are negative, the discontinuity in each curve shows the interval where $\delta C_l$ changes sign. We see at low multipoles both generation and suppression term tend to cancel each other. Especially due to the adoption of WMAP reionization model with high optical depth ($\tau_{reio} = 0.17$) in our computations, lines which scatter CMB photons at redshifts $z \lesssim 18$ encounter a high value of visibility function due to reionization, and therefore causes a strong Doppler generation (but negative) in the multipole range $l = 20 - 100$. This is the cause
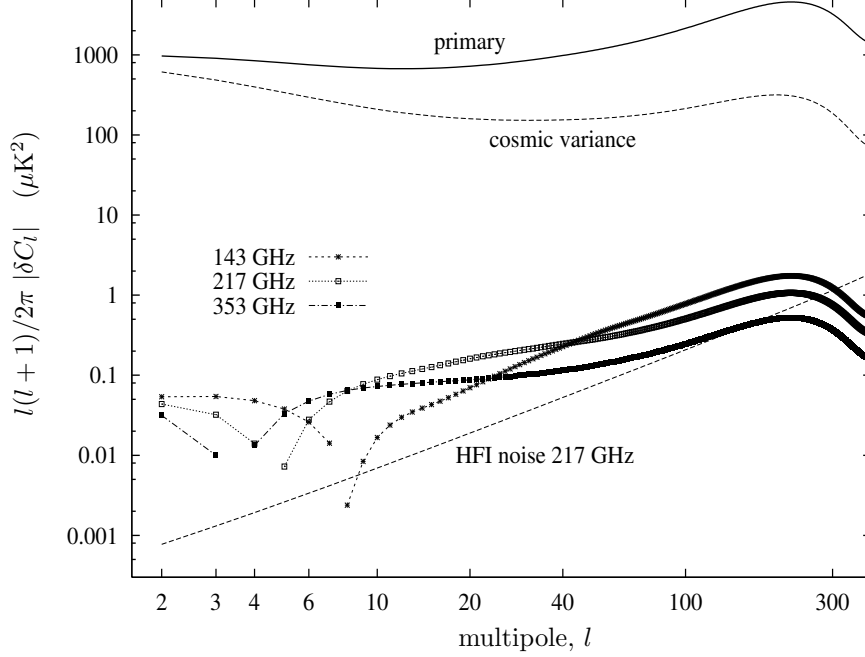
Figure 6.4: Angular dependence of temperature anisotropy generated by scattering from CII $158\mu$ fine-structure line. Shown here are three cases of $|\delta C_l|$ as should be observed from Planck HFI 143 GHz (scattering at $z = 12$), 217 GHz (scattering at $z = 8$) and 353 GHz (scattering at $z = 4$) channels, (using 100 GHz channel as reference)for 10% abundance of CII ions (with respect to solar) at all three redshifts. Also shown are the primary anisotropy, $C_l$, the cosmic variance limit, and noise level for 217 GHz channel (with respect to 100 GHz) for comparison.

for higher amplitude of the signal at 143 GHz. But at high multipoles $l > 100$ the contribution from Doppler generation is negligible, and the signal is simply proportional to the primordial $C_l$-s, and the line optical depth, provided $\tau \ll 1$. Hence using data from Table(5.2), and knowing the amplitude of primordial CMB signal, one can immediately predict the amplitude of the effect at small angular scales using formula(5.16).

Fig.(6.5) shows the amplitude of the predicted signal as a function of observing frequency, for a fixed angular scale $l = 10$. The contributions from four most important lines, viz. CII $158\mu$, NII $205\mu$, OI $63\mu$ and OIII $88\mu$, are shown, along with their sum. We also show four different redshift ranges for each line, which highlights the fact that contributions from CII and NII are higher because their signal is coming from lower redshifts where abundance is higher according to our chosen abundance history.

Fig.(6.6) summarizes our results for three different angular scales. As explained above, at low
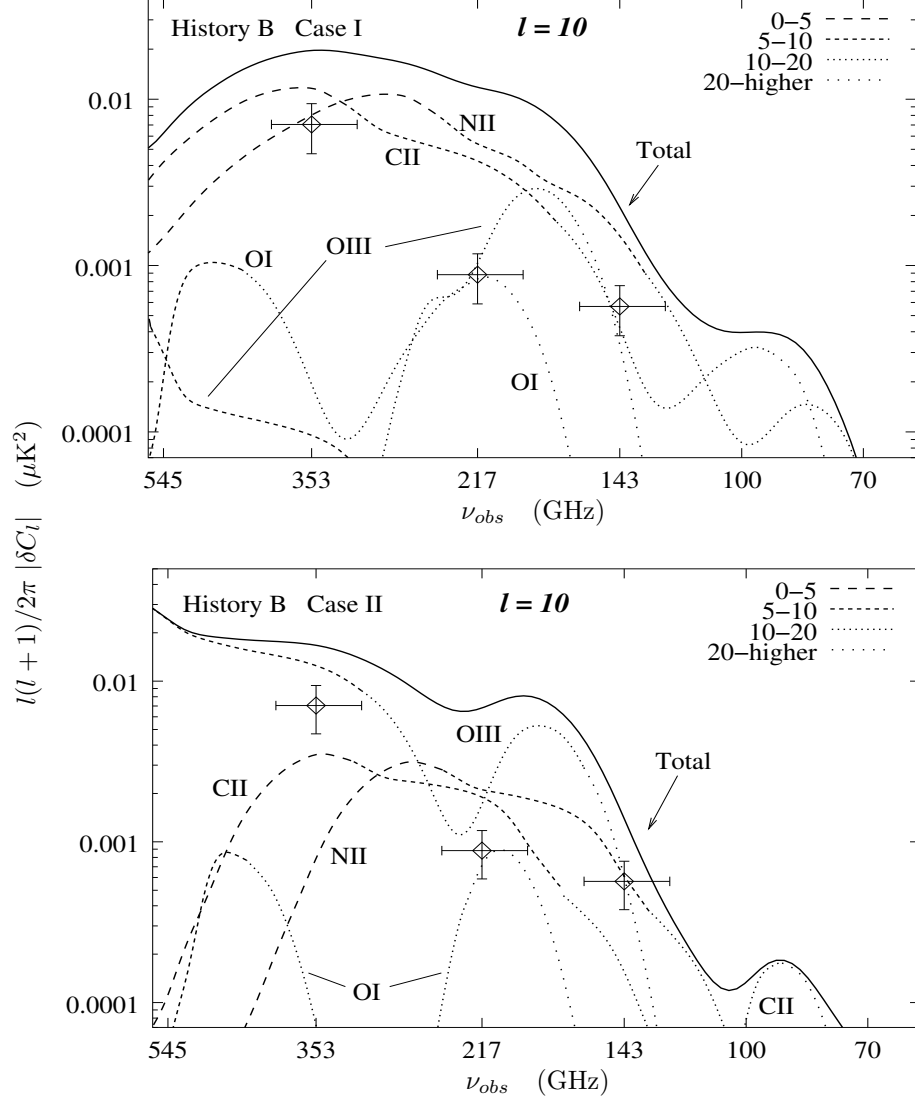
Figure 6.5:  Frequency dependence of temperature anisotropy generated by scattering from fine-structure lines. We take two ionization histories and the high abundance case from figure (6.1), and show the contributions of different lines in different frequency range, for a fixed multipole $l = 10$. Four different redshift ranges are marked for each species to emphasize the epochs where the dominant contribution from each lines are coming. The sensitivity limits of Planck HFI channels are marked by the crosses. The HFI limits have been improved by a factor of $\sqrt{\Delta l}$ by averaging over in the multipole range $l = 7 - 16$ . The sensitivity limits are for 3 standard deviation detection, and the *y-errorbars* correspond to $1\sigma$ error in $3\sigma$ detection (we recall that $\sigma = 3\sqrt{\sigma^2_{C_l(probe)} + \sigma^2_{C_l(ref)}}$, where the reference channel is fixed at HFI 100GHz). The *x-errorbars* corresponds to the wide bandwidth ($\sim 25\%$) of Planck HFI channels.
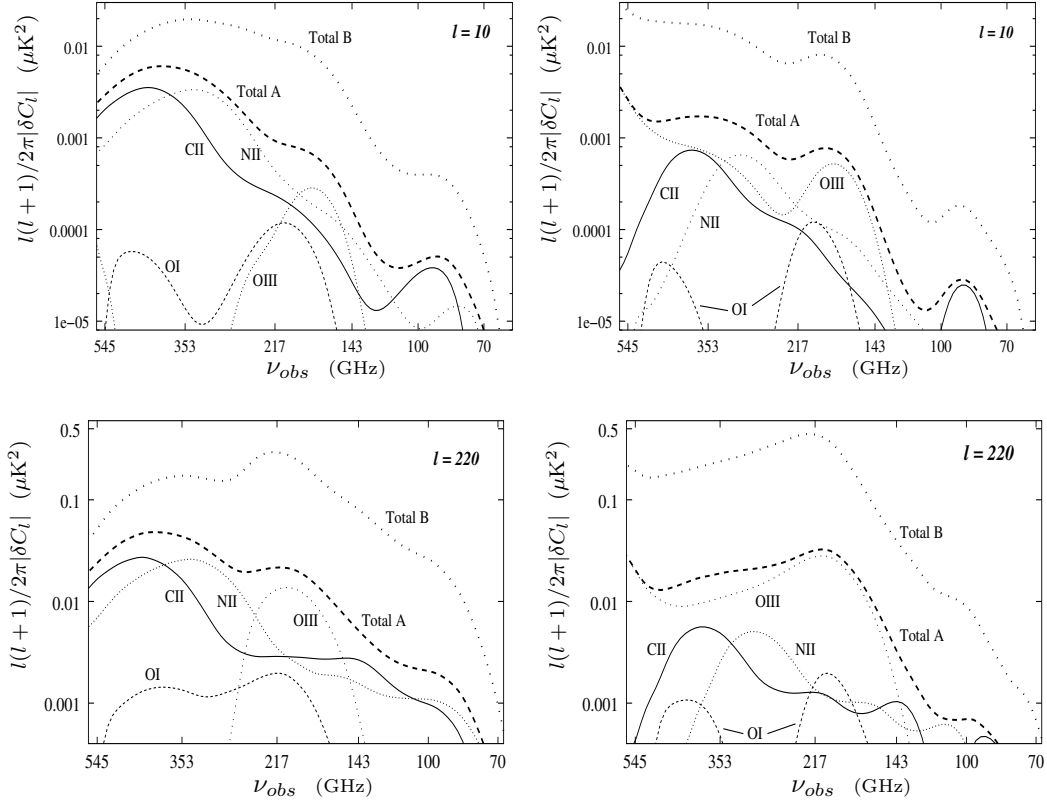
Figure 6.6: Temperature anisotropy generated by atomic and ionic fine structure lines at different frequencies in the case of two different angular scales of observation. The figures on *left* are for Case I of Fig.3, which is for reionization by stars unable to ionize OII. Figures on *right* are for Case II, which is for reionization by hot stars and quasars and hence have high OIII fraction. Each figure gives the total contribution for both history A and history B. However, the separate contributions from different lines are given for history A only. We present results for three angular scales: $l = 10$ (*above*) and $l = 220$ (first Doppler peak, in *below*). The scattering-generated $\delta C_l$-s that are proportional to the intrinsic $C_l$-s for higher multipoles, as can be clearly seen in comparison with Fig.(6.2).
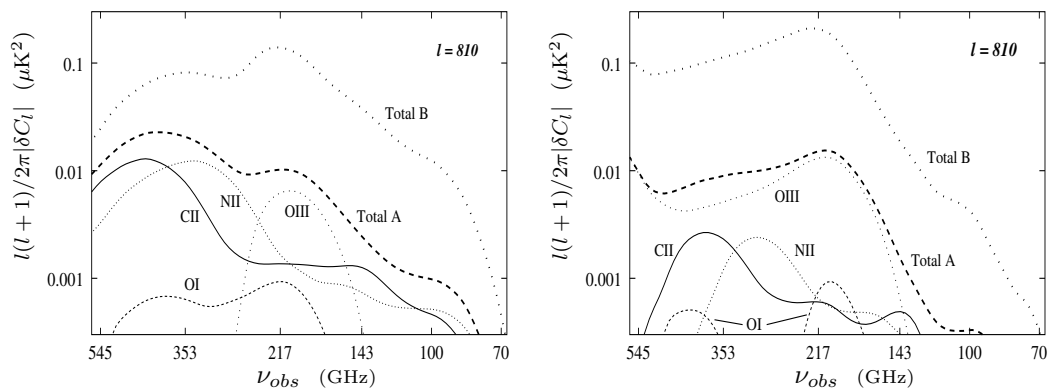
Figure 6.7: Same plot as before, but showing the results for $l = 810$ which is the position for the third Doppler peak in CMB power spectrum. The $\delta C_l$-s are again proportional to the intrinsic $C_l$-s, but magnitude is slightly less at the position of third peak because of the reduced power in primary spectrum from $l = 220$ to $l = 810$.

multipoles the effect is not proportional to $C_l$, as can be seen from the two panels at top. These low multipole results are important for future satellite missions like Planck and CMBPol. In the middle, results for $l = 220$ are shown, where effect is already proportional to $C_l$. The amplitude of the signal is highest here due to the large amplitude for the $C_l$ at the first Doppler peak. At the bottom we give results for the third Doppler peak, or $l = 810$, where signal drops by a factor of 2 from that of $l = 220$. However, these angular scales ($\theta \sim 13'$) are particularly suitable for future balloon and ground-based experiments with multi-channel narrow-band recievers.

### 6.1.1 Scenario for late reionization

Finally, in Fig.(6.8) and (6.9), we present an alternative ionization and enrichment history of the universe, when there were no production of heavy elements before $z \sim 12$. This is very interesting because, even for such late reionization, if there is moderate enrichment of the IGM around redshift $4-5$, we have the possibility to detect our signal with Planck HFI around $l = 10$. The contributions from high energy oxygen lines are reduced because of the absence of metals at high redshift, but long-wavelength lines of CII and NII still can generate strong signal from low redshifts ($z \lesssim 8$). The HFI sensitivities in this figure have again been improved by averaging the noise in a multipole range of $\Delta l = 10$ around $l = 10$. As discussed before, the signal for $l = 220$ and $l = 810$ are proportional to the optical depths in these lines and the primordial $C_l$-s.

Due to relatively small scattering cross-sections of the fine-structure transitions under discussion, such observations are sensitive to significant abundances of the atoms and ions (for example when given species contributes from 10% up to 100% of the corresponding element abundance), whereas the Gunn-Peterson effect gives optical depth of the order of unity already when abundance of neutral hydrogen is of the order of $10^{-5} - 10^{-6}$. Hence even if the universe is completely opaque

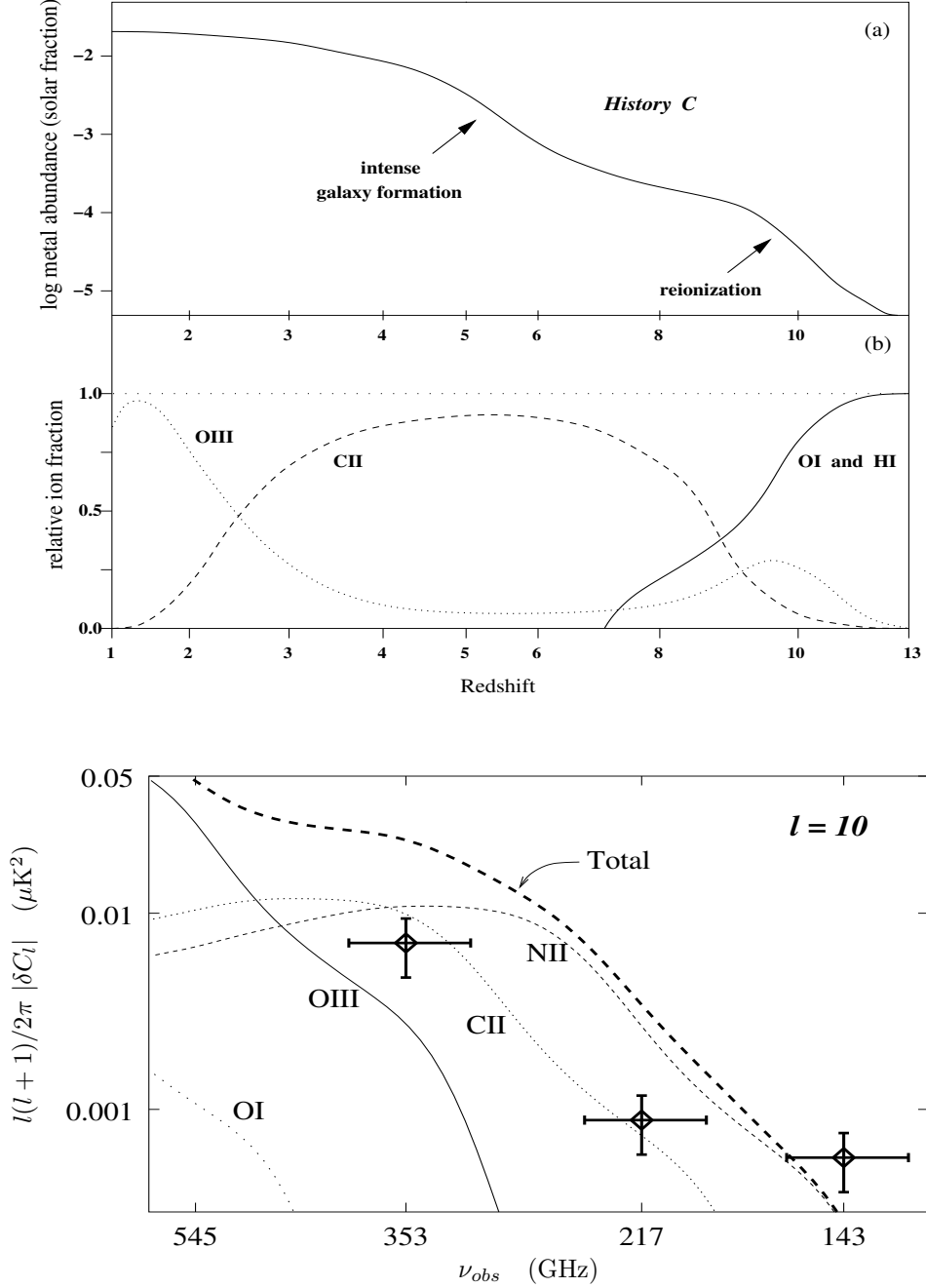Figure 6.8: Late ionization and enrichment history of the universe. *Top* Sketch for the abundance history with late reionization, where first metals are produced around $z \sim 10 - 12$. *Bottom* Temperature anisotropy for this abundance history generated at $l = 10$. Also shown are the Planck HFI sensitivity, where the noise levels have again been improved by $\sqrt{\Delta l}$ in the multipole range $10 - 20$.
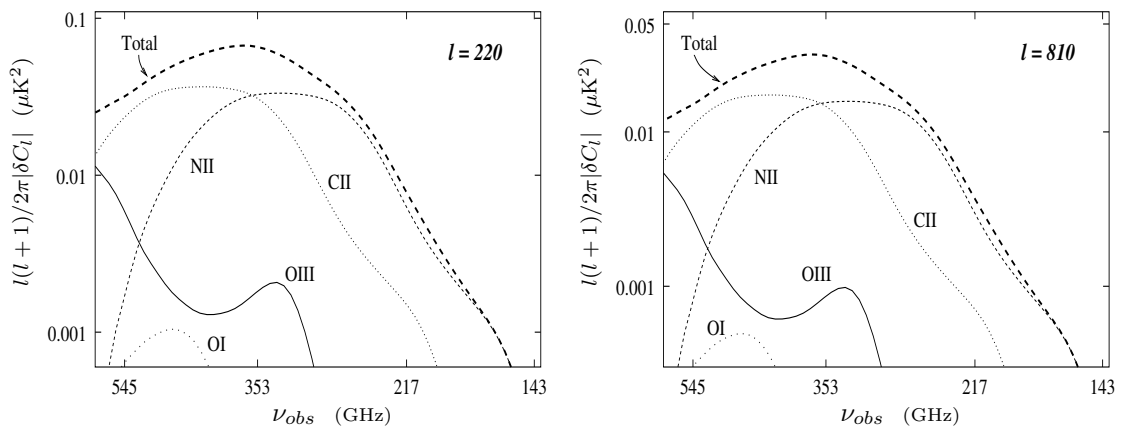
Figure 6.9: Late ionization and enrichment history of the universe, showing the temperature anisotropies at $l = 220$ *(left)* and $l = 810$ *(right)*, respectively.

to Ly-$\alpha$ photons at redshifts $z \gtrsim 6$, ionic fine-structure lines like CII $157.7\mu$ can probe the very first stages of patchy reionization process. Detection of all three broad spectral features connected with strongly redshifted OI, CII and OIII microwave lines will open the possibility to trace the complete reionization history of the Universe. In addition OIII line will proof the existence of extremely hot stars at that epoch.

The published level of noise of the Planck HFI shows that the three low frequency channels of HFI are almost an order of magnitude more sensitive than signal coming from cases I & II of history B. Even in the case of late reionization history (case C, Fig.6.8 ), Planck is about 4-times more sensitive than predicted signal. However, to be able to find contribution from at least three lines simultaneously we need higher amount of frequency channels than Planck HFI will have. A higher amount of frequency channels would certainly be possible for the next generation experiments like CMBPol even if they are based on already existing technology (Church 2002).

### 6.1.2 Significance of $\delta C_l$-s at small angular scales

There is the possibility that balloon and ground-based experiments will be able to check the level of enrichment of the universe by heavy elements even before Planck, observing at $l = 220$ and $l = 810$, for instance. At these high multipoles, effect is directly proportional to the optical depths in lines and the primordial CMB anisotropy. Hence using the data from Table(5.2) and Fig.(6.2), and the simple analytic relation $\delta C_l \simeq -2 \ \tau_{X_i} \ C_l^{primary}$, one can immediately give the effect in a first approximation. The high signal-to-noise ratio of the primordial $C_l$-s around the first three Doppler peaks will correspondingly give rise to strong signals in scattering, and might become accessible through the tremendous sensitivity promised from the forthcoming balloon and ground-based telescopes like Boomerang, ACT, APEX and SPT. Likewise, CBI, VSA and BIMA

intereforemeters are focusing their study at low frequencies, at which CI lines with wavelengths $609\mu$ and $370\mu$ might contribute to the observed signal.

CBI, VSA and BIMA interferometrs are studying successfully CMB angular fluctuations at low frequencies (30 GHz), and there are plans to continue observations on 45, 70, 90, 100 and 150 GHz. CI lines with wavelengths 609 and 370 $\mu$ coming from high redshifts ($z \sim$ 10-15) might contribute to the observed signal at low frequencies.

Beginning of the end of 60-ties theorists are discussing early star formation due to isothermal perturbations, making possible production of heavy elements at redshifts well above 100. This makes interesting the lines with much shorter wavelengths, like $12.8\mu$ Ne II line and many others, which might be contributing to the Planck HFI spectral bands even from redshifts $\sim$ 100.

# Chapter 7

# Emission from Denser Regions

## 7.1 Temperature anisotropies from emission

Recent computations of early star formation in the universe show that the regions which will later form cluster of galaxies are experiencing star formation much earlier than the future empty fields (Ciardi et al. 2003, Sokasian et al. 2004, Furlanetto et al. 2004). This shows that the merger tree knows already at rather high redshifts ($z \sim 15 - 20$) where the future cluster of galaxies will be. This numerical information opens a new way to study the process of reionization using the well known technique of Cosmic Microwave Background fluctuations. The first star formation occurs in the smallest scale objects which have the highest perturbation and mass of the order of $10^6 - 10^8$ $M_\odot$, and in simulations they are modeled in much larger scales, including the very important scale of future cluster of galaxies (Yoshida et al. 2002, Springel & Hernquist 2003). Let us remind that these scales correspond to a comoving size of $20h^{-1}$ Mpc. Strong dispersion in the time of first star formation, generation of ionizing photons, and production of chemical elements make these future cluster of galaxies very different in their surface brightness in the microwave bands. Numerical computations show that first such proto clusters might become bright already at redshift 17-20, but majority of them are really very bright in microwave bands when the bulk of star formation occurs around redshift 5. It is important for us that universe already at that redshift is separated into regions of high and low star formation. This inevitably would lead to the fluctuations of CMB, connected with well-known processes which contribute on different scales to the brightness of star forming regions of our and other nearby galaxies: bremsstrahlung radiation of dense ionized plasma, line emission from atoms and ions like $C^+$, and thermal radiation from low temperature dust. It is obvious that all these emission will come from very dense regions, but let us repeat that such radiation dense clouds are much more numerous in some parts of the universe (in regions of $20h^{-1}$ Mpc scale), and less numerous in regions where star formation is delayed or will not occur at all (e.g. in voids, or in regions where field galaxies will form much later).

# 7. EMISSION FROM DENSER REGIONS

In this chapter we will estimate the observed flux and surface brightness of the regions for proto-clusters and future cluster of galaxies, and then on simple assumptions we will try to find what is their contribution to the fluctuations in the microwave sky. It is very important to note that $C^+$ line emission (as well as other fine structure lines considered previously) from the regions enriched with heavy elements is spectrally narrow. Using different frequency channels of Planck spacecraft it might be possible to estimate the contributions to the angular fluctuations in the microwave background from proto clusters, where star formation is occurring at redshift interval $z \in [2, 20]$. The cold dust emission in our Galaxy and other nearby galaxies also have spectrum which drops rapidly in longer wavelengths. This also opens the way of differential broad-band spectroscopy, because only certain redshift intervals will contribute to any specific Planck channel, and other redshifts will not.

To compute the angular fluctuations we will adopt the following simple model. We will assume that the regions of intense star formation are very rare at higher redshifts, and their numbers are increasing, and have maxima at $z \sim 5.4$, according to the star formation history presented by Springel & Hernquist (2003). This history reflects the low mass long-lived star population, however for our purpose we are more interested in the massive ($> 8M_\odot$) star population at all redshifts which are the most efficient producer of UV photons. This we obtain by extrapolating the Initial Mass Function (IMF) into the low mass end assuming the simple Salpeter IMF (Salpeter 1955), which results into a renormalization of the star-formtation history. We use this global star formation rate to estimate the amount of massive stars formed inside halos of specific mass range, and estimate their luminosity in dust or $C^+$ line emission using the observed correlation of SFR-Luminosity in nearby star forming galaxies. This approach obviously gives the upper limit in line or dust emission, since this uses the metallicity or dust-to-gas ratio inside the halos to be the same as in local universe. But we see that even with solar abundance at high redshifts, the correlation signal from line emission is at best of similar magnitude to the scattering signal discussed in the thesis, and the reason for the smallness of the emission signal is the absence of any "suppression" term at high $l$-s, as well as from the lack of velocity dependence in the correlation part. We discuss these points in detail later.

In this final chapter we discuss the method of computation for the temperature fluctuations due to line emission from star-forming halos. We demonstrate only the case for $C^+$ $157.7\mu$ fine-structure line, but the formalism developed below using the correlation between star-formation and brightness temperature of an object is applicable for any line, as well as for the dust emission. The redshift of line emission is chosen to be around $z = 10$.

## 7.2 Correlation Between the SFR and Total Luminosity

In this section we try to formulate simple correlations between star formation rate inside halos and their total luminosity in far-IR lines or dust. This luminosity is then converted to the observed flux (when the halo is unresolved) or brightness temperature which can be used to compute the angular distribution of the sky intensity at the relevant frequencies.

### 7.2.1 Star Formation Rate Inside the Halos

The star formation history of the universe is obtained from the well-known Madau plot (Madau et al. 1996, 1998), which gives the amount of newly formed stars (in $M_\odot$) per year per unit co-moving volume of the universe. At high redshifts ($z \gtrsim 3$) we must rely on numerical simulations of the star formation history for extending the Madau plot upto high redshifts ($z \gtrsim 20$), as has been used, for example, by Barkana & Loeb (2000). In the present analysis we use the recent high-resolution simulations of the star formation history of the universe by Springel & Hernquist (2003), who have obtained a semi-analytic fit to the global star formation history

$$\dot{\rho}_\star(z) \;=\; 0.15 \text{ M}_\odot \text{yr}^{-1} \text{Mpc}^{-3} \; \left[ \frac{b \exp\left[a(z - z_m)\right]}{b - a \exp\left[b(z - z_m)\right]} \right] \tag{7.1}$$

with $a = 3/5$, $b = 14/15$ and the peak of star formation at $z_m = 5.4$. This is, however, the integrated star formation rate over all halo masses, and we need the star formation rate inside the halo of a specific mass. One way of obtaining it would be to assume the normalized star formation rate (star formation rate inside a halo per unit halo mass) to have a shape like step-function, which becomes zero below some critical halo mass (Hernquist & Springel 2003). In such approximation we can apply the Press-Schechter formalism to obtain the star formation rate (SFR) for a halo of mass $M_{halo}$ as

$$\dot{M}_\star \;=\; \frac{M_{halo} \; \dot{\rho}_\star(z)}{\bar{\rho} \; \left[F(\infty, z) - F(M_4, z)\right]} \tag{7.2}$$

Here $\bar{\rho}$ is the comoving background density of the universe, and $F(M, z)$ denotes the fraction of mass that is bound at epoch $z$ in halos of mass *smaller* than M. $M_4$ corresponds to virial temperature of $T_{vir} = 10^4$K (which is assumed to be the threshold halo mass to have star formation), and can be computed from the following formula $T_{vir}(M, z) = 9.5 \times 10^7 K \; [(1 + z)^3 \Omega_m + \Omega_\Lambda]^{\frac{1}{3}} (M_{halo}/10^{15} h^{-1} M_\odot)^{\frac{2}{3}}$ for a flat universe.

This star formation rate corresponds to the rate at which long-lived stars form, which have masses $\lesssim 8$ M$_\odot$. As we will see in the next section, the dust or far-IR line luminosity inside a galaxy corresponds to the rate of new-born *massive* stars, which have masses 8 M$_\odot$ or higher and produce the bulk of ionizing UV photons. These stars have a lifetime $\lesssim 3 \times 10^7$ years, which is much shorter than the cosmological timescale at the redshifts of interest. Hence the slope of the

total star-formation rate, and the luminosity function inside the halos, critically depends on this high-mass end of the star formation history. We must employ an additional normalization factor to the above star formation rate (eqn.7.2), which will correspond to the massive star formation rate inside the halo.

We do this by simply assuming a universal initial mass function (IMF) of Salpeter (1955) with a slope of $-1.35$ in the mass range $0.1 - 40$ M$_\odot$. The star formation rate given in eqn.(7.2) corresponds to stars with masses below 8 M$_\odot$, hence we should multiply it with the correction factor

$$f(> 8\text{M}_\odot) \;=\; \frac{\int\limits_{8}^{40} \mathcal{F}(M)dM}{\int\limits_{0.1}^{8} \mathcal{F}(M)dM} \;\simeq\; 0.12 \tag{7.3}$$

where $\mathcal{F}(M) \propto M^{-1.35}$. Hence the mass of the massive stars, which are the dominant producer of UV photons, is about 12% of the long-lived stars of smaller mass. Therefore to obtain the luminosity of a halo from its star formation rate, we must put this correction factor to the SFR obtained from the Madau plot, or in our case the global star formation history of Springel & Hernquist (2003).

## 7.2.2 Luminosity-SFR Relations in Galaxies

The star formation rate indicators inside a galaxy connected with its total luminosity can have many uncertainties, as it will depend on the metallicity, dust content, and the shape of the IMF. However we shall not go into a detailed study of these relations, and simply assume the most well-known calibrations in use for the local universe. Kennicutt (1998) formulate the following star formation rate indicators from the bolometric luminosities of galaxies

$$\dot{M}_* \text{ (M}_\odot \text{ yr}^{-1}) = 1.1 \times 10^{-41} \; L_{H\alpha} \text{ (erg s}^{-1}) \tag{7.4}$$

$$\dot{M}_* \text{ (M}_\odot \text{ yr}^{-1}) = 4.5 \times 10^{-44} \; L_{FIR} \text{ (erg s}^{-1}) \tag{7.5}$$

There relations refer to star formation in stars more massive than $\sim 5$ M$_\odot$, and we are mostly interested in stars above 8 M$_\odot$ which have life-time $\lesssim 3 \times 10^7$ years and explode as supernovae after that time scale. However, the SFR correction from $M > 5$ to $M > 8$ solar masses is relatively small, of the order of 20% (Grimm et al. 2003), which we can ignore in our modeling. Also, the above relations are based on the average properties of star forming galaxies, and there is considerable scatter in any correlation. We shall return to these issues when we describe the individual correlations with the spectral luminosities of dust or the lines with star formation rate, but before that we discuss the necessary formulation of observed flux and brightness temperature.

### 7.2.3 The Observed Flux and Brightness Temperature

We give here the definitions of observed flux and brightness temperatures that we shall be using subsequently. For details, any standard text on cosmology can be consulted, e.g. Padmanabhan (2002).

The bolometric flux observed from a source at redshift $z$ is given by

$$F_{bol} \; = \; \frac{L_{bol}}{4\pi d_L^2} \qquad \text{erg s}^{-1} \text{ cm}^{-2} \tag{7.6}$$

where $d_L$ is the luminosity-distance of the object at redshift $z$

$$d_L = \frac{c}{H_0} \; (1+z) \; \int_0^z \frac{dz}{\sqrt{(1+z)^2(1+\Omega_M z) \; - \; z(2+z)\Omega_\Lambda}} \tag{7.7}$$

However, we are more interested in the observed *flux density* for any frequency-dependent emission. For a power-law emission with spectral luminosity $L_\nu \propto \nu^{-\alpha}$, we have the observed flux density, or simply *flux*, given by

$$F_\nu(\nu_{obs}) \; = \; \frac{L_\nu(\nu_{obs})}{4\pi d_L^2 \; (1+z)^{\alpha-1}} \qquad \text{erg s}^{-1} \text{ cm}^{-2} \text{ Hz}^{-1} \tag{7.8}$$

For example, for dust emission with a $\nu^{1.5}$ emissivity law, we have $\alpha = -3.5$ in the R-J limits.

For line emission, we can obtain the spectral luminosity at the line center approximately by dividing the total luminosity with the line width: $L_\nu \approx L_{bol}/\Delta\nu$ (erg s$^{-1}$ Hz$^{-1}$). Now remembering that $\Delta\nu = (\Delta v_{th}/c)\nu$, and the scaling between observed and emitted frequency $\nu_{obs} = \nu_{em}/(1+z)$, we immediately obtain

$$F_\nu(\nu_{obs}) \; \approx \; \frac{L_{bol}}{4\pi d_L^2 (1+z) \; \Delta\nu_{obs}} \qquad \text{erg s}^{-1} \text{ cm}^{-2} \text{ Hz}^{-1} \tag{7.9}$$

For a more accurate treatment we must integrate over the line profile, which can be assumed to be a Gaussian with line-width $\Delta\nu$. With the above definition of flux, we can finally write the expression for *mean intensity*, $J_\nu \; = \; F_\nu/4\pi$ (erg s$^{-1}$ cm$^{-2}$ Hz$^{-1}$ sr$^{-1}$), which is the quantity that can be compared with the mean background intensity of the CMB photons ($B_\nu$) to obtain the change in brightness temperature due to emission

$$\Delta T_b \; = \; T_0 \, \frac{e^x - 1}{xe^x} \, \left(\frac{\Delta J_\nu}{B_\nu}\right) \; \approx \; \frac{c^2}{2k\nu^2} \, \Delta J_\nu \quad \text{(in the R-J limit)} \tag{7.10}$$

Here both $J_\nu$ and $B_\nu$ are at $\nu_{obs}$, and we have used the usual dimensionless frequency $x \equiv h\nu_{obs}/kT_0$ with $T_0 = 2.726$ K as the present-day CMB temperature.

In case it is necessary to compute the brightness temperature of an object *in situ*, i.e. in the comoving frame of emission, then one must assume some definite size of the emitting halo. Given the radius $R$ of the object, the mean intensity will be simply

$$J_\nu(\nu_{em}) \; = \; \frac{L_\nu}{4\pi \cdot 4\pi R^2} \qquad \text{erg s}^{-1} \text{ cm}^{-2} \text{ Hz}^{-1} \text{ sr}^{-1} \tag{7.11}$$

which should be compared with the intensity of CMB photons at the emitting redshift to obtain the brightness temperature of the halo. In the subsequent computation we shall assume $R$ to be equal to the virial radius, or 1/10th of the virial radius, of the halo.

## 7.3 Modeling the line emission

In this section we show how we model the line and dust emission from star formation rate inside galaxies. All these correlations are taken from existing literature, we merely apply the appropriate normalization for massive star formation within halos, and rearrange or re-group them to find the luminosity which interests us. All the references are cited in individual sections.

### 7.3.1 Emission from C$^+$ fine-structure line

The CII 158$\mu$ FS line is the most extensively studied FIR line that has been used as a star-formation tracer in galaxies, and it the dominant coolant of inter-steller gas. This radiation is generated both in diffuse inter-stellar medium, and in photo-dissociation regions, at the interface between molecular clouds and HII regions. The photo-ionizing radiation is dominated by B3 and B0 stars with $5 \leq M \leq 20$ M$_\odot$ (e.g. Xu et al. 1994), but of course hotter and more massive stars contribute. However, the intensity in CII line can in a galaxy not be expected to be directly proportional to the star formation rate, mainly because of the variety of the line sources and their physical condition. Also the excitation of the upper fine-structure level of CII fine-structure doublet saturates at high temperatures and high densities (e.g. see Kaufman et al. 1999). However the emission in this line is strong, and future sum-mm and far-IR experiments like ALMA and Herschell will be able to pick up galaxies in the CII line easily in wide range of redshifts.

To find the brightness temperature from the emission of CII line in a star-forming halo of mass $M_{halo}$ at redshift $z$, we start with the correlation between total CII luminosity of a galaxy and its star formation rate, $\dot{M}_*$ (Boselli, Gavazzi, Lequeux et al. 2002)

$$\dot{M}_* = 5.953 \times 10^{-33} \ \times \ 10^{0.8 \times \log L_{CII}} \quad \text{M}_\odot \ \text{yr}^{-1} \tag{7.12}$$

which gives

$$\log L_{CII} = 1.25 \left[ \log \dot{M}_* \ + \ 32.225 \right] \tag{7.13}$$

The slightly non-linear correlation given above is also supported by the observations from Stacey et al. 1991. This CII luminosity (in erg s$^{-1}$) is integrated over the entire line profile. To convert it into spectral luminosity at the line center, we divide it by the line-width, $L_\nu \approx L_{CII}/\Delta\nu$. This spectral luminosity is then converted to the brightness temperature with the standard formalism for conversion between flux and temperature.

### 7.3.2 Emission from dust

Although we shall not be presenting the results for temperature fluctuations due to dust emission, we show below that the dust emission from a halo can be correlated with its star formation rate in a similar manner. The correlation between the total FIR emission and star-formation rate is well established. From Kennicutt 1998, we have for starburst galaxies

$$\dot{M}_* \ (\mathrm{M_\odot \ yr^{-1}}) = 4.5 \times 10^{-44} \ L_{FIR} \ (\mathrm{erg \ s^{-1}}) \tag{7.14}$$

Here $L_{FIR}$ refers to the full integrated IR luminosity in the $8 - 1000\mu$ range. However, most of this emission comes from the wavelength range $20 - 200\mu$, with the peak of emission near $100\mu$, and hence the spectral luminosity of dust at $100\mu$ shows good correlation with the star-formation rate (Buat & Xu 1996, Misiriotis et al. 2004)

$$\log L_{100} \ = \ 29.03 + \log \dot{M}_* \tag{7.15}$$

where $L_{100}$ is the spectral luminosity (in ergs s$^{-1}$ Hz$^{-1}$ sr$^{-1}$) for the dust spectrum at $100\mu$. The advantage of this formulation is that $L_{100}$ is a directly observable quantity, and we need no detailed dust SED modeling and dependence on dust temperature.

For *broad-band CMB experiments like PLANCK*, the flux incident in each frequency channels will be the integrated flux over a band-width $\Delta\nu \approx 0.25\nu$. In such case the detailed modeling of dust SED is necessary. In star-forming galaxies like M 82, the dust SED is modeled with a $\nu^{1.5}$ emissivity law

$$F_\nu = (\mathrm{const.}) \ \nu^{1.5} \ B_\nu(T_d) \tag{7.16}$$

We try to use this relation, normalized with the $100\mu$ flux from eqn.(7.15) to get the SED for dust emission. Our modeling is based on the observations of Colbert et al. (1999). As the first approximation, we again model the spectrum of the star-forming galaxy M 82, and assume that similar spectrum will be obtained from halos at all redshifts. Surely this will give us an upper limit on the contribution from dust emission. Under such assumption, the formula for the observed flux density from dust emission becomes

$$F_\nu^{\mathrm{obs}} = 8.22 \ \left(\frac{L_{100}}{D_L^2}\right) \ \left[\frac{\nu_{obs}(1+z)}{3 \times 10^{12} \ \mathrm{Hz}}\right]^{4.5} \ \left[\exp\left(\frac{h\nu_{obs}(1+z)}{kT_d}\right) - 1\right]^{-1} \tag{7.17}$$

in ergs s$^{-1}$ cm$^{-2}$ Hz$^{-1}$, where $\nu_{obs}$ is the observing frequency, $\nu_{obs} = \nu_{em}(1+z)$, and $D_L$ is the luminosity distance (in cm). Integrating this flux we immediately get the dust contribution in each broad-band observing channel.

The correlation between the IR-luminosity and dust temperature is very weak, as shown by Blain, 1999. He has given a simple relation between bolometric luminosity and $T_d$ for luminous infrared galaxies for the same emissivity index $\beta = 1.5$ and a single population of isothermal dust

$$T_d/\mathrm{K} \simeq 40 \left(L_{FIR}/10^{10}\mathrm{L_\odot}\right)^{0.03} \tag{7.18}$$

For further correction, we should extrapolate the dust temperature at high redshifts taking into account the increased CMB temperature, to get appropriate dust temperature at that redshift. This can be done approximately by using the relation

$$T_d(z) = \left[ T_d^{4+\beta} + T_{CMB}^{4+\beta} \left( (1+z)^{4+\beta} - 1 \right) \right]^{1/(4+\beta)} \qquad (7.19)$$

where $T_{CMB}$ is today's CMB temperature.

## 7.4  Computation of the Power Spectrum

We now proceed to compute temperature fluctuations arising from the non-uniform distribution of the emitting sources, as well as the component resulting from the non-zero correlation of density fluctuations with the last scattering surface. We divide this section into two parts: in the first part we describe the standard techniques of computing the power spectrum, using the number density of halos prescribed by hierarchical model of structure formation, resulting into temperature fluctuations which has a Poissonian component and a halo-halo correlation component. In the second part we try to wstimate the effect of correlation of density perturbations at the emitting redshift with that of in the last scattering surface. This part uses a line-of-sight integration approach, using the CMBFAST code, and has been done in collaboration with C.Hernández-Monteagudo.

### 7.4.1  Poisson (shot noise) and the 2-point correlation components

In order to copute the power spectrum due to non-uniform distribution of the sources and due to clustering between the sources, we use the formulation from Komatsu & Kitayama (1999), assuming some definite size of the emissting objects. This is because the power spectrum is computed *in situ* by adding the $\Delta T_b(M, z)$ from many halos into the comoving volume at redshift $z$, whose radial extent is determined by the instrument's frequency resolution. To convert the spectral luminosity of a resolved halo into flux, and hence the brightness temperature, we must assume some size of the emitting source. For a rough estimate, we assume the size to be a fixed 10% of the virial radial of the halo, where the virial radius is defined as

$$R_{vir} = \frac{G\mu M_{halo}}{3kT_{vir}} \qquad (7.20)$$

where $\mu \approx 0.6m_p$ is the mean molecular weight, and we have dependence of virial temperature of the halo on its mass and redshift $z$ as

$$T_{vir} = 9.5 \times 10^7 \mathrm{K} \left( \frac{M_{halo}}{10^{15}h^{-1}\mathrm{M_\odot}} \right)^{\frac{2}{3}} \left( \frac{H(z)}{H_0} \right)^{\frac{2}{3}} \qquad (7.21)$$

The change in intensity is obtained by dividing the spectral luminosity by the total surface area of the source, and averaging over all solid angles

$$\Delta I_\nu \approx \frac{L_\nu}{4\pi \cdot 4\pi R^2} \quad \text{erg s}^{-1} \text{ cm}^{-2} \text{ Hz}^{-1} \text{ sr}^{-1} \tag{7.22}$$

which gives

$$\Delta T(M,z) = T_\gamma \, \frac{c^2}{2h\nu^3} \, \frac{(e^x - 1)^2}{xe^x} \, \Delta I_\nu \tag{7.23}$$

with $T_\gamma = 2.726(1+z)$ as the CMB temperature at redshift $z$, $x \equiv h\nu/kT_\gamma$. Below we show results for the C$^+$ line only, with $\nu = 1.9$ THz, and at redshift $z = 10$ with $\Delta z = 0.25z$.

The power spectrum arising from the number fluctuation of unresolved sources is well established. Following Cole & Kaiser (1988), the expression for $C_l$-s due to Poisson distributed sources is

$$C_l^{Poisson} = \int dz \, \frac{dV}{dzd\Omega} \, \int_{M_4}^{M_{max}} dM \, \frac{dn}{dM}(M,z) \, |T_l(M,z)|^2 \tag{7.24}$$

Here $dV$ is the comoving volume element at redshift $z$, and the quantity $dV/dzd\Omega$ can be expressed simply in terms of the angular diameter distance $d_A = d_L/(1+z)^2$ as

$$\frac{dV}{dzd\Omega} = d_A^2 \, c\frac{dt}{dz} \tag{7.25}$$

$\Delta T_l$ is the angular Fourier transform of $\Delta T(\theta)$. For the brightness temperature, eqn.(7.23) is used, which corresponds to the temperature in *real* space with a definite angular size $\theta_h \approx R_{vir}/d_A$. Hence the temperature in *Fourier* space for a particular multipole $l$ is obtained by convolving the real-space temperature with the angular area of the halo

$$\Delta T_l(M,z) = \Delta T_\theta(M,z) \, \left(2\pi\theta_h^2\right) \, \exp\left[-\frac{l(l+1)}{2}\frac{\theta_h^2}{2}\right] \tag{7.26}$$

We see that $C_l^P \propto |\Delta T_l|^2 \propto \theta_h^4$, and is constant for $l \ll l_h$ where $l_h = \pi/\theta_h$. This coefficient explains the smallness of $C_l$-s at large angles, since we have typically $R_{vir} \sim 3$ kpc for a star-forming halo, which at $z = 10$ corresponds to $\theta_h \sim 10^{-6}$ radians.

The other important part of the Poissonian component is the number count of the objects, $dn/dM$ at redshift $z$. To estimate the comoving number density of the halos, we employ the standard Press-Schechter formalism (Press & Schechter 1974)

$$\frac{dn}{dM} = \sqrt{\frac{2}{\pi}} \, \frac{\bar\rho}{M} \, \frac{\delta_c}{D(z)} \, \left|\frac{1}{\sigma^2(M)}\frac{d\sigma(M)}{dM}\right| \times \exp\left[-\frac{\delta_c^2}{2\sigma^2(M)D^2(z)}\right] \tag{7.27}$$

Here $\bar\rho$ is mean comoving matter density of the universe, $\delta_c$ is the overdensity threshold, $D(z)$ is the linear theory growth function of density perturbations, and $\sigma(M)$ is the variance of the density field smoothed with mass scale M. We have used $\sigma(M,z) = \sigma(M)D(z)$. This number density incorporates em all halos per unit mass range per comoving volume, but we are interested only in
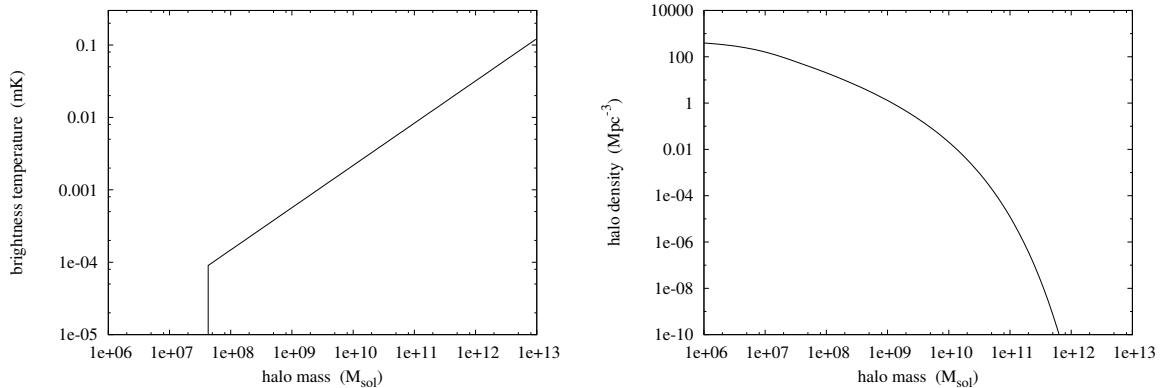
Figure 7.1: Brightness temperature and number density of star-forming (recently merged) halos at $z = 10$. In *left*, we show the brightness temperature (in mK) of star-forming halos in the $C^+$ line, following the correlation derived in eqn.(7.13). The temperature grows linearly with mass because we assumed the star formation rate inside halos is directly proportional to its mass. The sharp cut-off around $5 \times 10^7$ M$_\odot$ is due to the assumption that no halos below virial temperature $10^4$ K is able to form stars. In reality there will be a smooth transition around this cut-off. In *right* we show the number density of recently merged halos at $z = 10$, following the formulation of Sasaki (eqn.7.28) and Press-Schechter number count. The resulting $C_l$-s are product of these two quantities.

those halos which are having star formation at any given time. We assume the formation rate of massive stars are proportional to the merger rate of the halos, where the later quantity is given by Sasaki (1994)

$$\frac{d}{dt}\left(\frac{dn_{merg}}{dM}\right) = \frac{1}{D}\frac{dD}{dt}\frac{dn}{dM}\frac{\delta_c^2}{\sigma^2(M)D^2(z)} \tag{7.28}$$

where symbols have the same meaning as before. This we multiply by the average life-time of massive stars, $\Delta t = 10^7$ years, to get the amount of starburst that is actually going on at any given redshift. This is the quantity that we use in eqn.(7.24).

The mass integration is done over halos of all masses that can form stars. We choose $M_{max} = 10^{15}$ M$_\odot$ as the maximum mass for star forming halos, and for the lower mass limit we use $M_4$, which corresponds to halos with virial temperature $T_{vir} = 10^4$K at that redshift. Below this limit we assume no star formation inside the halo, following Springel & Hernquist (2003), although this is a crude approximation which might under estimate the contribution from low-mass halos. The contribution from very massive halos of masses $M_{halo} > 10^{12}$ M$_\odot$ into the power spectrum is very small due to the rarity of these objects.

In addition to the Poisson term, there would be additional clustering term in the power spectrum due to halo-halo correlation. At large angular scales the contribution from the clustering term may be significant over the Poisson term. For this part we follow the formulation of Komatsu &

Kitayama (1999), who used this expression

$$C_l = \int dz \; \frac{dV}{dzd\Omega} P\left(k = \frac{l}{r(z)}\right) \left[\int_{M_4}^{M_{max}} dM \; \frac{dn}{dM}(M, z) \; D(z)\tilde{b}(M, z) \; T_l(M, z)\right]^2 \qquad (7.29)$$

$P(k, z)$ is the linear theory power spectrum, and we have used the Limber approximation $k = l/r(z)$, where $r(z) = d_A(1 + z)$ is the comoving distance or proper motion distance. The clustering power spectrum relates to the matter power spectrum $P(k, z)$ through the time-independent bias, $b(M, z)$, whose analytic expression is given by Mo & White (1996). However, following Oh et al. (2003), we use the mass weighted bias for our computation, given by

$$\tilde{b}(M, z) = \int_{M_4}^{M_{max}} dM \frac{dn}{dM} \; M \; b(M, z) \left/ \int_{M_4}^{M_{max}} dM \frac{dn}{dM} \; M \right. \qquad (7.30)$$

which corresponds to flux-weighted bias since we assume $F_\nu \propto M_{halo}$. The lower limit of halo mass is again chosen to be equal to halos with virial temperature $10^4$K at that redshift, below which we assume no star formation.

The results for such computations are shown in Fig.(7.2). The shape of these power spectra are weakly dependent on the size of the sources, and fairly well determined., but their amplitudes are somewhat more uncertain. The relative amplitude of the Poisson and clustering terms depends on the thickness of the redshift interval, $\Delta z$, sampled by the frequency resolution of the instrument, and we have used parameters similar to a broad-band instrument like PLANCK HFI with 25% bandwidth. Also the amplitude of the power spectrum is very sensitive to the halo mass-function, $dn/dM$ in the low mass range, i.e. on the lower cut-off in our mass integration.

These computations show that even assuming solar abundance of the emitting species, i.e. taking the same SFR-luminosity correlation as in the local universe, the amplitude of the emission term is several orders of magnitude lower than the scattering term arising from the same $C^+$ line. However the reason for the high amplitude of the scattering signal discussed in this thesis is a non-zero correlation between the density fluctuations at the epoch of scattering/emission and that in the last scattering surface, which resulted in $C_l \propto \tau_\nu$ at large angles. We must check whether there is any boost in the emission power spectrum at low $l$-s from such correlation. This is done next where we employ a line-of-sight approach for computing temperature fluctuations in accordance to the one used in scattering.

## 7.4.2 Effect of correlation with the CMB

In order to compute the correlation between the $C^+$ line emission and the CMB, we must express the emission as a function of the linear density field. This is because the correlation existing between
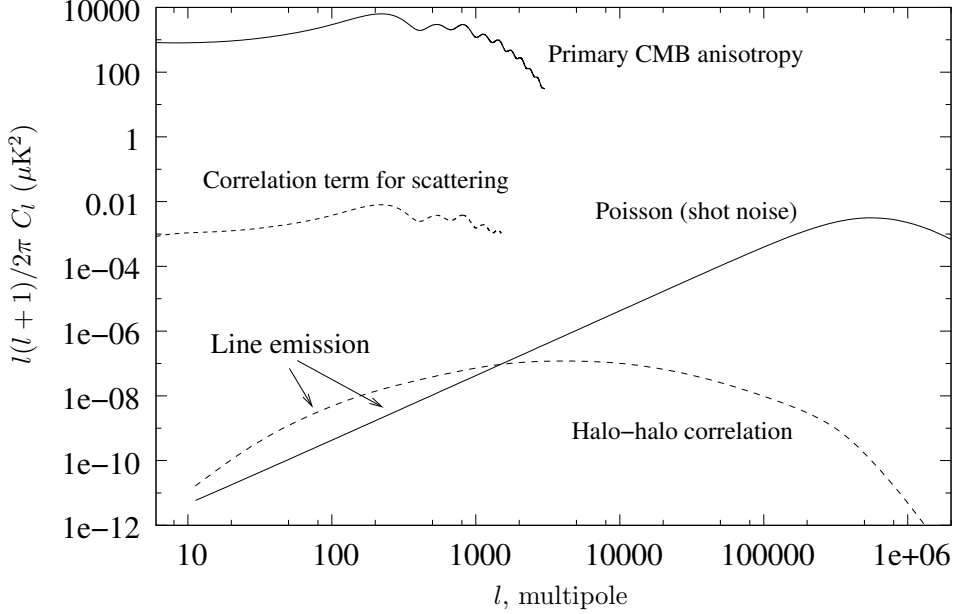
Figure 7.2: Figure showing the temperature fluctuations generated by emission in the $C^+$ $157.7\mu$ FS line, *without* any correlation with the density perturbations with the LSS. Observing frequency is 170 GHz, for which the contribution of $C^+$ line comes from redshifts around $z = 10$, and we have chosen a frequency resolution $\Delta\nu/\nu = 0.25$. The Poisson $C_l$-s are constant upto a very high $l$ which roughly corresponds to the size of the objects, which we took as 10% of the virial radius. This plot shows that without any correlation with the density fluctuations in the LSS, which were responsible for the high amplitude of the scattering signal (shown in figure), the emission contribution is negligible even with solar abundance of the metals.

CMB temperature anisotropies and $C^+$ emission resides in the fact that the halo population trace, in the large scales, the cosmological density field. We use the halo bias factor $b_h$ relating the density fluctuation field with that of the halo (Cooray 2001), and write the mass of newly formed stars inside the halo as the following

$$M_\star = f_{\text{eff}} \, \rho_b \, b_h \, \delta(\vec{r}) \, V_{halo} \tag{7.31}$$

Here $f_{\text{eff}}$ is the fraction of the baryonic mass of the halo that goes into massive stars, which we assume to be 0.01. $\rho_b$ is the mean baryon density of the universe, and $\delta(\vec{r})$ denotes the linear over-density at the point $\vec{r}$. The halo bias $b_h$ relates the cosmological density contrast $\delta$ with the density contrast *inside* the halo, and its value is close to $18\pi^2$. From the previous analysis of empirical correlation between the star formation and luminosity of the halo, which is roughly linear, we can write $L_\nu = A \, (M_\star/\Delta t_\star)$, where $A$ is a constant. Therefore we have the volume emissivity for any given point

$$j_\nu(\vec{r}) \;\approx\; \frac{A}{4\pi\Delta t_\star} \, f_{\text{eff}} \, \rho_b \, b_h \, \delta(\vec{r}) \tag{7.32}$$

Having this relation we can compute the change in intensity along the line-of-sight by integrating the volume emissivity through the halo, which gives

$$\Delta I_\nu = \int_{halo} j_\nu ds \approx \frac{A}{4\pi\Delta t_\star} f_{\text{eff}} \rho_b b_h \delta(\vec{r}) 2R_{vir} \tag{7.33}$$

The constant $A$ relates the luminosity of the halo to its star formation rate, according to $L_\nu = A (M_\star/\Delta t_\star)$, for which we derived the empirical relations previously. The factor $\Delta t_\star \sim 10^7$ years comes from using $\dot{M}_\star = M_\star/\Delta t_\star$, so that only the recently merged halos contribute, although we shall see that results are independent of $\Delta t_\star$.

From this, we can compute the relative change in brightness along the line-of-sight by comparing the above result with the CMB intensity at that redshift

$$\frac{\Delta I_\nu}{B_\nu(T_{rad})}[M,z] = \frac{A/(4\pi\Delta t_*) f_{\text{eff}} \rho_b b_h \delta 2R_{vir}(M,z)}{2\frac{(kT_0)^3}{(hc)^2} \frac{x^3}{e^x - 1} (1+z)^3} \tag{7.34}$$

where $T_{rad} \equiv T_0(1+z)$ and $T_0 = 2.726$ K. $x$ is the dimension-less frequency, $x \equiv h\nu/kT_{rad}$. Therefore, the brightness change for a single halo of mass M at redshift $z$ is an integral along the line of sight intersected by the halo, and has an $\propto 1/(1+z)^3$ dependence. We remind that $\nu_{obs} = \nu/(1+z)$, with $\nu = 1.9$ THz for the C$^+$ line.

However, when computing the contribution of the halo population by means of an integral along the line of sight, we shall proceed as in Hernández–Monteagudo & Sunyaev (2004a), where the following formalism is detailed. The $k$-mode of the temperature fluctuation $\frac{\delta T}{T_0}$ can be expanded onto a basis of Legendre polynomia,

$$\Delta(\mathbf{k},\eta) = \sum_l (-i)^l (2l+1) P_l(\mu) \Delta_l(k,\eta), \tag{7.35}$$

with $\mu$ the cosine given by the scalar product of the unitary vectors of $\mathbf{k}$ and the direction of observation, $\mathbf{n}$ (see, e.g., Hernández–Monteagudo & Sunyaev 2004b); and the multipoles $\Delta_l$ are given by an integral along the line of sight:

$$\Delta_l(k,\eta_0) = \int_{\eta_{dec}}^{\eta_0} d\eta j_l[k(\eta_0 - \eta)] S(k,\eta) \tag{7.36}$$

$\eta$ denotes conformal time, and it is equivalent to comoving distance. The source function $S(k,\eta)$, for this case, can be written as

$$S^{CII}(k,\eta) = \int_{M_4} dM \frac{\left(\frac{dn_{merg}}{dM} \tilde{j}_\nu(k,M) \tilde{W}_h(k)\right)}{B_\nu^{CMB}(\eta)} \tag{7.37}$$

In this equation, the lower limit of the mass integral is given by $M_4$, which is the mass corresponding to a virial temperature to $10^4$ K. The quantity $\tilde{j}_\nu(k,M)\frac{dn_{merg}}{dM}$ is the Fourier transform of $j_\nu \cdot$

93

$\frac{dn_{merg}}{dM}$, i.e., the emissivity within haloes times the number density per unit mass of recently formed haloes. This product is, a priori, a position dependent quantity, since it depends on the spatial distribution of the haloes. We are taking $\frac{dn_{merg}}{dM}$ from the model of Sasaki (1994) as before

$$\frac{dn_{merg}}{dM} = \dot{N}_{form}(M, \eta) \times \Delta t_{\star} \tag{7.38}$$

That is, we are looking at those haloes which have formed as a result of mergers in the last time interval given by $\Delta t_{\star}$. This number density will be taken to be dependent on mass and cosmic epoch, but independent of position in space. The statistical properties of our halo distribution will be ruled then by the underlying density field $\delta$ present in $j_{\nu}$ by means of the bias factor $b(M, \eta)$ (Mo & White, 1996), connecting the halo clustering properties with the power spectrum of $\delta$. Hence, the bias factor $b(M, \eta)$ must be introduced in $S^{CII}(k, \eta)$. Finally, $\tilde{W}_h(k)$ is the Fourier transform of a volume window function giving the physical size of the halo. For simplicity, we shall assume that the halos have a gaussian profile, given in real space by

$$W_h(\mathbf{x}) = \exp\left(-\frac{\mathbf{x}^2}{2\sigma_h^2}\right) \tag{7.39}$$

for a halo placed at $\mathbf{x}_h = 0$, with a typical size of $\sigma_h$. In practice, we shall take $\sigma_h$ equal to the virial radius, $R_v(M, \eta)$. The Fourier transform of this profile reads

$$\tilde{W}_h(\mathbf{k}) = \left(2\pi\sigma_h^2\right)^{3/2} \times \exp\left(-\frac{k^2 \cdot \sigma_h^2}{2}\right) \tag{7.40}$$

and hence, for large scales (small $k$'s), it is essentially the volume of the halo.

Having this present, the 2-point correlation contribution to the angular power spectrum reads

$$C_l^{\text{CII, 2h}} = (4\pi)^2 \int dk \; k^2 P_{\psi}(k) \left[\Delta_l^{\text{CII}}(k, \eta_0)\right]^2 \tag{7.41}$$

where $P_{\psi}(k)$ is the primordial scalar power spectrum. Similarly, the cross-correlation between CII emission and CMB will be given by

$$C_l^{\text{CII - CMB}} = (4\pi)^2 \int dk \; k^2 \; P_{\psi}(k) \left[\Delta_l^{\text{CMB}}(k, \eta_0)\Delta_l^{\text{CII}}(k, \eta_0)\right] \tag{7.42}$$

The result for such computation is shown in Fig.(7.3). This plot concludes our analysis of the line emission in this chapter, showing that the correlation term of the line emission with CMB is smaller in amplitude, or at best comparable, with the amplitude of the scattering signal we have discussed in this thesis even for solar abundance of the emitting species at very high redshift. In this figure we show both the halo-halo correlation term (eqn.7.41) and the enhancement due to correlation with the CMB (eqn.7.42). We also plot the Poisson term in the power spectrum following the procedure given in previous section, and we see that the 2-point halo-halo correlation term

## CII line emission at z=10
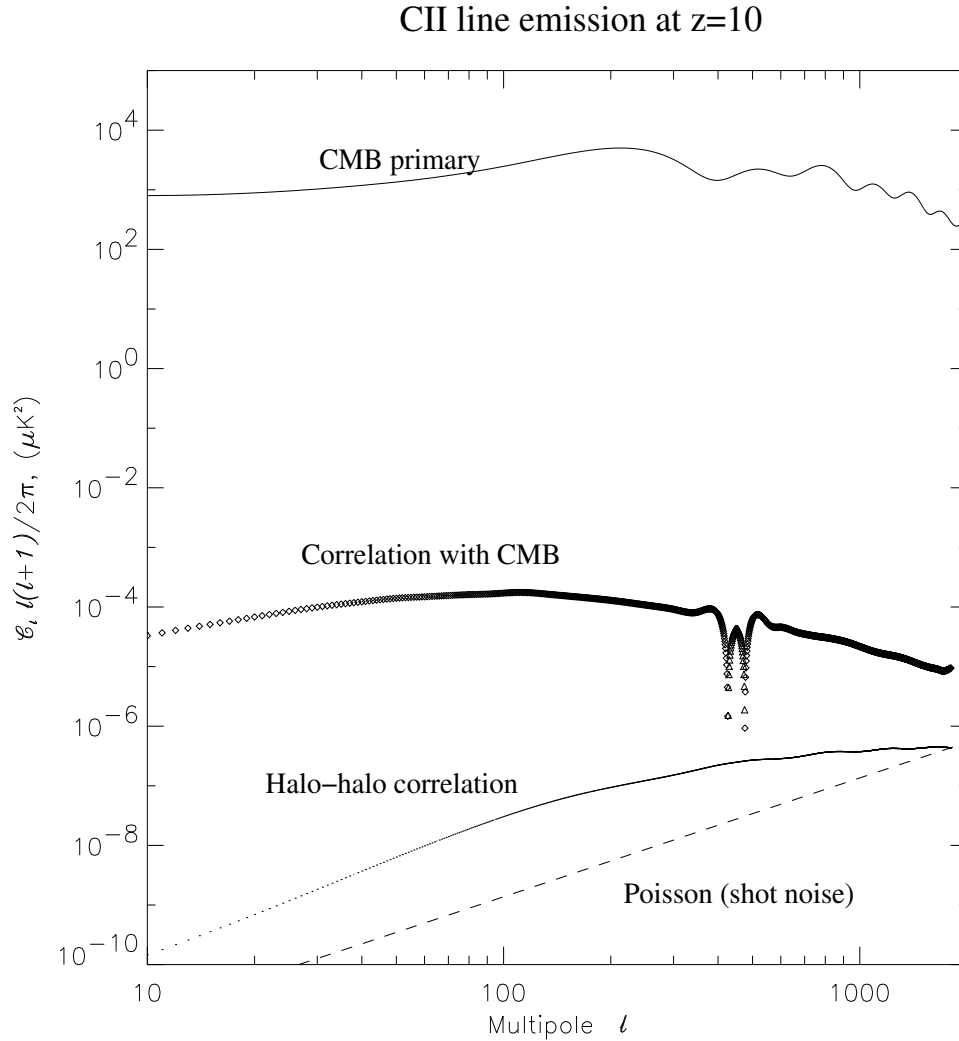


Figure 7.3: Results for line-of-sight computation and enhancement of the emission signal due to correlation with the density field. We show both the halo-halo correlation *(solid line)* and the correlation with the CMB *(diamonds)*, as both can be obtained from the line-of-sight integration as discussed in the text. Also shown is the Poisson component *(dashed line)* as discussed previously. We see the effect of correlation with the CMB which causes strong enhancement of the emission amplitude, especially at large angles. However, this enhancement is small compared to the scattering signal in the same line.

following the line-of-sight integration approach matches with the standard model for computation of 2-point correlation (see Fig.7.2). There is an enhancement in the emission signal due to correlation with CMB, particularly at low $l$-s, but its amplitude is smaller than that of the scattering amplitude that we have discussed. There are two reasons for this: firstly there is no "suppression" term at the high $l$-s (given by $\delta C_l \approx -2\tau_\nu C_l^{\text{prim}}$), which correspond to the uniform smoothing of primordial anisotropies due to resonant scattering and gave a high amplitude for the change in temperature anisotropies from scattering at small angles. The second reason is that because of the velocity dependent nature of the resonant scattering, there was also a velocity related correlation term present which caused enhancement of the signal at low $l$-s. The emission amplitude, on the other hand, is independent of the velocity of the emitter, and therefore the CMB correlation term contains only density correlation of the emitting regions with the CMB. This causes further loss in power at large angles.

The result for line emission at $z = 10$ shows an amplitude of the emission signal correlated with the CMB at $10^{-4}$ $\mu K^2$ for roughly $1°$ scale. In Ch.5 we obtained an amplitude for the scattering signal a few times $10^{-3}$ $\mu K^2$ for the same CII line at the same redshift even for very moderate abundance level (about 1000 times lower than the solar abundance value). Since the SFR-luminosity correlation for the CII line in eqn.(7.13) was obtained from the starburst galaxies in the local universe, the amplitude for the emission signals given in Fig.(7.3) all correspond to solar values for ionic Carbon abundance, and will be much lower if any realistic abundance history is chosen. The Poisson and the halo-halo correlation parts will go down at *square* of the abundance, whereas the signal correlating with the CMB will go down *linearly* with abundance. Therefore the integrated effect of resonant scattering, discussed in this thesis, will dominate over the line emission signal for all angular scales important for CMB studies.

# Chapter 8

# Conclusions

We have investigated in detail the process of resonant scattering of the CMB photons by atoms, ions and molecules; in presence of peculiar motion of the scatterer. This is a very attractive problem because of its simplicity: the resultant change in the brightness temperature of the background CMB photons depends only on two parameters, the optical depth in scattering and the radial component of peculiar velocity. The far-IR fine-structure lines of various atoms and ions, as well as the sub-millimeter rotational lines of diatomic molecules like the CO, provide an effective cross-section for scattering of CMB photons in a wide range of redshifts, which in turn is suitable for various applications like finding peculiar motion of the galaxies, or probing the enrichment and ionization history of the universe.

We presented an exact formulation of the process of resonant scattering in presence of peculiar velocities, which had been absent in the literature. Therefrom we have tried to find applications for the scattering process in individual gas clouds, the main example of which was inferring the motion of nearby galaxies in the CMB rest frame from scattering in CO rotational lines. The process of scattering can cause both an increment or a decrement in the background temperature depending on the direction of motion of the object, but only a *decrement* in temperature can be regarded as the definite signal of scattering, which one can distinguish from emission in the same line. We paid particular attention to Virgo cluster galaxies, where the high amplitude of galactic velocities can give rise to a temperature change of more than 40 $\mu$K km s$^{-1}$in the CO $J = 2 - 1$ 230 GHz line. Future sub-mm instruments like ALMA will be able to resolve galaxies at much further distances ($z \gtrsim 3$), where higher excitation levels of CO as well as the CI fine-structure lines become important. Observing this scattering signal might open a new way to infer cluster peculiar motions and their internal dynamics, as the scattering signal does not depend on the velocity of Hubble expansion and thereby serve as an independent estimator of large scale peculiar motions.

However, observing the signal of scattering from an individual object requires very low density gas, as even at relatively low overdensities the process of collision becomes more effective in producing photons and the object can no longer be visible via scattering. For high velocity galaxies

like M99 in the Virgo cluster this happens at densities $\sim 20$ cm$^{-3}$ in neutral atomic gas for CO 230 GHz line, but for average amplitude of peculiar motions this density limit is lower. In this regard we have described three types of critical densities characterizing the effect of collision. The most important fact is that although individual objects are no longer visible in scattering after the first critical density, when brightness temperature in emission and scattering becomes equal, one can expect to see the integrated signal of scattering from all objects in the sky having densities upto several times higher. This is possible through observing the large-scale coherent distortion in the primordial CMB temperature fluctuations, where the emission from small dense objects are less significant. The frequency dependent nature of the scattering signal, and the possibility to have an enhancement in its amplitude via a non-zero correlation between large-scale density fluctuations at the last scattering surface and at the epoch of scattering, makes the study of CMB power-spectrum distortion an useful tool to study the enrichment and ionization history of the universe.

Under the approximation of negligible drag force, we have computed what are the changes in the CMB angular power spectra introduced by resonant species placed at redshifts which are dependent on the observing and resonant frequencies. The overall effect can be decomposed into a damping or suppression of the original CMB temperature fluctuations, and a generation of new anisotropies. For the optically thin limit to which we have restricted ourselves, damping dominates over generation of new anisotropies in the intermediate and high multipole range ($l \gtrsim 20$).

These changes in the CMB are of very small amplitude ($0.01 - 0.3\mu K$), and could be distinguished from the CMB component by means of their frequency dependence. Indeed, a comparison with respect to a *reference* channel containing only non-frequency dependent temperature fluctuations could be used to quantify the amount of angular power introduced by the resonant species. However, this would only be feasible if either the other frequency-dependent components are negligible or characterized with extreme accuracy. The possible presence of foregrounds, galactic of extragalactic, whose amplitude and spectral behavior is still under characterization, is a serious aspect to be taken into account. Other technical challenges, such as the calibration of different channels and the enormous sensitivity required, should be accessible from the next generation of detector technology.

We have obtained limits for abundances of heavy elements when complete foreground removal is possible, but also have shown values when all foregrounds are present in the sky map. Our analyses have particularly focused on PLANCK HFI channels, whose very low noise levels give extremely strong limits on abundances. It is easiest to observe the proposed effect with HFI at angular scales of $\theta \sim 20°$ or $l \sim 10$ because of the very low noise of the first three HFI channels at these multipoles. Using the 143 & 217 GHz channels of HFI, with the 100 GHz channel as reference, limits as low as $10^{-3} - 10^{-4}$ solar abundance were obtained for atoms and ions of the most important elements like carbon, nitrogen and oxygen in the redshift range [5, 30]. At higher multipoles ($l > 200$), we have shown that future balloon and ground-based experiments like ACT, APEX and SPT can

put similar constraint on abundances, where the predicted signal is stronger because of the higher amplitude of the primordial CMB signal, and effect will be directly proportinal to the optical depths in lines. The presence of foregrounds makes all these limits about a factor of $10^2$ worse, but that must be considered as the most pessimistic scenario.

# Appendix A

# Appendix: Analytic form of $\delta C_l$-s

Following the equation for the $k$-mode of the photon temperature fluctuation,

$$\Delta_T(k,\eta_0,\mu) = \int_0^{\eta_0} d\eta \, e^{ik\mu(\eta-\eta_0)} \left[ \Upsilon(\eta)\left(\Delta_{T0} - i\mu v_b\right) + \dot{\phi} + \psi - ik\mu\psi \right] \tag{A.1}$$

we proceed now to characterize the change in the radiation power spectrum. In eq.(A.1), the terms in the angle $\mu = \hat{\mathbf{k}} \cdot \hat{\mathbf{n}}$ can be eliminated after integrating by parts and neglecting the contribution of boundary terms, (Seljak & Zaldarriaga 1996). This gives:

$$\Delta_T = \int_0^{\eta_0} d\eta \, e^{ik\mu(\eta-\eta_0)} S(k,\eta) \tag{A.2}$$

where the source term $S(k,\eta)$ is defined as

$$S(k,\eta) = e^{-\tau}\left(\dot{\phi} + \dot{\psi}\right) + \Upsilon\left(\Delta_{T0} + \psi + \frac{\dot{v}_b}{k}\right) + \dot{\Upsilon}\left(\frac{v_b}{k}\right) \tag{A.3}$$

From this source term, the angular power spectrum can be expressed as, (e.g. Seljak & Zaldarriaga, 1996):

$$C_l = (4\pi)^2 \int dk \, k^2 P_\psi(k) \left| \int_0^{\eta_0} d\eta S(k,\eta) j_l\left[k(\eta_0 - \eta)\right] \right|^2$$

$$= (4\pi)^2 \int dk \, k^2 P_\psi(k) \left|\Delta_{T,l}\right|^2 \tag{A.4}$$

where $j_l$ is the spherical Bessel function of order $l$ and $P_\psi(k)$ is the initial scalar perturbation power spectrum. If at a given frequency the CMB interacts through the resonant transition $i$ of a species $X$, the measured power spectrum will differ from the reference one by an amount:

$$\delta C_l \equiv C_l^{X_i} - C_l$$

$$= (4\pi)^2 \int dk \, k^2 P_\psi(k) \left[ \left| \int_0^{\eta_0} d\eta \, S^{X_i}(k,\eta) j_l\left[k\left(\eta_0 - \eta\right)\right] \right|^2 \right.$$

$$- \left| \int_0^{\eta_0} d\eta \, S(k, \eta) j_l \left[ k(\eta_0 - \eta) \right] \right|^2 \Big]$$

$$= (4\pi)^2 \int dk \, k^2 P_\psi(k) \Big[ \left| \Delta_{T,l}^{X_i} \right|^2 - |\Delta_{T,l}|^2 \Big]$$

$$= (4\pi)^2 \int dk \, k^2 P_\psi(k) \big[ 2 \, \Delta_{T,l} + \delta\Delta_{T,l} \big] \delta\Delta_{T,l} \tag{A.5}$$

with $\delta\Delta_{T,l} \equiv \int_0^{\eta_0} d\eta \, \left( S^{X_i}(k, \eta) - S(k, \eta) \right) j_l \left[ k(\eta_0 - \eta) \right]$, and where the term $S^{X_i}(k, \eta)$ refers to the sources including the species $X$. Note that the cross term $2 \, \Delta_{T,l} \cdot \delta\Delta_{T,l}$ only arises after computing the difference of the power spectra, i.e., it is not present if one computes the power spectrum of the difference of two maps obtained at different frequencies. This cross term is precisely the responsible of having $\delta C_l$ linear in $\tau_{x_i}$, and hence also linear in the abundance of the species $X_i$. This term also accounts for the correlation existing between the temperature fluctuations generated during recombination and those generated during the scattering with the species $X$. This non-zero correlation is essentially due to those $k$ modes corresponding to lengths bigger than the distance separating the two events, i.e., recombination and scattering with $X$. Let us now model the differential opacity due to this transition as $\dot{\tau}_{X_i} = \tau_{X_i} \mathcal{P}(\eta)$, where $\mathcal{P}(\eta)$ is a profile function of area unity, $\int_0^{\eta_0} d\eta' \, \mathcal{P}(\eta') = 1$. We write the optical depth as $\tau_{tot}(\eta) = \tau(\eta) + \tau_{X_i}(\eta)$, where the last term refers to the optical depth due to the transition $i$ of the $X$ species. It can be expressed as $\tau_{X_i}(\eta) = \tau_{X_i} \, \mathcal{A}(\eta) = \tau_{X_i} \int_\eta^{\eta_0} d\eta' \, \mathcal{P}(\eta')$, with $\mathcal{A}(\eta)$ the area function of the profile $\mathcal{P}(\eta)$. We will assume that the profile peaks at $\eta = \eta_{X_i}$ and that $\eta_-$ and $\eta_+$ are such that $\mathcal{P}(\eta) \approx 0$ for $\eta < \eta_-$ and $\eta > \eta_+$. Hereafter, $\eta_{X_i}$ will be referred to as *transition epoch* or *line epoch*. If we add this new term to the opacity, and assume that $\tau_{X_i} \ll 1$, then we can expand the term $\delta\Delta_{T,l}$ in a power series of $\tau_{X_i}$. In this case, we obtain:

$$\delta\Delta_{T,l} = \tau_{X_i} \cdot \left\{ - \int_0^{\eta_+} d\eta \, j_l \left[ k(\eta_0 - \eta) \right] \mathcal{A}(\eta) \right.$$

$$\times \left[ e^{-\tau} \left( \dot{\phi} + \dot{\psi} \right) + \dot{\tau} e^{-\tau} \left( \Delta_{T0} + \psi + \frac{\dot{v}_b}{k} \right) + \, e^{-\tau} \left( \ddot{\tau} + \dot{\tau}^2 \right) \frac{v_b}{k} \right]$$

$$\left. + \int_0^{\eta_+} d\eta \, j_l \left[ k(\eta_0 - \eta) \right] \mathcal{P}(\eta) e^{-\tau} \left[ \left( \Delta_{T0} + \psi + \frac{\dot{v}_b}{k} \right) + \left( \frac{1}{\mathcal{P}} \frac{d\mathcal{P}}{d\eta} + 2\dot{\tau} \right) \frac{v_b}{k} \right] \right\}$$

$$+ \, \tau_{X_i}^2 \cdot \left\{ \frac{1}{2} \int_0^{\eta_+} d\eta \, j_l \left[ k(\eta_0 - \eta) \right] \mathcal{A}^2(\eta) \right.$$

$$\times \left[ e^{-\tau} \left( \dot{\phi} + \dot{\psi} \right) + \dot{\tau} e^{-\tau} \left( \Delta_{T0} + \psi + \frac{\dot{v}_b}{k} \right) + \, e^{-\tau} \left( \ddot{\tau} + \dot{\tau}^2 \right) \frac{v_b}{k} \right]$$

$$\left. + \int_0^{\eta_+} d\eta \, j_l \left[ k(\eta_0 - \eta) \right] e^{-\tau} \left[ - \left( \Delta_{T0} + \psi + \frac{\dot{v}_b}{k} \right) \mathcal{A}(\eta) \mathcal{P}(\eta) \frac{v_b}{k} \left( \mathcal{P}^2(\eta) + \mathcal{A}(\eta) \left( -\frac{d\mathcal{P}}{d\eta} - 2\dot{\tau} \right) \right) \right] \right\}$$

# A. APPENDIX: ANALYTIC FORM OF $\delta C_L$-S

$$+ \quad \mathcal{O}(\tau_{X_i}^3)$$

$$= \tau_{X_i} \cdot \mathcal{D}_1 + \tau_{X_i}^2 \cdot \mathcal{D}_2 + \mathcal{O}(\tau_{X_i}^3). \tag{A.6}$$

It is worth to note that $\mathcal{D}_1$ contains both the suppression of intrinsic CMB anisotropies, and the generation of new fluctuations at line epoch. This expansion allows us writing $\delta C_l$ as a power series of $\tau_{X_i}$ as well,

$$\delta C_l \;=\; \tau_{X_i} \cdot (4\pi)^2 \int dk \; k^2 P_\psi(k) \left[ \mathcal{D}_1 \; 2\Delta_{T,l} \right]$$

$$+ \; \tau_{X_i}^2 \cdot (4\pi)^2 \int dk \; k^2 P_\psi(k) \left[ \mathcal{D}_2 \; 2\Delta_{T,l} + \mathcal{D}_2^2 \right]$$

$$+ \; \mathcal{O}(\tau_{X_i}^3)$$

$$= \tau_{X_i} \cdot \mathcal{C}_1 + \tau_{X_i}^2 \cdot \mathcal{C}_2 + \mathcal{O}(\tau_{X_i}^3) \tag{A.7}$$

The result of this expansion is displayed in Fig.(A.1): the change in the power spectrum induced by resonant transitions is computed for different redshifts, 25 (top panel) and 500 (bottom panel), and different amplitudes of the optical depth (solid lines correspond to $\tau = 1.5 \times 10^{-4}$ and dot-dashed lines to $\tau = 0.15$). Diamonds give the linear approximation in $\tau$, whereas triangles show the quadratic one. Both match the exact $\delta C_l$'s fairly well for the low $\tau$ cases. Therefore, by means of eq.(5.4), we can establish a linear relation between $\delta C_l$ and the abundance of the species.

In Fig.(A.2), diamonds show the absolute value of $\mathcal{C}_1$ versus $l$. As shown above, this term is the sum of two integrals. The first one is the suppression induced by the $e^{-\tau_{X_i}}$ term, (thick solid line in the figure), whereas the second contain the newly generated anisotropies, (thick dashed line). The latter term has a monopole ($\Delta_0 + \psi$, thin dashed line) and a velocity (thin dotted line) contribution. We are plotting absolute values of all terms. As pointed out by Zaldarriaga & Loeb (2002), the monopole term decreases with cosmic time and hence the velocity term becomes the most important source of generation of new anisotropies. However, this generation takes place at the transition epoch, and hence is shifted towards the low multipole range. It is easy to show that the maximum multipole below which generation becomes significant is roughly given by $l_{X_i} \sim 2\pi \; (\eta_0 - \eta_{X_i})/\eta_{X_i}$. We show that the suppression term is dominant for high multipoles, and only at very low multipoles suppression and generation tend to cancel each other. Only if higher orders in the power expansion are relevant, (i.e., if $\tau_{X_i} \sim 1$) the newly generated anisotropies become important.

This cancellation of suppression and generation terms at low multipoles can be better understood when coming back onto eq.A.1. If in this equation we substitute $\tau$ by $\tau + \tau_{X_i}$, we find that the change in the temperature modes due to $\tau_{X_i}$ can be written as:
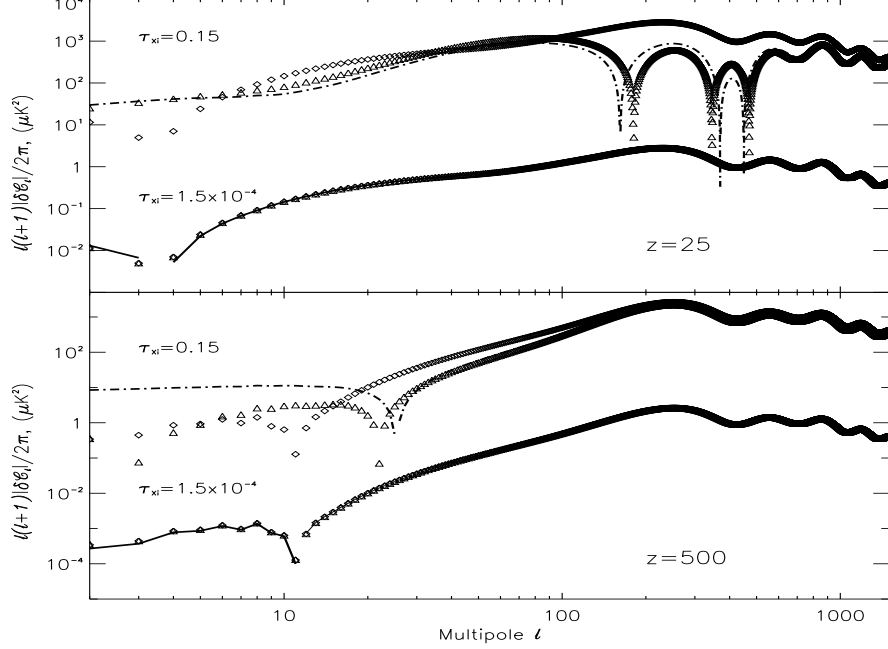
Figure A.1: This figure shows the validity of the linear (diamonds) and quadratic (triangles) approximations on $\tau$ when trying to describe the changes induced in the power spectrum by a resonant transition ($\delta C_l$'s). We see that both suffice to accurately match the theoretical $\delta C_l$'s for redshifts 25 (top panel) and 500 (bottom panel) and for $\tau = 1.5 \times 10^{-4}$, (solid lines). However, when $\tau$ is closer to one (dot-dashed lines), the quadratic approximation performs remarkably better than the linear one.

$$\delta\Delta_T = \left(e^{-\tau_{X_i}} - 1\right) \int_0^{\eta_0} d\eta \, e^{ik\mu(\eta-\eta_0)} \dot\tau e^{-\tau} \left(\Delta_{T0} - i\mu v_b\right)$$

$$+ \, e^{-\tau_{X_i}} \int_0^{\eta_0} d\eta \, e^{ik\mu(\eta-\eta_0)} \dot\tau_{X_i} e^{-\tau} \left(\Delta_{T0} - i\mu v_b\right), \tag{A.8}$$

where we have applied the definition of the visibility function, $\Upsilon(\eta) = \dot\tau(\eta) \, e^{-\tau(\eta)}$. However, recalling that the visibility function gives the probability of a photon being emitted at a given $\eta$, and taking $\dot\tau_{X_i} = \tau_{X_i}\delta_D(\eta - \eta_{X_i})$, the last equation merely implies that

$$\delta\Delta_T \simeq \tau_{X_i} \left[\Delta_{T0}(\eta_{X_i}) - \Delta_{T0}(\eta_{rec}) - i\mu \left(v_b(\eta_{X_i}) - v_b(\eta_{rec})\right)\right], \tag{A.9}$$

where we have taken into account that $\tau_{X_i}$ is much smaller than unity, and approximated the exponentials to unity, as we shall focus on the very low $k$ range. That is, the change in the temperature mode $\Delta_T(k, \mu, \eta)$ reflects the difference of the monopole ($\Delta_{T0}$) and velocity terms when evaluated at recombination and at the transition epochs. We can estimate how this difference
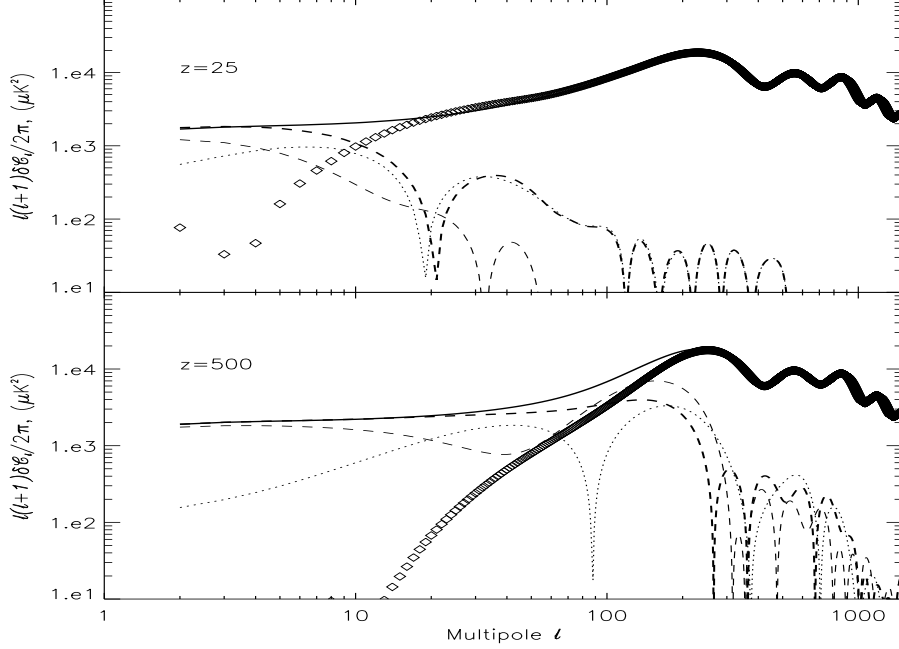
# A. APPENDIX: ANALYTIC FORM OF $\delta C_L$-S



Figure A.2: Study of the different contributions to $\mathcal{C}_1$ in eq.(5.15). Diamonds give $\mathcal{C}_1$ versus multipole. We are plotting only absolute values. In units of $\tau_{X_i}$, we plot the damping term in solid line. The term responsible for the generation of new anisotropies is plotted in thick dashed line. Its two components, monopole $((\Delta_0 + \psi))$ and velocity, are also displayed in thin dashed and thin dotted lines respectively. As conformal time goes by, the relative weight of the velocity term with respect the monopole term increases, and the sum of both at low multipoles approaches the amplitude of the original CMB anisotropies, (solid line). Both generation and damping tend to cancel each other at a multipole $l = l_{X_i}$, dependent on the epoch of interaction $\eta_{X_i}$.

projects onto multipole space if we restrict ourselves to the low multipole (large angle) range. For the scattering redshifts under consideration ($z_{X_i} >$ a few), we can safely neglect the term due to the Integrated Sachs-Wolfe effect. Then from eq.(A.1), one finds that the time dependence of the monopole term $\Delta_{T0}(\eta)$ can be approximated as $\Delta_{T0}(\eta) \simeq \Delta_{T0}(\eta_{rec}) \, j_0 \left( k \left[ \eta - \eta_{rec} \right] \right)$, where $j_0(x)$ is the spherical Bessel function of order zero. From this dependence, it is easy to see that at low multipoles, i.e., at small enough $k$'s, $\Delta_{T0}(\eta_{rec})$ and $\Delta_{T0}(\eta_{\eta_{X_i}})$ will be roughly equal, and thus their difference in the equation above will tend to vanish. This can also be seen in Fig.(A.2), where the contribution of the monopole term to $\mathcal{C}_1$ (thin dashed line) has roughly the same amplitude at redshifts 500 and 25 for $l < 10$. This behaviour is the responsible for the cancellation of the $\delta C_l$'s at low $l$'s. In this situation, the difference of the velocity terms will be of particular relevance. The evolution of velocities can be approximated, after integrating in $\mu$, as $v_b(\eta) \simeq v_b(\eta_{rec}) \dot{D}(\eta)/\dot{D}(\eta_{rec}) j_1 \left( k \left[ \eta - \eta_{rec} \right] \right)$, with $D(\eta)$ the linear growth factor . The growth of velocities

will assure an increase of the Doppler-induced anisotropy power. Finally, due to the fact that $j_l(x)$ is maximum at $x \sim l$, then we have that the Doppler term will predominantly contribute for [1] $k \sim 2\pi/\eta_{X_i}$, which corresponds to multipoles $l_{X_i} \sim 2\pi \left( \eta_0 - \eta_{x_i} \right) / \eta_{X_i}$. Again, this can be checked by looking at the velocity term (dotted line) in Fig.(A.2): the power is projected at lower multipoles at later epochs, scales at which the amplitude grows with conformal time as $\dot{D}$.

Therefore, the factors determining the cross-over of the $\delta C_l$'s from (Doppler-induced) positive values at small $l$ to (absorption-induced) negative values at large $l$ are two: *a)* the constant amplitude of the monopole at large scales, and *b)* the growth of peculiar velocities with cosmic time . The angular scale at which such crossing takes place is roughly determined by the time at scattering epoch, $\eta_{X_i}$, $l_{X_i} \sim 2\pi \left( \eta_0 - \eta_{x_i} \right) / \eta_{X_i}$.

---

[1]We are assuming that $\eta_{X_i} >> \eta_{rec}$ throughout the paper. However, strictly speaking, one should consider the difference of conformal times of recombination and resonant scattering, i.e., $k \sim 2\pi/(\eta_{X_i} - \eta_{rec})$.

# Appendix B

# Appendix: Solution of Statistical Equilibrium Equation

Under the condition of statistical equilibrium, the level populations in a multilevel system are determined by the detailed balance equations

$$
n_i \Big[ A_{i,i-1} + J_{\nu_{i,i-1}} B_{i,i-1} + \mathcal{N}_{H_2} \sum_{j=1}^{i-1} \gamma_{ij} \Big] + n_i \Big[ J_{\nu_{i,i+1}} B_{i,i+1} + \mathcal{N}_{H_2} \sum_{k=i+1}^{N} \gamma_{ij} \Big]
$$
$$
= n_{i+1} \Big[ A_{i+1,i} + J_{\nu_{i+1,i}} B_{i+1,i} \Big] + \mathcal{N}_{H_2} \sum_{k=i+1}^{N} n_k \gamma_{ki} \tag{B.1}
$$
$$
+ n_{i-1} J_{\nu_{i-1,i}} B_{i-1,i} + \mathcal{N}_{H_2} \sum_{j=1}^{i-1} n_j \gamma ij
$$

Here $n_i$ represents population of the $i$-th level, $A_{i,j}$ and $B_{i,j}$ are respectively the Einstein A- and B-coefficients for radiative and induced transitions, and $\gamma_{i,j}$ are the collision rates per unit density (in $cm^{-3}s^{-1}$). $\mathcal{N}_{H_2}$ is the number density of (colliding) $H_2$ molecules, and $J_\nu$ is the background radiation field due to the CMB at frequency $\nu$

$$
J_\nu = \frac{2h\nu^3}{c^2} \Big[ \exp\Big( \frac{h\nu}{kT_{CMB}(z)} \Big) - 1 \Big]^{-1} \tag{B.2}
$$

We can rewrite eqn.(B.1) as the following

$$
n_i \sum_{i \neq j} \Big( C_{ij} + J_{\nu ij} B_{ij} \Big) + n_i \sum_{j<i} Aji - \sum_{j<i} n_j \Big( C_{ji} + J_{\nu_{ji}} B_{ji} \Big)
$$
$$
- \sum_{j>i} n_j \Big( C_{ji} + A_{ji} + J_{\nu_{ji}} B_{ji} \Big) = 0 \tag{B.3}
$$

where we have redefined the collision rate as $C_{ij} = \mathcal{N}_{H_2} \gamma_{ij}$. These are the set of equations we wish to solve.

Clearly, eqn.(B.3) represents a set of $N$ linear equations ($N$ is the maximum number of levels that is being considered), which can be written in matrix format

$$
\begin{pmatrix}
D_{11} & D_{12} & D_{13} & \ldots & D_{1,N-1} & D_{1N} \\
D_{21} & D_{22} & D_{23} & \ldots & D_{2,N-1} & D_{2N} \\
D_{31} & D_{32} & D_{33} & \ldots & D_{3,N-1} & D_{3N} \\
\vdots & \vdots & \vdots & \vdots & \vdots & \vdots \\
\vdots & \vdots & \vdots & \vdots & \vdots & \vdots \\
D_{N-1,1} & D_{N-1,2} & D_{N-1,3} & \ldots & D_{N-1,,N-1} & D_{N-1,N} \\
D_{N1} & D_{N2} & D_{N3} & \ldots & D_{N,N-1} & D_{NN}
\end{pmatrix}
\begin{pmatrix}
n_1 \\ n_2 \\ n_3 \\ \vdots \\ \vdots \\ n_{N-1} \\ n_N
\end{pmatrix}
=
\begin{pmatrix}
0 \\ 0 \\ 0 \\ \vdots \\ \vdots \\ 0 \\ 0
\end{pmatrix}
\tag{B.4}
$$

However, these set of $N$ equations form an exactly singular system, as can be seen by summing these equations (it gives $0 = 0$). We need to replace one of the equations (any one can be replaced, but we choose the last one) by the conservation equation

$$
n_1 + n_2 + n_3 + \ldots n_N = 1
\tag{B.5}
$$

Hence our matrix equation to be solved becomes

$$
\begin{pmatrix}
D_{11} & D_{12} & D_{13} & \ldots & D_{1,N-1} & D_{1N} \\
D_{21} & D_{22} & D_{23} & \ldots & D_{2,N-1} & D_{2N} \\
D_{31} & D_{32} & D_{33} & \ldots & D_{3,N-1} & D_{3N} \\
\vdots & \vdots & \vdots & \vdots & \vdots & \vdots \\
\vdots & \vdots & \vdots & \vdots & \vdots & \vdots \\
D_{N-1,1} & D_{N-1,2} & D_{N-1,3} & \ldots & D_{N-1,,N-1} & D_{N-1,N} \\
1 & 1 & 1 & \ldots & 1 & 1
\end{pmatrix}
\begin{pmatrix}
n_1 \\ n_2 \\ n_3 \\ \vdots \\ \vdots \\ n_{N-1} \\ n_N
\end{pmatrix}
=
\begin{pmatrix}
0 \\ 0 \\ 0 \\ \vdots \\ \vdots \\ 0 \\ 1
\end{pmatrix}
\tag{B.6}
$$

This we solve by the standard Gauss-Jordan elimination method, which replaces the matrix of equation coefficients by the unity matrix, so that we have

$$
\begin{pmatrix}
1 & 0 & 0 & \ldots & 0 & 0 \\
0 & 1 & 0 & \ldots & 0 & 0 \\
0 & 0 & 1 & \ldots & 0 & 0 \\
\vdots & \vdots & \vdots & \vdots & \vdots & \vdots \\
\vdots & \vdots & \vdots & \vdots & \vdots & \vdots \\
0 & 0 & 0 & \ldots & 1 & 0 \\
0 & 0 & 0 & \ldots & 0 & 1
\end{pmatrix}
\begin{pmatrix}
n_1 \\ n_2 \\ n_3 \\ \vdots \\ \vdots \\ n_{N-1} \\ n_N
\end{pmatrix}
=
\begin{pmatrix}
p_1 \\ p_2 \\ p_3 \\ \vdots \\ \vdots \\ p_{N-1} \\ p_N
\end{pmatrix}
\tag{B.7}
$$

$p_1$, $p_2$, $\ldots$ $p_N$ are the required set of solution for level populations.

## B. APPENDIX: SOLUTION OF STATISTICAL EQUILIBRIUM EQUATION

### Method of computation

We begin by the collision rates $\gamma_{ij}$, and compute the full $\gamma$-matrix using the relation

$$\gamma_{ji} \;=\; \gamma_{ij} \; \frac{g_i}{g_j} \; \exp\Big(-\frac{h\nu_{ij}}{kT_{gas}}\Big)$$

Then we compute the collision rate matrix $\mathbb{C}$ by multiplying this with the Hydrogen molecule number-density, which in turn is obtained from the mean baryonic density and the overdensity of the cloud.

The Einstein A- and B-coefficients are related by

$$\begin{aligned}
B_{ij} &= \frac{c^2}{2h\nu_{ij}^3} \; A_{ij} \quad \text{if } i > j \\
&= \frac{g_j}{g_i} \; B_{ji} \qquad \text{if } i < j
\end{aligned}$$

We assume the radiative transition probabilities are of significance only between *adjacent* levels. Now using eqn.(B.2), we compute the matrix $(\mathbb{B}\mathbb{J}_\nu)$ by the relation

$$\begin{aligned}
B_{ij}J_{\nu_{ij}} &= A_{ij}\left[\exp\Big(\frac{h\nu_{ij}}{kT_{CMB}(z)}\Big) - 1\right]^{-1} \quad \text{if } i > j \\
&= (g_j/g_i) \; B_{ji}J_{\nu_{ij}} \qquad\qquad\qquad \text{if } i < j
\end{aligned}$$

To compute the matrix of equation coefficients $\mathbb{D}$, we first put all diagonal elements equal to zero, and calculate the off-diagonal elements by the relation (these coefficients are negative since they represent loss of molecules from a given level)

$$\begin{aligned}
D_{ij} &= -\Big(C_{ji} + A_{ji} + B_{ji}J_{\nu_{ji}}\Big) \qquad \text{if } i < j \\
&= -\Big(C_{ij} + B_{ij}J_{\nu_{ij}}\Big) \qquad\qquad \text{if } i > j
\end{aligned}$$

Finally the diagonal elements of matrix $\mathbb{D}$ are computed by summing all the elements in a given column, since they represent net gain of molecules into any given level (and hence are positive)

$$D_{ii} = -\Big( \sum_{i>j} D_{ji} + \sum_{i<j} D_{ij} \Big)$$

Thus we have the matrix equation $\mathbb{D}\mathbf{n} = 0$ to solve. The last row is replaced by the *conservation* or *closure* relation to prevent singular solution, and Gauss-Jordan method is applied to obtain the level populations $\mathbf{p}$.
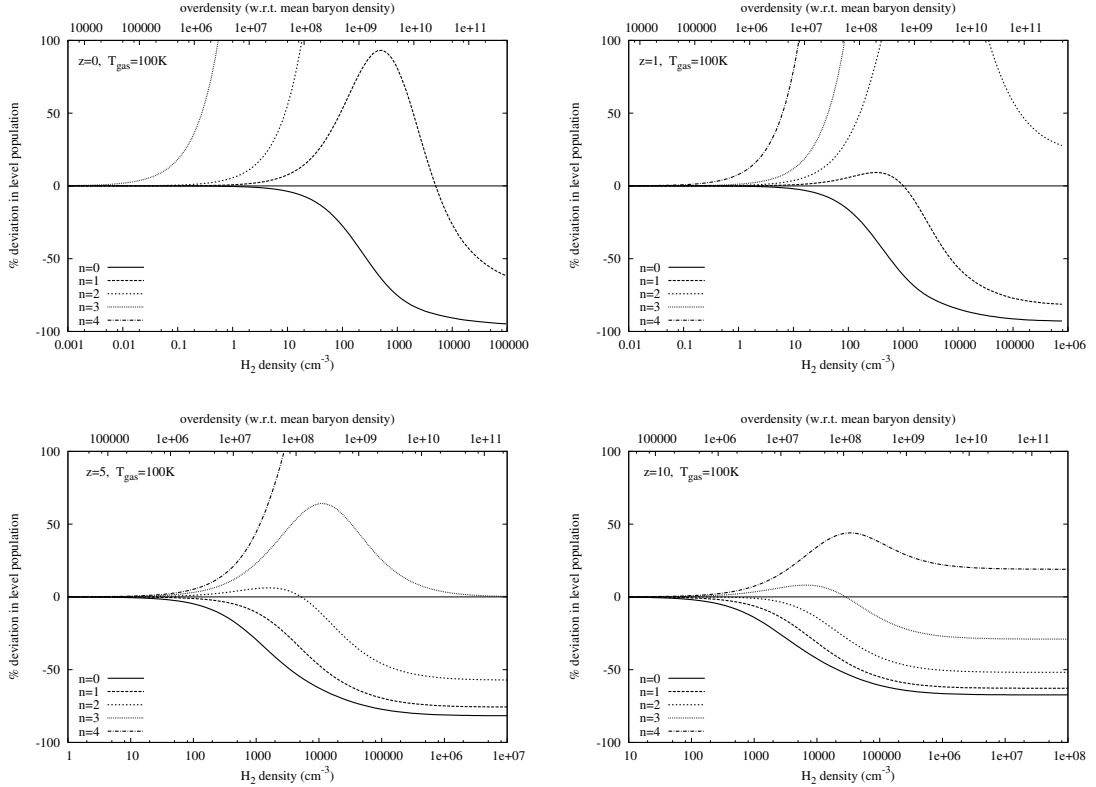
Figure B.1: Change in level population of different rotational levels of the CO molecule at different redshifts, as fuction of density of $H_2$ molecules. In the horizontal axis we plotted the molecular density, and in the vertical axis the *percentage change* in the level population, both increase and decrease, compared with the population dictated only by CMB. Therefore a change by 100% corresponds to doubling of a level populations. Results are shown for redshifts $z = 0, 1, 5$ & $10$, respectively.

## Application: level populations of the CO molecule

Our example for applying the above formalism in a physical system is the excitation of the rotational levels of CO molecules in collision with $H_2$. We solved for the level populations upto $N = 15$, in a 100 K neutral gas, for different redshifts. The Einstein coefficients were taken from Chandra et al. (1996), and the collisional rates are from Flower & Launay (1985). The only radiation field affecting the level populations were assumed to be that of the CMB.

In Fig.(B.1) we have shown how the fraction of CO molecules in the first five rotational levels changes with increasing molecular density. The four panels correspond to redshifts $z = 0, 1, 5$ & $10$, respectively. The population of the lowest ($J = 0$) level can only decrease as the density increases, as the collisions will tend to populate the upper levels more and more, thereby reducing the population at the lowest level. The upper levels initially increase their population as a result of depopulation of lower levels, before decreasing again as for higher densities even higher levels get

populated. The very rapid increase for levels $J \geq 3$ levels at low redshifts reflect the fact that these levels had been almost not populated when only CMB was present, therefore any slight increase in their population coming from collisions results in a rapid increase in the percentage deviation.
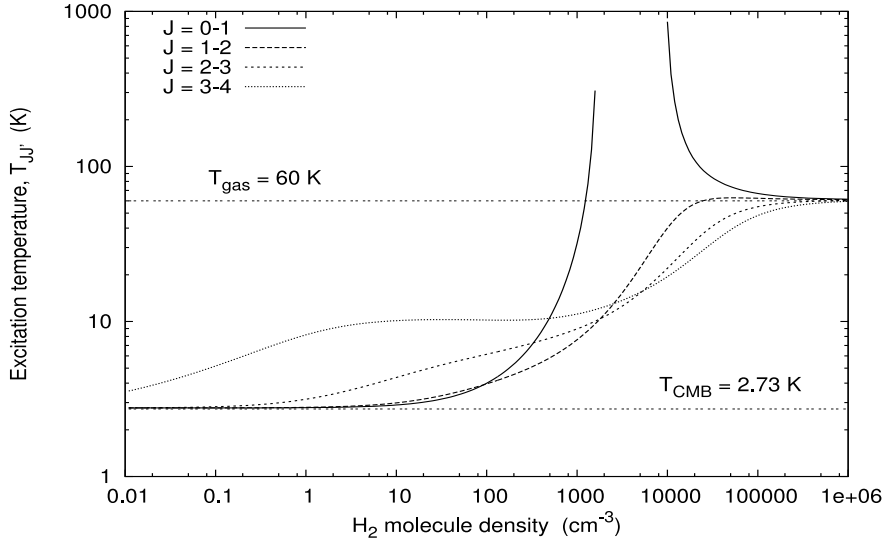


Figure B.2: Excitation temperature for various CO rotational levels, as function of $H_2$ molecular density. For low densities we have $T_{EX}$ equal to the background CMB temperature for all levels. Then with increasing density the collision starts to influence level populations and makes $T_{EX}$ to increase. At very high densities collisional processes completely dominates populating and de-populating levels, and the excitation temperature becomes equal to the kinetic temperature of the gas (LTE condition). The discontinuity in the $T_{EX}$ for $J = 0$ level corresponds to a range of densities where the excitation temperature becomes *negative* and population inversion occurs for this transition.

Fig.(B.2) shows how the excitation temperature of the first four rotational transitions change with increasing density. For very low density the excitation temperature is equal to the $T_{CMB}$, reflecting the fact that collisions does not exert any influence in populating or de-populating the levels. With increasing density the excitation temperature increases gradually, and finally it asymptotically approaches the kinetic temperature of the gas. This is the domain of classical critical density, when collisional de-excitation rate from the upper levels become faster than the radiative de-excitation rates. The interesting discontinuity in the curve corresponding to $J = 0 - 1$ 115.35 GHz transition marks the region when $T_{EX}$ becomes negative! This corresponds to a *population inversion*, which can lead to maser action in this lowest CO rotational line. We found that such an effect has actually been discussed by some authors, first described by Morris (1980) and later analyzed in details by Piehler et al. (1991).

# Bibliography

[1] Basu, K., Hernández-Monteagudo, C. & Sunyaev, R. 2004, A&A, 416, 447

[2] Bennett, C., Halpern, M., Hinshaw, G. et al. 2003, ApJS, 148, 1

[3] Bennett, C., Hill, R., Hinshaw, G. et al. 2003b, ApJS, 148, 97

[4] Bergstrom, L. & Goobar, A. 1998, *Cosmology and Particle Astrophysics*, Wiley

[5] Blain, A. 1999, MNRAS, 309, 955

[6] Blain, A., Smail, I., Ivison, R. et al. 1999, MNRAS, 302, 632

[7] Bond, J., Efstathiou, G. & Tegmark, M. 1997, MNRAS 291, L33

[8] Boselli, A., Gavazzi, G., Lequeux, J. et al. 2002, A&A, 385, 454

[9] Bougleux, E. & Galli,D. 1997, MNRAS, 288, 638

[10] Bromm, V. & Loeb, A. 2002, ApJ, 575, 111

[11] Buat, V. & Xu, C. 1996, A&A, 306, 61

[12] Butler, B. & Wootten, A. 1999, *ALMA Memo No. 276*, NRAO

[13] Cen, R. 2003, ApJ, 591, 12

[14] Cen, R. & Ostriker, J.P. 1999, ApJ, 514, 1

[15] Chandra, S., Maheswari, V. & Sharma, A. 1996, A & AS, 117, 557

[16] Church, S. 2002, technical report, scripts for talk available from: http://ophelia.princeton.edu/~page/cmbpol-technology-v2.ppt

[17] Chiang, E. & Goldreich, P. 1997, ApJ, 490, 368

[18] Ciardi, B., Stoehr, F. & White, S. 2003, MNRAS, 343, 1101

[19] Colbert, J., Malkan, M., Clegg, P. et al. 1999, ApJ, 511, 721

## BIBLIOGRAPHY

[20] Cole, S. & Kaiser, N. 1988, MNRAS, 233, 637

[21] Cooray, A. 2001, Ph.Rev.D, 64, 3514

[22] Crenny, Y. & Federman, S. 2004, ApJ, 605, 278

[23] da Silva, A., Barbosa, D., Liddle, A. et al. 2000, MNRAS, 317, 37

[24] Davis, M. & Peebles, P.J.E. 1983, Ann.Rev.A&A, 21, 109

[25] de Bernardis, P., Dubrovich, V., Encrenaz, P. et al. 1993, A&A, 269, 1

[26] Dietrich, M., Hamann, F., Appenzeller, I. & Vestergaard, M. 2003, ApJ, 596, 817

[27] Dubrovich, V. 1977, SvA Lett., 128, 315

[28] Dubrovich, V. 1993, Ast. Lett., 19, 53

[29] Dubrovich, V. 1997, A&A, 324, 27

[30] Einsestein, D., Hu, W. & Tegmark M. 1999 ApJ, 518, 2

[31] Federspiel, M., Tammann, G. & Sandage, A. 1998, ApJ, 495, 115

[32] Fixsen D. et al. 1996, ApJ, 430, L85

[33] Flower, D. & Launay, J. 1985, MNRAS, 214, 271

[34] Freedman, W., Madore, B., Mould, J. et al. 1994, Nature, 371, 757

[35] Freudling, W., Corbin, M. & Korista, K. 2003, ApJ, L67

[36] Fukugita, M., Hogan, C. & Peebles, P.J.E. 1998, 503, 518

[37] Furlanetto, S., Zaldarriaga, M. & Hernquist, L. 2004, ApJ, 613, 1

[38] Genzel, R. 1991, *The Galactic Intersteller Medium, Saas-Fee Advanced course 21* (eds. D. Pfenninger & P. Bartholdi), Springer-Verlag

[39] Giovanelli, R., Haynes, M. et al. 1998, AJ, 116, 2632

[40] Gnedin, N. & Jaffe, A. 2001, ApJ, 551, 3

[41] Gradshteyn, I. & Ryzhik I. 1965, *Table of Integrals, Series and Products*, Academy Press, New York

[42] Gramann, M. & Suhhonenko, I. 2003, 339, 271

[43] Green, S. & Thaddeus, P. 1976, ApJ, 205, 766

[44] Grimm, H.-J., Gilfanov, M. & Sunyaev, R. 2003, MNRAS, 339, 793

[45] Gruzinov, A. & Hu, W. 1998, ApJ, 508, 435

[46] Gunn, J. & Peterson, B. 1965, ApJ, 142, 1633

[47] Heger, A. & Woosley, S. 2002, ApJ, 567, 532

[48] Hernández-Monteagudo, C. & Sunyaev, R. 2004a, *astro-ph/0405487*

[49] Hernández-Monteagudo, C. & Sunyaev, R. 2004b, *in preparation*

[50] Hernquist, L. & Springel, L. 2003, MNRAS, 341, 1253

[51] Hoffman, G., Lewis, B. & Salpeter, E. 1995, 441, 28

[52] Hu, W. & Sugiyama, N. 1994, Phys. Rev. D, 50, 627

[53] Hinshaw, G., Barnes, C., Bennett, C.L. et al. 2003, ApJS, 148, 63

[54] Hunter, D., Kaufman, M., Hollenbach, D. et al. 2001, ApJ, 553, 121

[55] Jerjen, G. & Tammann, G. 1993, A&A, 276, 1

[56] John, T. 1988, A&A, 193, 189

[57] Kaufman, M., Wollfire, M., Hollenbach, D. et al. 1999, ApJ, 527, 795

[58] Kennicutt, R. 1998, ApJ, 498, 541

[59] Komatsu, E. & Kitayama, T. 1999, ApJ, 526, 1

[60] Knox, L. 1995, Ph.Rev.D, 52, 4307

[61] Kogut, A., Lineweaver, C., Smoot, G. et al. 1993, ApJ, 419, 1

[62] Kogut A., Spergel, D.N., Barnes, C. et al., 2003, ApJS, 148, 161

[63] Loeb, A. 2001, ApJL, 555, 1

[64] Loeb, A. & Zaldarriaga, M. 2002, ApJ, 564, 52

[65] Lu, N., Salpeter, E., Hoffman, G. 1994, ApJ, 426, 473

[66] Lutz D., Compilation of FS Line Parameters for ISO Spectroscopy, 1998.
http://www.mpe.mpg.de/www_ir/ISO/linelists/index.html

[67] Madau, P., Meiksin, A. & Rees, M. 1997, ApJ, 475, 429

# BIBLIOGRAPHY

[68] Malhotra, S., Kaufman, M., Hollenbach, D. et al. 2001, ApJ, 561, 766

[69] Maoli, R., Melchiorri, F. & Tosti, D. 1994, ApJ, 425, 372

[70] Maoli, R., Ferrucci, V., Melchirri, F. et al. 1996, ApJ, 457, 1

[71] Mather, J., Cheng, E., Cottingham, D. et al. 1994, ApJ, 420, 439

[72] Mathis, J. 1990, Ann.Rev.A&A, 28, 37

[73] Mihalas, D. 1970, *Steller Atmospheres*, W. H. Freeman & Co.

[74] Misiriotis, A., Papadakis, I., Kylafis, N. et al. 2004, A&A, 417, 39

[75] Mo, H.-J. & White, S. 1996, MNRAS, 282, 347

[76] Morris, M. 1980, ApJ, 236, 823

[77] Oh, S., Cooray, A. & Kamionkowski, M. 2003, MNRAS, 342, 20

[78] Osterbrock, D. 1988, *Astrophysics of Gaseous Nebulae and Active Galactic Nuclei*, University Science Books

[79] Ostriker, J.P. & Vishiac, E. 1986, ApJ, 306, L51

[80] Padmanabhan, T. 2002, *Theoretical Astrophysics Vol. III: Galaxies and Cosmology*, Cambridge University Press

[81] Page, L., Barnes, C., Hinshaw, G. et al. 2003, ApJS, 148, 39

[82] Peebles, P.J.E. & Yu, J. 1970, ApJ, 162, 815

[83] Penton, S., Shull, J. & Stocke, J. 2000, ApJ, 544, 150

[84] Poglitsch, A., Krabbe, A., Madden, S. et al. 1995, ApJ, 454, 293

[85] Pierce, M. & Tully, R. 1988, ApJ, 330, 579

[86] Pradhan A.K. & Peng J., 1995, Atomic Data For The Analysis of Emission Lines (STScI Symposium Series no. 8, Ed: R.E.Williams and M.Livio, CUP)

[87] Piehler, G., Kegel, W. & Tsuji, T. 1991, A&A, 245, 580

[88] Press, W. & Schechter, P. 1974, ApJ, 187, 425

[89] Prunet, S., Sethi, S.K. & Bouchet, F.R. 2000, MNRAS, 314, 348

[90] Razoumov, A., Norman, M., Abel, T. & Scott, D. 2002, ApJ, 572, 695

[91] Röllig, M. 2002, A&A, 392, 1081

[92] Rybicki, G. & Lightman, A. 1985, *Radiative Processes in Astrophysics*, Wiley

[93] Sachs, R. & Wolfe, A. 1967, ApJ, 147, 73

[94] Sasaki, S. 194, PASJ, 46, 427

[95] Salpeter, E. 1955, ApJ, 121, 161

[96] Sandage, A., Tammann, G. & Hardy, E. 1972, ApJ, 172, 253

[97] Sazonov, S., Churazov, E., & Sunyaev, R. 2002, MNRAS, 333, 191

[98] Seljak, U., Burwell, J. & Pen, U.L. 2000, Phys. Rev. D., 63, 3001

[99] Seljak, U. & Zaldarriaga, M. 1996, ApJ, 469, 437

[100] Silk, J. 1974, ApJ, 193, 525

[101] Smoot, G. & Scott, D. 1996, astro-ph/9603157

[102] Sobolev, V.V. 1946, *Moving Atmospheres of Stars*, Leningrad State Univ.; English transl.1960, Harvard Univ. Press

[103] Sokasian, A., Yoshida, N., Abel, T. et al. 2004, MNRAS, 350, 47

[104] Suginohara, M., Suginohara, T., & Spergel, D.N. 1999, ApJ, 512, 547

[105] Spergel, D., Verde, L., Peiris, H. et al 2003, ApJS, 148, 175

[106] Springel, V., White, M. & Hernquist, L. 2001, ApJ, 549, 681

[107] Springel, V. & Hernquist, L. 2003, MNRAS, 339, 312

[108] Stacey, G., Geis, N., Genzel, R. et al. 1991, ApJ, 373, 423

[109] Sunyaev, R. & Zel'dovich, Ya.B. 1970, Ap&SS, 7, 3

[110] Sunyaev, R. & Zel'dovich, Ya. B. 1972, Comm. Astrophys. Sp. Phys., 4, 173

[111] Sunyaev, R. & Zel'dovich, Ya. B. 1975, MNRAS, 171, 375

[112] Sunyaev, R. 1977, SvAL, 3, 268

[113] Sunyaev, R. & Zel'dovich, Ya. B. 1980, MNRAS, 190, 413

[114] Tammann, G. & Sandage A. 1985, ApJ, 294, 81

## BIBLIOGRAPHY

[115] Tegmark, M., Eisenstein, D.J., Hu, W. & de Oliveira-Costa A. 2000, ApJ, 530133

[116] Valageas, P., Silk, J. & Schaeffer, R. 2001, A&A, 366, 363

[117] Varshalovich, D. Khersonskii, V. & Sunyaev, R. 1981, Astrophysics 17, 273

[118] Vishniac, E., 1987, ApJ, 322, 597

[119] Wyithe, J. & Loeb, A. 2003, ApJ, 588, L69

[120] Xu, C., Lisenfeld, U., Völk, H. et al. A&A, 282, 19

[121] Yoshida, N., Stoehr, F., Springel, V. & White, S. 2002, MNRAS, 335, 762

[122] Yu, K., Billawala, Y. & Bally, J. 1999, AJ, 118, 2940

[123] Yu, Q., Spergel, D. & Ostriker, J.P. 2001, ApJ, 558, 23 (YSO)

[124] Zaldarriaga, M. & Loeb, A. 2002, ApJ, 564, 52

[125] Zel'dovich, Ya. B., Kurt, V. & Sunyaev, R. 1968, ZhETF, 55, 278

[126] Zel'dovich, Ya. B. & Sunyaev, R. 1969, Ap&SS, 4, 301

[127] Zel'dovich, Ya. B. & Sunyaev, R. 1980, SvAL, 6, 285